ELECTRON ENHANCED ATOMIC LAYER DEPOSITION (EE-ALD) FOR ROOM TEMPERATURE GROWTH OF GALLIUM NITRIDE, SILICON, AND BORON NITRIDE FILMS

by

JACLYN KELLY SPRENGER

B.S., Washington State University, 2012

A thesis submitted to the

Faculty of the Graduate School of the

University of Colorado in partial fulfillment

of the requirement for the degree of

Doctor of Philosophy

Department of Chemistry

2017

This thesis entitled:

ELECTRON ENHANCED ATOMIC LAYER DEPOSITION (EE-ALD) FOR ROOM TEMPERATURE GROWTH OF GALLIUM NITRIDE, SILICON, AND BORON NITRIDE FILMS

by Jaclyn Kelly Sprenger

has been approved for the Department of Chemistry and Biochemistry

_____

Steven M. George

_____

Michael P. Marshak

Date_____

The final copy of this thesis has been examined by the signatories, and we find that both the content and the form meet acceptable presentation standards of scholarly work in the above mentioned discipline.

Sprenger, Jaclyn Kelly (Ph.D., Chemistry [Physical])

ELECTRON ENHANCED ATOMIC LAYER DEPOSITION (EE-ALD) FOR ROOM TEMPERATURE GROWTH OF GALLIUM NITRIDE, SILICON, AND BORON NITRIDE FILMS

Thesis directed by Professor Steven M. George

Abstract

Electron enhanced atomic layer deposition (EE-ALD) can drastically reduce the temperatures required for film growth through electron stimulated desorption (ESD) of surface species. The desorption process creates highly reactive “dangling bond” surface sites. Precursors can then adsorb efficiently on the dangling bonds. EE-ALD enables deposition of thin films on thermally sensitive substrates and growth of laminate materials where alloying would occur at traditional processing temperatures.

We have demonstrated the EE-ALD of polycrystalline GaN, BN, and amorphous Si at room temperature (27˚C). Film growth was performed using alternating exposures of the appropriate precursors and low energy electrons (~100 eV). X-ray reflectivity and spectroscopic ellipsometry measurements monitored linear film growth versus number of reaction cycles. Additionally, we observed some dependence of the growth rate on electron flux and electron energy. Growth rates varied from 0.2 Å/cycle for Si films to 3.2 Å/cycle for BN films.

Depth-profiling using x-ray photoelectron spectroscopy demonstrated clean BN (1.3:1) films with < 3 at.% C and O impurities. Crystallites as large as 10 nm were observed by high-resolution transmission electron microscopy and grazing angle x-ray diffraction for GaN films. EE-ALD should facilitate the deposition of a variety of ALD films at low temperature. Materials grown with hydride or halide precursors are all possible candidates due to their large ESD cross-sections.

Acknowledgements

I would like to take a moment to recognize those who have guided me and helped me throughout my pursuit of a PhD.

First, I would like to thank Prof. Steven M. George for all the support, direction and motivation he has provided throughout the years especially in the face of unexpected results and equipment problems.

Second, I would like to thank the Steven George Research Group members especially those who have helped me including Dr. Andrew Cavanagh, Dr. Huaxing Sun, Dr. Virginia Anderson, Dr. Diane Lancaster, Dr. Daniel Higgs, Mr. Jonas Gertsch and Ms. Jasmine Wallas.

Third, I would like to thank my family and friends for their support. Particularly, I would like to acknowledge my parents, Randy and Katy Sprenger, for their willingness to look over my writing. Additionally, I would like to acknowledge my partner, Greg Benolken, and my grandmother, Kappy Sprenger, without whose encouragement I would not have been as successful.

Fourth, I would like to thank Dr. Don David and Mr. Ken Smith from the CIRES Integrated Instrument Development Facility for their assistance in reactor design and building, LabVIEW programming, and instrument troubleshooting.

Fifth, I would like to thank all my collaborators including Dr. Kathryn Wahl from Naval Research Laboratories, Dr. Alexana Roshko and Dr. Paul Blanchard from the National Institute of Standards and Technologies, and Dr. Russell Perkins and Mr. Andrew Tomaschke from the University of Colorado Boulder.

Lastly, I am very grateful to the Defense Advanced Research Projects Agency (DARPA) for funding this work.

Contents

Abstract iii
Acknowledgements iv
Contents v
Figures vii
Chapter 1: Introduction 1
I. Atomic Layer Deposition 1
A. Basics 1
B. Applications 3
C. Limitations 5
II. Non-Thermal Atomic Layer Deposition 6
A. Mechanisms for Enhancement 6
III. Electron Enhanced Atomic Layer Deposition 7
A. Electron Stimulated Desorption 7
B. Ultra-high Vacuum Reactor Design 9
C. Compatible Precursors 11
Chapter 2: Electron Enhanced Growth of Crystalline Gallium Nitride Thin Films at Room Temperature and 100°C Using Sequential Surface Reactions[39] 13
I. Abstract 13
II. Introduction 14
III. Experimental 18
A. Vacuum Chamber 18
B. Chemicals and Materials 21
C. *Ex situ* Film Analysis 22
IV. Results and Discussion 23
A. Film Growth and Characterization Using Spectroscopic Ellipsometry 23
B. Crystallinity from GIXRD Measurements 30
C. Crystallinity from TEM Measurements 34
D. Composition from XPS Depth-Profiling Measurements 34
E. Mass Spectrometry Measurements of H_2 Desorption and Etch Products 40
F. Constant Ion Currents during Electron Exposures 44
G. Electron Enhancement for Other Thin Films and Competing Growth and Etching 48
V. Conclusions 50
VI. Acknowledgements 51
Chapter 3: Electron Enhanced Atomic Layer Deposition of Silicon Thin Films at Room Temperature[112] 52
I. Abstract 52
II. Introduction 53
III. Experimental 56
A. Vacuum Chamber 56
B. Chemicals and Materials 58
C. *In situ* Film Analysis 60
D. *Ex situ* Film Analysis 60
IV. Results and Discussion 61
A. Film Growth and Characterization Using *in situ* Multi-Wavelength Ellipsometry 61

B. Self-Limiting Growth Characterization 66
C. Hydrogen ESD Cross Section 70
D. Composition from *in situ* AES and *ex situ* XPS Depth-Profiling Measurements 73
E. Spatial Profile of Deposition Area and XRD Measurements 75
F. Applications of Si EE-ALD 80
V. Conclusions 81
VI. Acknowledgements 82
Chapter 4: Electron Enhanced Atomic Layer Deposition of Boron Nitride Thin Films at Room Temperature[163] 83
I. Abstract 83
II. Introduction 84
III. Experimental 87
A. Vacuum Chamber 87
B. Chemicals and Materials 87
C. *In situ* Growth Analysis 88
D. *Ex situ* Film Analysis 89
IV. Results and Discussion 90
A. *In situ* Film Growth and Characterization 90
B. Growth Conformality 98
C. Film Composition 100
D. Film Crystallinity and Structure 103
E. Proposed Growth Mechanism 106
F. Growth on Patterned Substrates 108
V. Conclusions 111
VI. Acknowledgements 112
Chapter 5: Experimental Details 113
I. Reaction Conditions 113
II. Cleaning Substrate Surfaces 115
III. Electron Source Instability 116
IV. Carbon Contamination 117
A. Reaction Chamber 117
B. Hydrogen Atom Beam Source 120
C. Wire Insulation 121
D. Auger Spectrometer 122
Chapter 6: Future Directions 123
I. Bottom-Up Filling 123
II. Deposit-Etch Technique 124
References 127

Figures

Figure 1.1: Cartoon for an ALD process using sequential dosing of precursors A and B. ALD relies on self-limiting surface modifications for monolayer growth control.[2] 2
Figure 1.2: Cross-sectional SEM image of an Al_2O_3 ALD film growth on a patterned trench structure demonstrates the high levels of obtainable conformality with ALD.[3] 4
Figure 1.3: Menzel-Gomer-Redhead mechanism for electron stimulated desorption.[1] 8
Figure 1.4: Knotek-Feibelman mechanism for electron stimulated desorption.[1] 10
Figure 1.5: Schematic of reactor designed for this EE-ALD work. 12
Figure 2.1: Proposed growth mechanism for electron-enhanced GaN growth using sequential surface reactions. 17
Figure 2.2: Experimental schematic of vacuum apparatus. 19
Figure 2.3: Photo of GaN film grown on Si(111) substrate at 27 °C. 25
Figure 2.4: (a) GaN film on Si(111) wafer showing three positions for analysis using spectroscopic ellipsometry. (b) Thickness of GaN versus number of reaction cycles at the three positions. 27
Figure 2.5: Index of refraction, n, and extinction coefficient, k, versus radiation energy for the GaN film on Si(111) wafer. 29
Figure 2.6: GIXRD of GaN films grown on Si(111) wafers at (a) 27 °C and (b) 100 °C. (c) Positions and intensities of diffraction peaks for crystalline wurtzite GaN powder. 31
Figure 2.7: Photo of GaN film grown at 27 °C on a single-crystal GaN(0001) substrate attached to a Si(111) wafer using a carbon adhesive. 33
Figure 2.8: Cross-sectional HRTEM phase contrast images of GaN films grown on Si(111) wafer at (a) 27 °C and (b) 100 °C. 35
Figure 2.9: Cross-sectional HRTEM phase contrast image of the GaN film grown on Si(111) wafer at 100 °C. 36
Figure 2.10: XPS depth profile of GaN film grown on Si(111) wafer showing oxygen-free stoichiometric GaN with some carbon contamination. An Al capping layer protected the GaN film from oxidation. 38
Figure 2.11: Ion currents for: (a) m/z= 16 and 17; (b) m/z=2; (c) m/z=15 and 18; and (d) m/z=69 and 70 during the GaN growth on Si(111) wafers after the end of the HABS exposure. The electron current is turned on at ~75 s and reaches its maximum value at ~100 s. 41
Figure 2.12: Ion currents for (a) m/z=2 and (b) m/z=69 versus electron beam energy during the electron exposures during GaN growth on Si(111) wafers. The ion currents were nearly identical after the TMG/H and NH_3 reactions. 43
Figure 2.13: Alternative growth mechanism for electron-enhanced GaN growth using sequential surface reactions. 49
Figure 3.1: Proposed growth mechanism for Si electron-enhanced atomic layer deposition (EE-ALD) using disilane as the reactant. 55

Figure 3.2: Schematic of experimental apparatus showing sample load lock, main chamber and sample analysis chamber. 57
Figure 3.3: Si EE-ALD on an Al_2O_3/Si(111) substrate displaying a growth rate of 0.15 Å/cycle after an initial nucleation period of ~35 cycles. Electron energy was 50 eV, electron exposure time was 60 s, and Si_2H_6 dose pressure was 0.15 mTorr for <300 ms. 62
Figure 3.4: Film thickness versus number of reaction cycles for electron energies of 30, 88 and 150 eV. Electron exposure time was 60 s and Si_2H_6 dose pressure was 0.15 mTorr for <300 ms. 63
Figure 3.5: Growth rate for Si EE-ALD films versus electron energy. Electron exposure time was 60 s and Si_2H_6 dose pressure was 0.15 mTorr for <300 ms. 65
Figure 3.6: Growth rate versus Si_2H_6 dose pressures for exposure times of <300 ms. Electron energy was 100 eV and electron exposure time was 60 s. 67
Figure 3.7: Growth rate of Si EE-ALD films versus electron exposure times. Electron energy was 100 eV and Si_2H_6 dose pressure was 0.15 mTorr for <300 ms. Silicon growth rate was proportional to $(1 - e^{-t/\tau})$. Hydrogen ESD cross section determined from τ was $\sigma = 5.8 \times 10^{-17}$ cm^2. 68
Figure 3.8: AES analysis of film grown using 1300 Si EE-ALD reaction cycles. Electron energy was 100 eV, electron exposure time was 60 s, and Si_2H_6 dose pressure was 0.15 mTorr for <300 ms. 74
Figure 3.9: XPS depth-profile of film grown on Si(111) wafer with a $Zn_{0.55}Mg_{0.45}O$ ALD buffer layer using 1000 Si EE-ALD reaction cycles. Electron energy was 100 eV, electron exposure time was 60 s, and Si2H6 dose pressure was 0.15 mTorr for <300 ms. 76
Figure 3.10: Photo of growth area on Si(111) wafer with a ~200 Å Al_2O_3 ALD buffer layer. Film was grown using 1350 Si EE-ALD reaction cycles. Electron energy was 50 eV, electron exposure time was 60 s, and Si_2H_6 dose pressure was 0.15 mTorr for <300 ms. 77
Figure 3.11: Film thickness versus spatial position for growth area observed in Figure 3.10. Film thickness is uniform over most of the region exposed to the electron beam. 79
Figure 4.1: Linear growth rate of EE-ALD BN films on Si(111) substrate observed with respect to three different electron energies. 92
Figure 4.2: Growth rate dependence of EE-ALD BN films on Si(111) substrate based on electron energy used during each exposure. 93
Figure 4.3: Self-limiting BN EE-ALD film growth is observed for borazine exposures greater than 7×10^{-2} Torr s. 95
Figure 4.4: Self-limiting BN EE-ALD film growth rate is observed for electron emission currents greater than 100 μA. 96

Figure 4.5: Growth rate shows self-limiting behavior with respect to the electron exposure time on the sample. Data is fit in order to determine the time constant, τ, which allows for the calculation of the electron stimulated hydrogen desorption cross section. The cross section was found to be 3.9×10^{-14} cm^2. 97
Figure 4.6: Picture of BN film grown at 27 ˚C on a Si(111) substrate. 99
Figure 4.7: Spatial spectroscopic ellipsometry profile of the BN EE-ALD growth spot pictured in Figure 4.6 shows good conformality across the region that was exposed to electron flux. 101
Figure 4.8: XPS depth profile of a BN EE-ALD film grown on Si(111). Film shows consistent composition throughout the bulk with approximately 56 at.% B and 40 at.% N. The film shows approximately 3 at.% C and 1 at.% O contamination throughout bulk. 102
Figure 4.9: a) GIXRD scan of EE-ALD BN film grown at 100 ˚C shows polycrystallinity consistent with hexagonal BN. Crystallite sizes are calculated to be on the order of 1-2 nm. Additionally, due to the presence of only two peaks (002) and (004), it appears that film growth is textured parallel to the substrate surface. b) XRD powder pattern of hexagonal BN for reference. 104
Figure 4.10: HR-TEM images of EE-ALD BN film grown on Si(111) at 100 ˚C. a) Hexagonal and turbostratic BN film shows texturing with the (002) basal plane parallel to the substrate surface. b) Interface of the Si(111) substrate and EE-ALD BN film shows an ~1 nm amorphous BN layer before the formation of the hexagonal and turbostratic BN film. 107
Figure 4.11: Proposed EE-ALD BN growth mechanism 109
Figure 4.12: EE-ALD BN film growth on trench structure at 27 ˚C. Top pane: STEM image shows thick BN film deposition on top of trench structure with some film deposition on trench sides and bottom. Bottom panes: EELS for B, N, Si, O and a false-colored, combined elemental map. BN films deposited into trench preferentially on the bottom and sloped sides. More vertical regions experienced very little film growth. 110
Figure 5.1: SEM image of the electron flood gun disc after filament failure. Pitting and surface morphology changes are evident. 118
Figure 5.2: EDS elemental mapping of disc shown in Figure 5.1. Images show loss of oxygen from the yttria layer and addition of silicon to the disc face. 119

Chapter 1: Introduction

I. Atomic Layer Deposition

A. Basics

Atomic layer deposition (ALD) is a versatile technique that allows for the growth of ultra-thin films that are conformal and pinhole free with Ångstrom-level control. Film growth is achieved through repeated sequential exposures of gaseous reactant molecules.[4] Reactant molecules (precursors) must possess a reasonable vapor pressure at temperatures between 25 - 200 °C and exhibit no intermolecular reactions with itself. Typically, two or more precursors are used for ALD film growth. These precursors are chosen based on the energetic favorability of their chemical reactions. Without a favorable chemical reaction, where each precursor creates a layer reactive to the next precursor, ALD growth cannot proceed.

ALD film growth commonly occurs within a vacuum chamber, although atmospheric pressure techniques are becoming more common.[4-6] Precursors are exposed to the substrate and allowed to react with the surface in a sequential fashion. Each precursor exposure is separated by either a time-delayed inert gas purge (temporal ALD) or a high-pressure inert gas physical zone (spatial ALD). This separation allows the precursor to react only with the exposed surface resulting in monolayer film deposition that self-limits once all reactive surface sites are consumed. Surface coverages for a single dose are theoretically up to 100 %; however, it is common for practical surface coverages to be lower.[4] Each monolayer that is deposited changes the character of the surface reactive sites and promotes film growth for the following precursor exposure as shown as Figure 1.1. Here precursor A reacts with surface sites until they have all been consumed. The resulting surface has different reactive sites that are incompatible to further reaction with precursor A. Precursor B is chosen based on being compatible for reaction with surface sites left by precursor A. These surface sites are consumed until a monolayer from

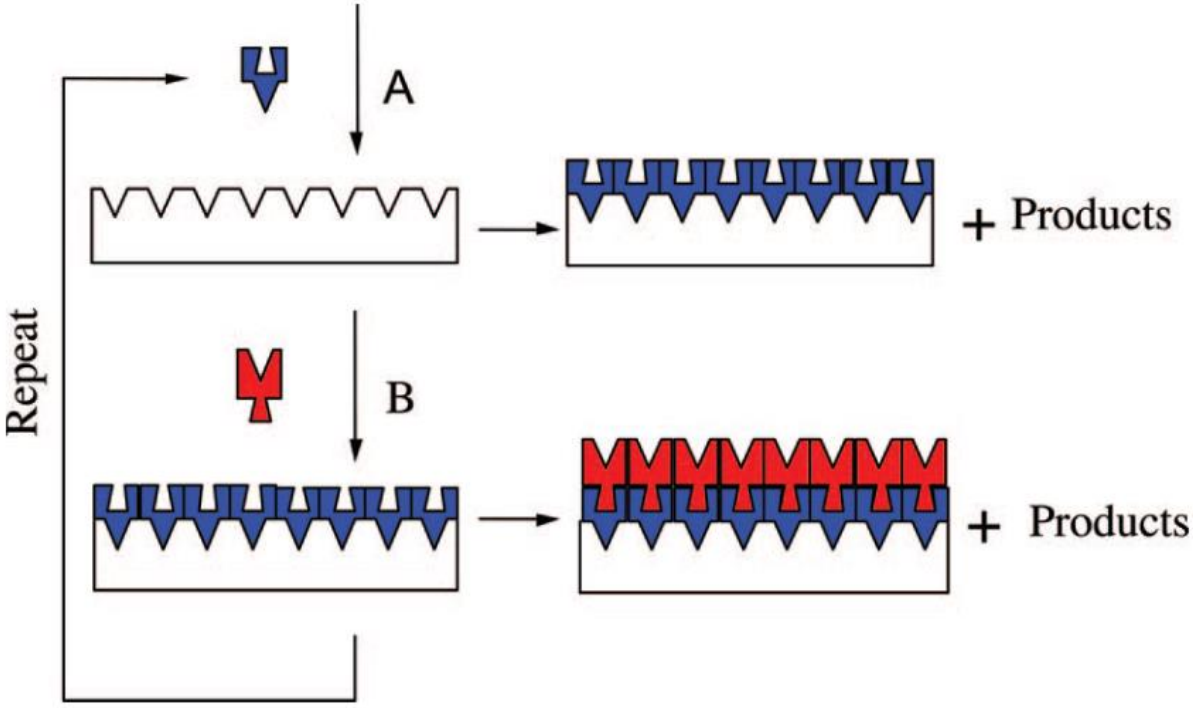

Figure 1.1: Cartoon for an ALD process using sequential dosing of precursors A and B. ALD relies on self-limiting surface modifications for monolayer growth control.[2]

precursor B is formed at which point the reaction again self-limits. At this point, the surface sites have been regenerated to react with precursor A. These "AB" reaction sequences can be repeated until the desired thickness is achieved. It is possible to achieve films that are a single monolayer as well as films that are hundreds of nanometers thick with ALD.

One of the greatest advantages of ALD as a thin film deposition technique is its ability to coat surfaces conformally regardless of substrate geometry.[4] Since ALD employs gas-phase precursors, a thin film will coat any zone on the substrate, including trenches, into which the gas molecules can diffuse. Assuming proper precursor separation is observed, conformal film thickness will be observed throughout the entire ALD film. Figure 1.2 shows an ALD Al_2O_3 film deposition of 300 nm on a patterned Si trench structure.

ALD processes presently exist for many materials within the oxide, nitride, carbide, sulfide, fluoride and metallic families.[4,7-10] Additionally, organic based materials such as polymers and biomaterials can be deposited with a variation of ALD called molecular layer deposition (MLD).[4,11] Finally, it is possible to create varied film structures such as nano-laminates and doped materials through varying the relative number of ALD cycles or chemical reactions.[4,12,13]

B. Applications

ALD films with many varied properties are possible due to the flexibility in choosing precursors and engineering reaction chemistry. Currently, coatings with insulating, semiconducting, conducting, dielectric, magnetic and refractive properties are available for ALD.[4,7,10,13] Additionally, ALD has flexibility in the substrate on which films can be deposited.[4] Many substrate materials have been used to date including metals, ceramics, semiconductors, polymers,[14] fabrics,[15] particles[16] and nanotubes.[17]

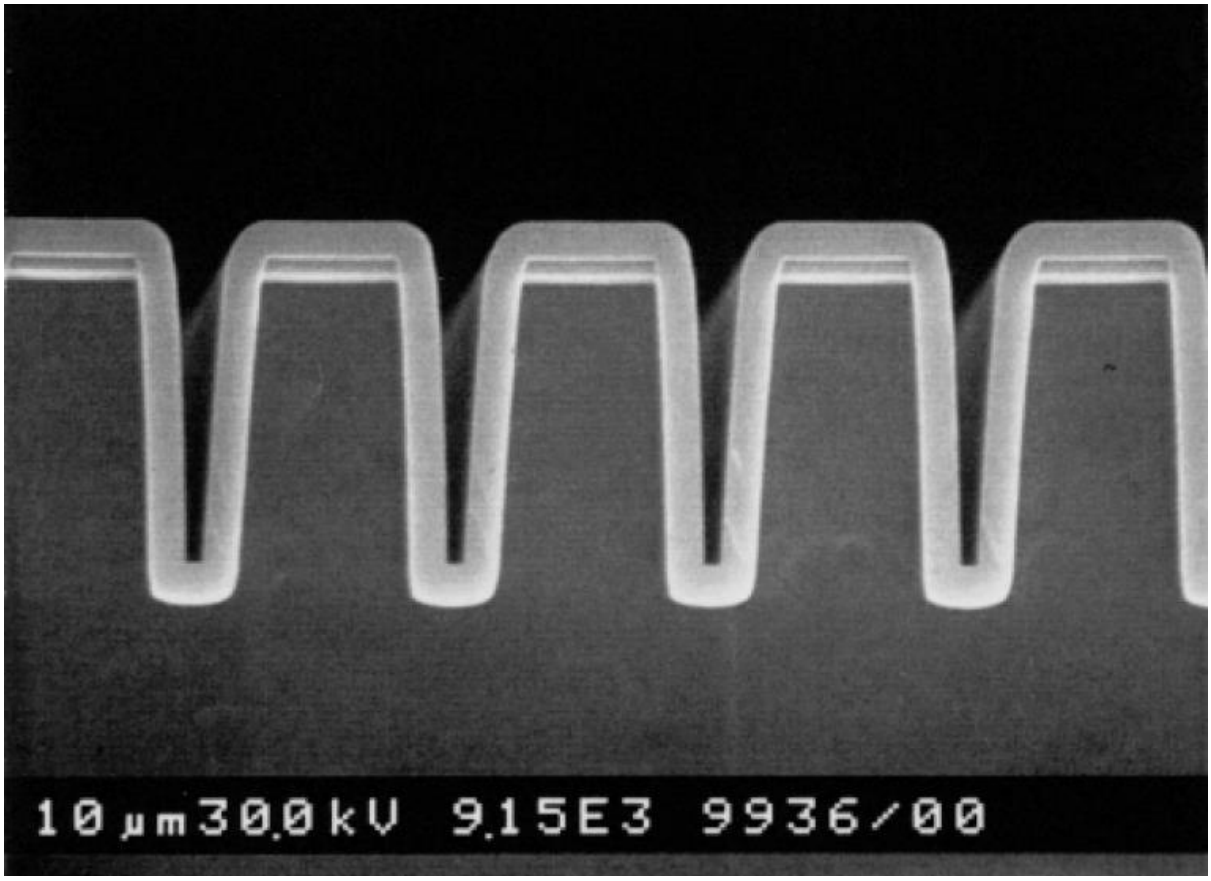

Figure 1.2: Cross-sectional SEM image of an Al_2O_3 ALD film growth on a patterned trench structure demonstrates the high levels of obtainable conformality with ALD.[3]

With this flexibility in materials and substrates, ALD has a growing industrial presence in microelectronics, batteries, solar cells, pharmaceuticals and biomedical applications. ALD is employed in microelectronics to fabricate high-k dielectrics for metal-oxide-semiconductor field-effect transistors (MOSFET), metal barriers and gate metals, metal interconnects and dynamic random access memory (DRAM) capacitors.[18] The main advantage of ALD for this application is the conformality of ultra-thin films over complex structures and the ability to engineer film properties while reducing microelectronic dimensions. There is interest in ALD for batteries as there is potential to use these films in lithium ion batteries, super capacitors and fuel cells to mitigate the capacitance loss as cells age due to cycling.[19-21] ALD films serve two main purposes in solar cell applications: as flexible barriers to prevent oxidative deterioration from water vapor and as a buffer layer to reduce charge recombination energy loss.[22] Finally, pharmaceutical and biomedical fields are applying ALD films for enhancing powder handling, controlling time delay dosing and as a surface modification for implants.[23,24]

C. Limitations

There are still many materials for which a viable ALD process does not exist. This is generally due to either the lack of safe precursors compatible with ALD reaction requirements, unreactive precursors at desired reaction temperatures or the material quality of produced ALD films not being sufficient for the desired application. Generally, a chemical vapor deposition (CVD) or molecular beam epitaxy (MBE) process can be employed to deposit the desired film. However, these techniques lack the growth rate control and conformality of an ALD process. For example, high aspect ratio structures are difficult to coat without the control of an ALD process. Additionally, CVD and MBE processes typically require much higher temperatures for quality film deposition to occur. Typically, ALD processes can be run under 300 °C, while CVD and MBE process temperatures commonly exceed 800 °C.[25] These elevated temperature

requirements make it impossible to deposit films on thermally sensitive substrates such as some polymers. Furthermore, surface roughening and interfacial alloying can occur at elevated temperatures resulting in degraded film quality.[26,27] It is desirable to work toward low temperature ALD alternatives for these CVD and MBE processes.

II. Non-Thermal Atomic Layer Deposition

A. Mechanisms for Enhancement

Elevated temperatures allow many surface reactions to be energetically favorable for normally unreactive ALD precursors. However, elevated temperatures are often undesirable in thin film growth. It is possible to substitute the thermal energy source that drives these reactions with an alternative source of energy. Possible non-thermal energy sources include using ion, photon or electron fluxes across the surface.

The use of ions is already popular in the form of plasma-enhanced ALD (PEALD). PEALD utilizes a plasma (typically H_2, N_2 or O_2) to generate highly reactive radical fluxes across the substrate surface.[4,28] The majority of films deposited by PEALD are metal oxides, metal nitrides and pure metals.[4,28] PEALD offers many benefits including reduced reaction temperature, access to new precursors and chemistries, and increased growth rates.[28] However, a persistent limitation of PEALD occurs in the form of plasma-induced damage to the film. This damage can result in surface modification and defect formation which deteriorates film quality for some applications.[28] Additional damage can occur to sensitive substrates during the initial reaction cycles.

Several photochemical ALD (pc-ALD) processes have been described for common metal oxides.[29] These processes are considered to require ultraviolet (UV) light sources to provide the necessary photon energy to stimulate surface reactions.[29] However, it is difficult to find suitable

light sources with sufficient intensity.[29] While initial work in pc-ALD shows promise in promoting enhanced electrical properties in ALD films at reduced reaction temperatures, photo-driven processes' main application remains lithography and patterning.

Prior to this work, electron fluxes across the substrate surface had not been employed to stimulate ALD surface reactions. Therefore, electron-enhanced atomic layer deposition (EE-ALD) will be the focus of this work.

III. Electron Enhanced Atomic Layer Deposition

A. Electron Stimulated Desorption

Electron stimulated desorption (ESD) can occur on surfaces that have been exposed to an electron flux. Typically, ESD will result in desorption of hydrogen species from the surface; however, it is possible for other species to be removed as well. The surface will then have "dangling" bonds remaining from the desorption process. A "dangling" bond is a highly reactive, unpaired electron on an immobilized atom.[30] These "dangling" bonds will readily react with gas molecules that adsorb on the surface. Thus, it is possible to replace the thermal energy component of these reactions.

ESD has been found to occur through two main pathways described by the Menzel-Gomer-Redhead mechanism and the Knotek-Feibelman mechanism. The Menzel-Gomer-Redhead mechanism is pictured in Figure 1.3. It describes how the incident electron flux transfers energy to valence, bonding electrons on the surface. These electrons are excited into an antibonding orbital, which as the electron relaxes down its potential energy curve, results in the dissociation of the surface bond.[31,32] The surface bond of interest for these studies is the hydrogen bond to silicon, gallium nitride or boron nitride. Once the dissociation occurs, radical hydrogen species can react and leave the surface as H_2. The remaining electron from the

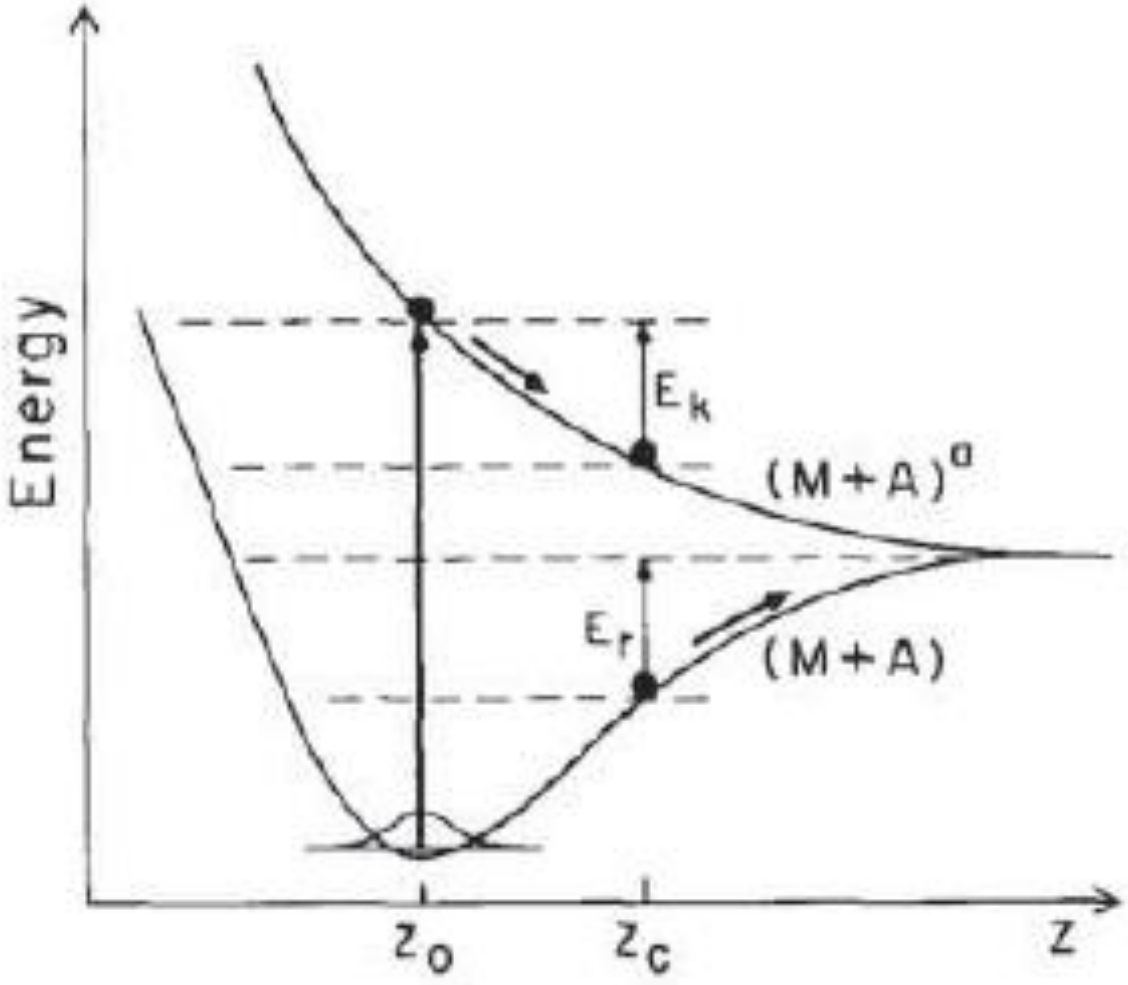

Figure 1.3: Menzel-Gomer-Redhead mechanism for electron stimulated desorption.[1]

dissociated bond becomes the dangling bond site that will be used for precursor adsorption. The second possible mechanism for ESD processes to occur through is the Knotek-Feibelman mechanism pictured in Figure 1.4. The Knotek-Feibelman mechanism describes an Auger process of bond dissociation. An incident electron on the surface with energy equal to or greater than the energy of a core level orbital will knock that core level electron out of its atom. The remaining electron hole will be filled by a valence level electron releasing energy and falling down into it. In order to conserve energy, another valence electron will absorb the released energy and become energetically excited enough to escape the atom.[33] With the loss of these valence, bonding electrons, hydrogen can be dissociated from the surface leaving the surface highly reactive.

B. Ultra-high Vacuum Reactor Design

Due to the highly reactive nature of the "dangling" bonds generated through ESD, it is imperative that this chemistry proceeds in a clean environment. "Dangling" bonds should react indiscriminately with any gaseous species present including water and oxygen. Such side reactions would generate film impurities and reduce the efficiency with which films are grown, as competition exists for reactive sites. Additionally, a clean system will preserve the lifetime of the "dangling" bonds allowing for more flexibility in reaction parameters. To achieve this goal, a specialized ultra-high vacuum (UHV) reactor was designed and built on site to perform EE-ALD. UHV pressures are typically considered to be 10^{-9} – 10^{-12} Torr. For comparison, lunar pressure fluctuates around 10^{-12} Torr and pressure in interstellar space is < 10^{-17} Torr.[34,35]

The reactor is set up in three sections that are isolated from each other: a load lock chamber, a reaction chamber and an analysis chamber. The base pressure of the EE-ALD reaction chamber is 10^{-10} Torr. The load lock chamber is set up to load samples while removing atmospheric gases and desorbing excess water from surfaces to maintain the integrity of the

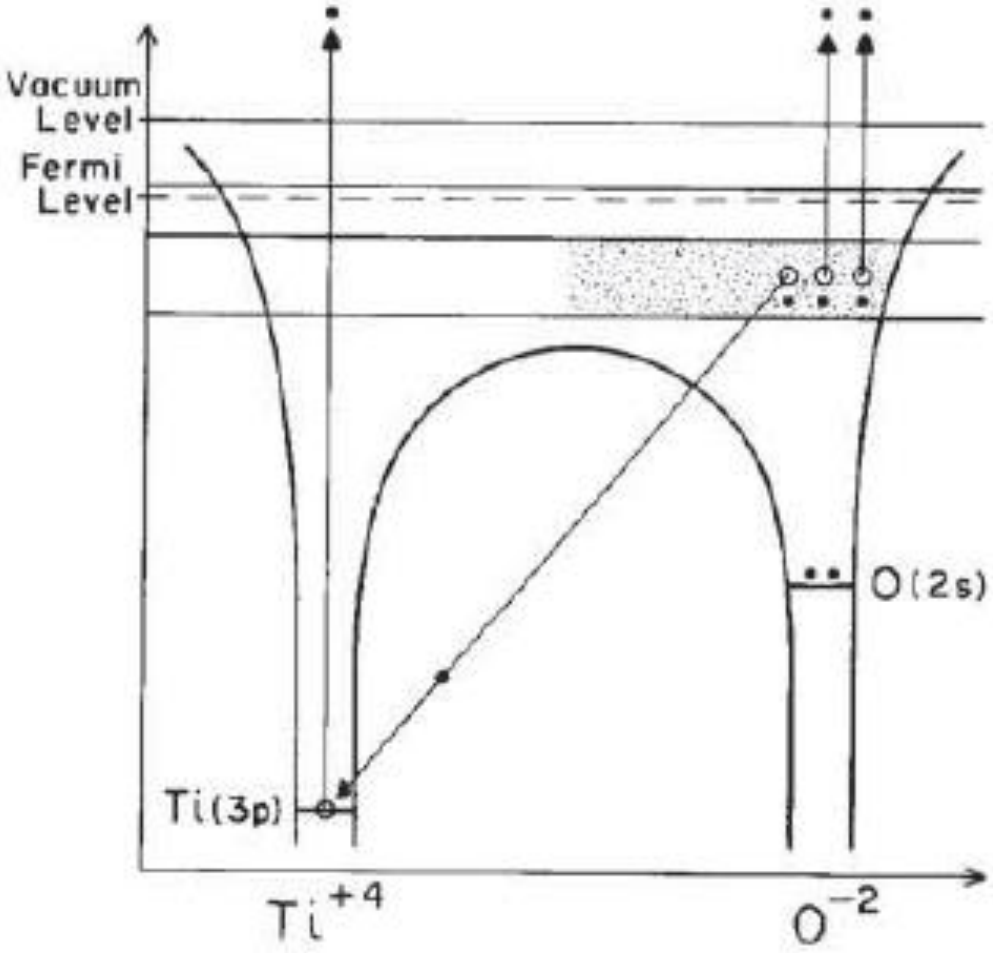

Figure 1.4: Knotek-Feibelman mechanism for electron stimulated desorption.[1]

vacuum in the reaction chamber. Samples can be moved between chambers with a magnetically coupled transfer arm. The reaction chamber is equipped with *in situ* analysis techniques including ellipsometry to monitor film thickness and mass spectrometry to identify species coming off the reaction surface. EE-ALD reactions are performed using an electron flood gun as the electron source and micro-pulse valves to introduce precursors. Behind the micro-pulse valves is a dosing manifold that allows for tight control over the pressure of gas introduced into the system. Finally, the analysis chamber can be accessed through the reaction chamber by another magnetically coupled transfer arm. The analysis chamber is equipped with an *in situ* Auger to monitor the composition of the film surface. An overview of the EE-ALD reactor is shown in Figure 1.5.

C. Compatible Precursors

The proposed reaction mechanism for this EE-ALD work involves the ESD of surface species as an alternative reaction pathway. Therefore, it is anticipated that any surface species with a large ESD cross section should serve as a viable reaction chemistry. This work focuses solely on the ESD of hydrogen from silicon, GaN and BN surfaces. However, hydrogen has a large ESD cross section from many materials including diamond[36] and TiO_2[37] which may allow these films to be deposited with EE-ALD in the future. Other surface species, including halogens,[38] also exhibit large ESD cross sections potentially allowing their implementation into EE-ALD processes. It is anticipated that hydrogen and halogen terminated precursors will be viable options for use in EE-ALD film depositions.

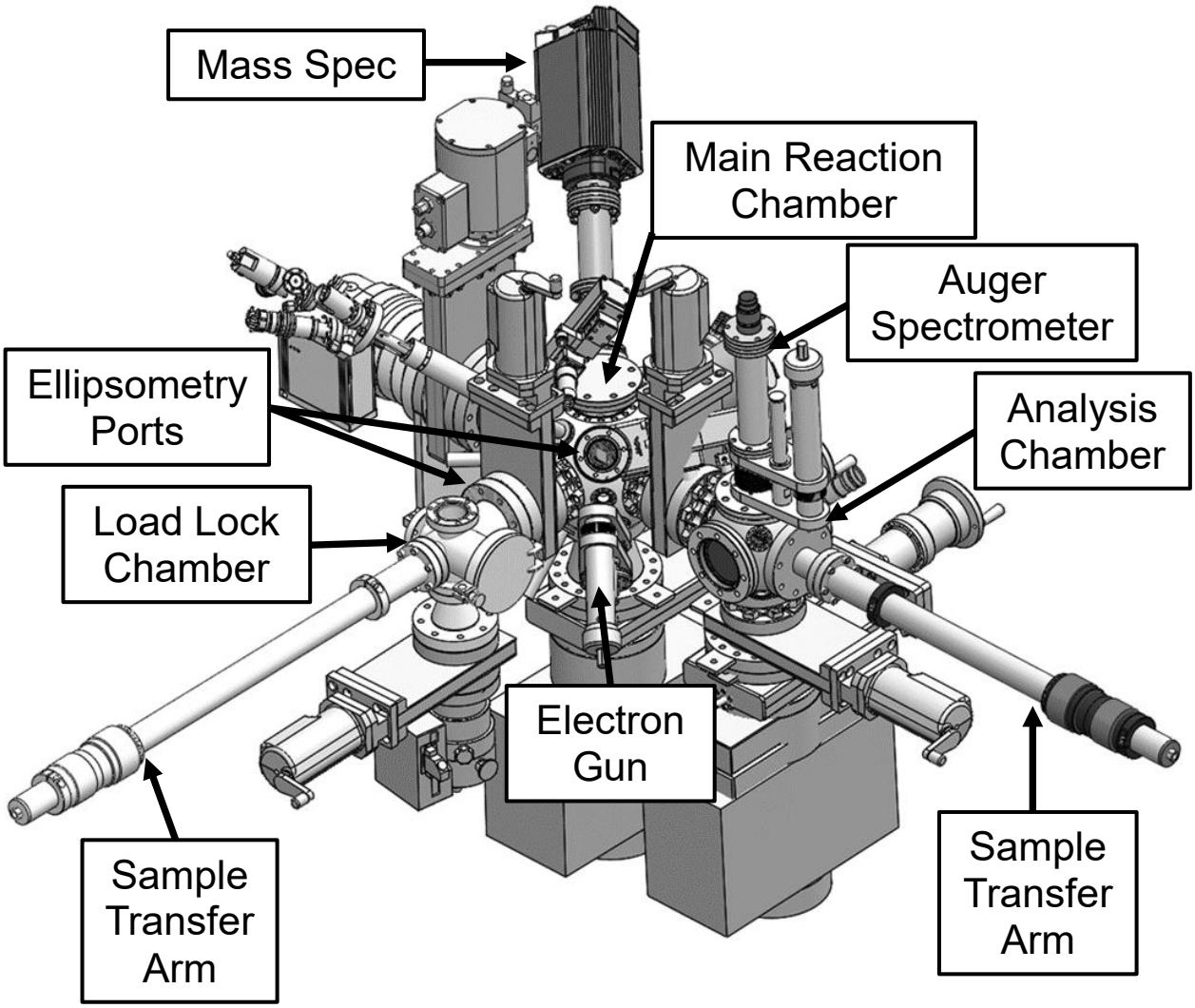

Figure 1.5: Schematic of reactor designed for this EE-ALD work.

Chapter 2: Electron Enhanced Growth of Crystalline Gallium Nitride Thin Films at Room Temperature and 100°C Using Sequential Surface Reactions[39]

Jaclyn K. Sprenger[1], Andrew S. Cavanagh[1], Huaxing Sun[1], Kathryn J. Wahl[2], Alexana Roshko[3] and Steven M. George[1,4]

[1]Department of Chemistry and Biochemistry, University of Colorado, Boulder, CO 80309; [2]Naval Research Laboratory, Washington, DC 20375; [3]National Institute of Standards and Technology, Boulder, CO 80305; [4]Department of Mechanical Engineering, University of Colorado, Boulder, CO 80309.

I. Abstract

Low energy electrons may provide mechanisms to enhance thin film growth at low temperatures. As a proof of concept, this work demonstrated the deposition of gallium nitride (GaN) films over areas of ~5 cm^2 at room temperature and 100 °C using electrons with a low energy of 50 eV from an electron flood gun. The GaN films were deposited on Si(111) wafers using a cycle of reactions similar to the sequence employed for GaN atomic layer deposition (ALD). Trimethylgallium ($Ga(CH_3)_3$, TMG), hydrogen (H) radicals and ammonia (NH_3) were employed as the reactants with electron exposures included in the reaction cycle after the TMG/H and NH_3 exposures. A number of *ex situ* techniques were then employed to analyze the GaN films. Spectroscopic ellipsometry measurements revealed that the GaN films grew linearly with the number of reaction cycles. Linear growth rates of up to 1.3 Å/cycle were obtained from the surface areas receiving the highest electron fluxes. Grazing incidence X-ray diffraction analysis revealed polycrystalline GaN films with the wurtzite crystal structure. Transmission electron microscopy (TEM) images showed crystalline grains with diameters between 2-10 nm depending on the growth temperature. X-ray photoelectron spectroscopy depth profiling displayed no oxygen contamination when the GaN films were capped with Al prior to atmospheric exposure. However, the carbon concentrations in the GaN films were 10-35 at.%.

The mechanism for the low temperature GaN growth is believed to result from the electron stimulated desorption (ESD) of hydrogen. Hydrogen ESD yields dangling bonds that facilitate Ga-N bond formation. Mass spectrometry measurements performed concurrently with the reaction cycles revealed increases in the pressure of H_2 and various GaN etch products during the electron beam exposures. The amount of H_2 and GaN etch products increased with electron beam energy from 25 to 200 eV. These results indicate that the GaN growth occurs with competing GaN etching during the reaction cycles.

II. Introduction

Gallium nitride (GaN) is an important wide band gap semiconductor that has many applications in optoelectronics[40,41] and high power electronics.[42,43] However, bulk GaN single crystals are not easily produced using conventional methods.[44] GaN devices rely on GaN heteroepitaxy on other substrates.[45] This situation increases the importance of depositing GaN using vapor phase processes such as metalorganic chemical vapor deposition[45-47] (MOCVD), hydride vapor phase epitaxy[48] (HVPE), and molecular beam epitaxy[49] (MBE) techniques. Unfortunately, these vapor phase processes require high temperatures. For example, temperatures of 800-1100 ºC are needed for GaN growth using MOCVD with trimethylgallium (TMG) or triethylgallium (TEG) and NH_3.[45-47] These high temperatures preclude GaN deposition on many thermally sensitive substrates and device structures. One goal of this work was to develop a method to lower the temperature of GaN thin film growth.

Another goal of this work was to define a GaN atomic layer deposition (ALD) process at low temperatures using sequential, self-limiting surface reactions. ALD techniques are able to deposit thin films conformally with atomic layer control.[50] The sequential surface reactions utilized for GaN ALD also allow for the addition of non-thermal enhancement between or during

the sequential reactions. Thermal GaN ALD was initially reported using either TMG or TEG and NH_3 as the reactants at temperature ranging from 450-900 °C.[51-53] The use of a hot filament to decompose the NH_3 also produced GaN ALD films at 250-350 °C using TEG and NH_3.[54] GaCl and NH_3 were used as the reactants for GaN ALD at temperatures from 350-400 °C.[55,56] Slightly higher temperatures of 500-750 °C were required for GaN ALD using $GaCl_3$ and NH_3.[57,58] TMG and a NH_3 plasma has also been used for GaN ALD at temperatures from 185-385 °C.[59,60] In this work, TMG, hydrogen (H) radicals and NH_3 were employed as the reactants with electron exposures included in the reaction sequence after the TMG/H and NH_3 exposures to lower the required temperatures for GaN ALD. TMG was employed instead of TEG because of its higher vapor pressure.

The electron exposures were used for non-thermal enhancement of GaN ALD by electron stimulated desorption (ESD).[61,62] ESD can be used to desorb a variety of surface species, such as hydrogen and halogens, from surfaces.[61,62] In particular, the ESD of hydrogen from GaN is an efficient process.[63,64] Earlier studies have reported an ESD cross section for hydrogen from GaN(0001) of 2×10^{-17} cm^2 at 90 eV.[63] This ESD cross section is much higher than previously reported ESD cross sections for hydrogen from Si(100).[65-69] ESD can occur via the Menzel-Gomer-Redhead[70,71] (MGR) or Knotek-Feibelman[72,73] (KF) mechanisms. The ESD of hydrogen will create free dangling bond sites on the surface. These dangling bond sites can be created at temperatures much lower than 250-500 °C where hydrogen desorbs thermally from GaN surfaces.[74-76] The dangling bond sites are expected to promote bond formation with other reactants with little or no activation barrier to facilitate thin film growth at low temperatures.

A similar ESD approach has been pursued for nanoscale patterning on silicon surfaces.[77] This work is based on the ability of electrons from the scanning tunneling microscope (STM) to

desorb hydrogen by ESD from silicon surfaces.[67,69,77,78] Hydrogen is observed to desorb from Si(100)-2x1 surfaces and leave behind silicon dangling bonds.[67,69,77,79] The reactive dangling bonds can adsorb other reactants such as Al, $Fe(CO)_5$ or O_2.[65,80,81] The remaining hydrogen serves as a mask to prevent adsorption. Hydrogen ESD has been employed to form Al,[81] Fe[82] and oxide[80] nanoscale patterns on Si(100) surfaces. In contrast, the approach in this paper uses ESD after sequential TMG/H and NH_3 reactant exposures to grow GaN thin films. This procedure also uses an electron flood gun for hydrogen ESD over surface areas of ~5 cm^2.

The proposed stepwise sequence of the surface reactions for low temperature GaN growth is shown in Figure 2.1. A hydrogen atom exposure after the TMG exposure is intended to replace the $–CH_3$ groups with hydrogen. Electron beam exposures at 50 eV after the TMG/H and NH_3 exposures are expected to desorb hydrogen and form dangling bonds on the GaN surface. Using this proposed stepwise sequence of reactions, GaN film growth on Si(111) wafers was conducted at room temperature and 100 °C. Because of the high reactivity of the dangling bonds, the GaN film growth was performed in an ultra-high vacuum (UHV) chamber to minimize competitive adsorption from other reactants such as H_2O. Mass spectrometry was also employed to analyze the gas species resulting from the ESD during the reaction sequence.

The GaN films were then analyzed using a variety of *ex situ* techniques. The thickness of these GaN films were measured using spectroscopic ellipsometry (SE). The crystallinity of the GaN films was characterized using grazing incidence x-ray diffraction (GIXRD). The size of the crystallites in the GaN films was established using high-resolution transmission microscopy (HRTEM). The composition of the GaN films was measured using x-ray photoelectron spectroscopy (XPS). These analysis techniques can reveal if low temperature growth of crystalline GaN films is possible using electron enhancement at low electron energies of 50 eV.

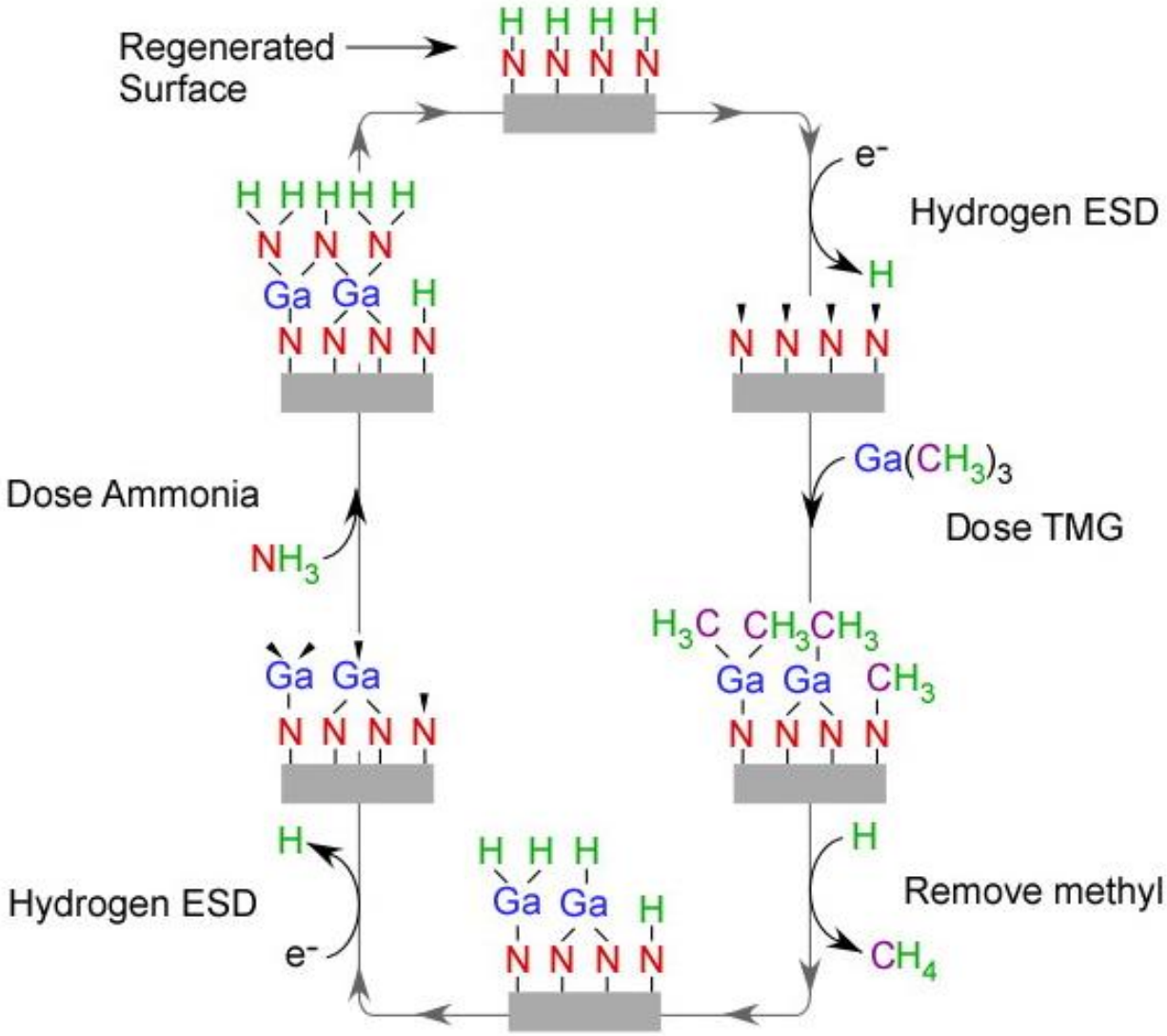

Figure 2.1: Proposed growth mechanism for electron-enhanced GaN growth using sequential surface reactions.

III. Experimental

A. Vacuum Chamber

The low temperature GaN film growth was conducted in an UHV chamber that was attached to a load lock chamber. Figure 2.2 shows a schematic of the UHV chamber and the load lock. The core of this UHV chamber is a 4.5" spherical cube (Kimball Physics Inc.). A magnetic sample transfer arm (Thermionics) is attached to the load lock chamber. A gate valve separates the load lock and main chamber. The chamber was pumped with a turbomolecular pump (HiPace 300C, 260 L/s for N_2, Pfeiffer Vacuum Technology AG) during the reaction cycles and additionally with an ion pump (TiTan 100L Variable Element, 100 L/s, Gamma Vacuum) between experiments.

The sample stage (Thermionics) was heated using a temperature-regulated filament. This filament was controlled using a LabVIEW-based proportional-integral-derivative (PID) control. Without heating, the temperature of the sample stage was at room temperature. With the filament heating, the sample stage could be raised to 400 °C. The sample stage included three compression clips that secured the Si(111) wafers and a thermocouple to measure the temperature. The sample stage was grounded to prevent charge build-up.

A beam of low energy electrons was produced using an electron flood gun with an yttria-coated iridium filament (Model EGA-1012, Kimball Physics Inc.). The electron flood gun could produce electron energies from 5-1000 eV at electron currents from 1-2000 μA. Electrons from the electron gun were incident on the Si(111) substrate at 55 ° from the surface normal. The distance between the end of the electron gun and the Si(111) substrate was approximately 2.5 cm. Each electron beam exposure was conducted for ~120 s. The chamber pressure during the electron exposures was $\leq 1 \times 10^{-7}$ Torr.

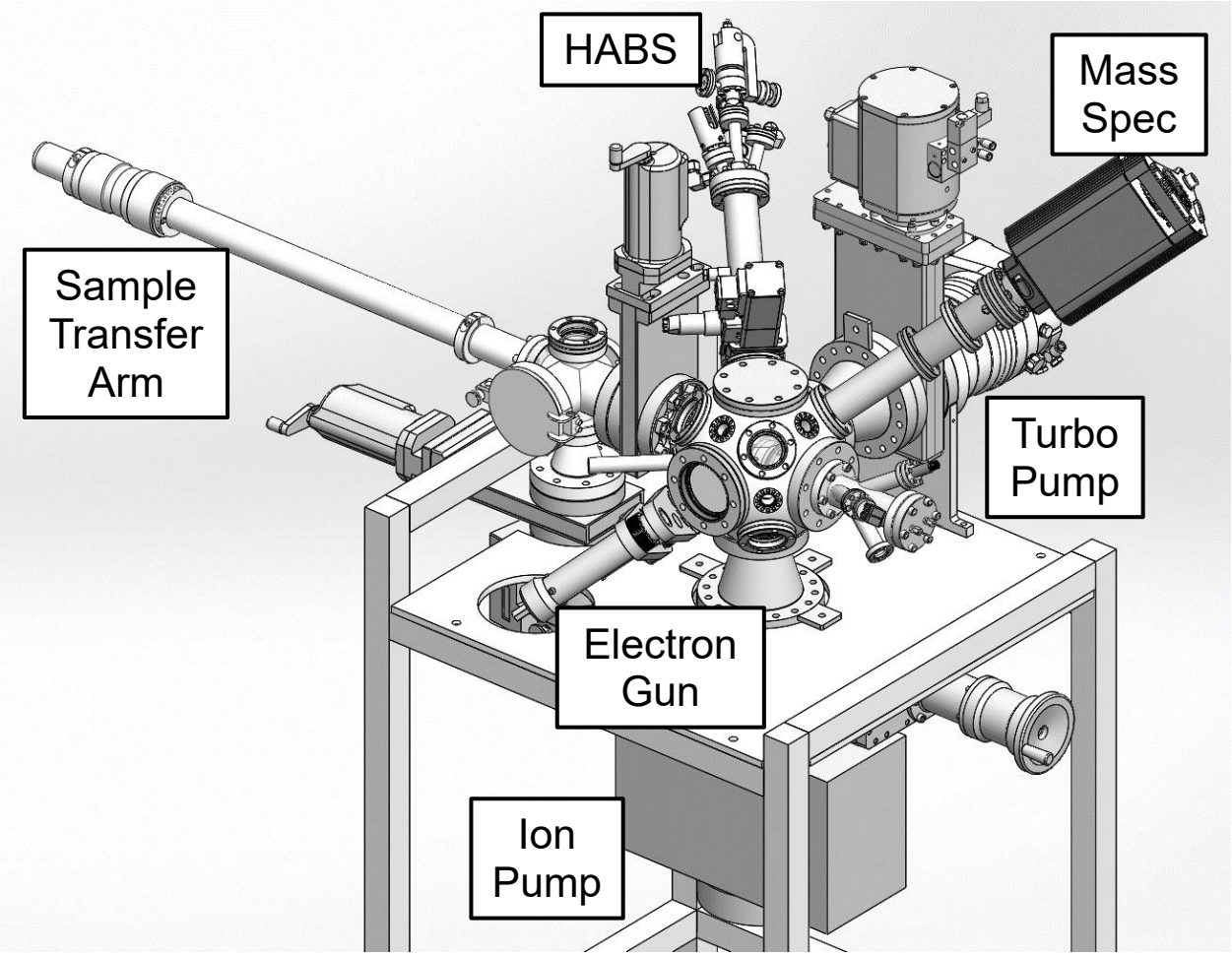

Figure 2.2: Experimental schematic of vacuum apparatus.

Precursors were introduced into the UHV chamber through miniature micro-dispensing pulse valves (Parker Hannifin Corp.). Prior to introduction, the NH_3 and H_2 lines were passed through hydride and hydrogen gas purifiers (Entegris Inc.), respectively. The valves were open for 100 ms to dose the TMG and NH_3 precursors. The pressure transients in the vacuum chamber during the TMG and NH_3 exposures were each ~1 mTorr.

A hydrogen atom beam source (HABS) (MBE-Komponenten GmbH) was used to produce the hydrogen radicals. The hydrogen radicals were formed by cracking H_2 using a tungsten capillary at 1900 °C. The chamber pressure during the hydrogen atom beam exposure was ~ 1 x 10^{-5} Torr with ~ 1 sccm of H_2 flowing through the HABS. The working distance from the end of tungsten capillary in the HABS to the Si(111) substrate was ~20 cm. The hydrogen radical flux was incident on the Si(111) substrate at an angle of 55 ° from surface normal. The HABS was expected to have a flux of 1-5 x 10^{15} H-atoms cm^{-2} s^{-1} based on the operating conditions. Hydrogen radical exposures covered a surface area of ~5 cm^2. The hydrogen atom exposure time was typically 100 s. Shorter hydrogen atom exposure times led to more carbon incorporation in the GaN films.

The UHV chamber also was equipped with a mass spectrometer (PrismaPlus QMG 220M with C-SEM detector, Pfeiffer Vacuum Inc.). This mass spectrometer could measure mass signals up to m/z = 200 amu. This mass spectrometer also has an internal ion current to pressure calibration that allows partial pressures to be estimated from ion currents. The mass spectrometer is located in the top right-hand side of Figure 2.2. The HABS is positioned just left of center in the top portion of Figure 2.2. The electron gun is shown in Figure 2.2 in the front lower left of the UHV chamber. A z-translation stage allowed the electron flood gun to be extended and retracted to accommodate the sample transfer arm. The ion pump is located

underneath the main UHV chamber. The turbomolecular pump is positioned in back of the UHV chamber on the right-hand side behind the mass spectrometer.

After the completion of most of the work presented in this paper, an *in situ* ellipsometer (Film Sense, FS-1 Multi-Wavelength Ellipsometer) was installed on the chamber. This *in situ* ellipsometer provided a method to study the effect of reaction parameters on the growth rate of the GaN film. In addition, the experimental apparatus was also upgraded to include a small second chamber where the sample could be analyzed using Auger electron spectroscopy using a cylindrical mirror analyzer (RBD Instruments, microCMA Compact Auger Analyzer). This Auger spectroscopy analysis chamber was separated from the main chamber by a gate valve. The sample could be moved between the main chamber and the Auger spectroscopy analysis chamber using a magnetic transfer mechanism.

B. Chemicals and Materials

GaN films were grown using trimethylgallium ($Ga(CH_3)_3$; 99.9999%, electronics grade, Strem), ammonia (NH_3; 99.999%, anhydrous, Airgas) and hydrogen (H_2; research grade, Airgas). Films were deposited on boron-doped Si(111) substrates (Silicon Valley Microelectronics, Inc.). The substrates were rinsed with acetone and methanol, and cleaned with Nano-Strip (Cyantec Corporation). The silicon native oxide was removed and the surface was hydrogen-passivated using dilute hydrofluoric (HF) acid (50:1 H_2O:HF).[9-11]

The silicon substrate on the sample stage was loaded into the load lock chamber and the background pressure was reduced to $1x10^{-6}$ Torr. The silicon substrate on the sample stage and the surrounding load lock chamber were then UV-irradiated for 1 hour using UV lamps (RDB Instruments) to desorb water and other surface species from the silicon substrate and chamber walls.[83] After the pressure in the load lock was reduced to approximately 1×10^{-8} Torr, the silicon substrate on the sample stage was transferred into the main chamber. The silicon

substrate on the sample holder and the main chamber were again irradiated with UV light for 1 hour. Prior to deposition, the Si(111) wafer was also cleaned using a 100 s hydrogen atom beam exposure at a flux of 1-5 x 10^{15} H-atoms cm^{-2} s^{-1}.

For comparison, GaN films were also deposited on the Ga-face of single-crystal GaN(0001) substrates (Kyma Technologies) provided by the Naval Research Laboratory. The Ga-face was employed because the previous studies of hydrogen ESD on GaN substrates were performed on the Ga-face of GaN(0001).[84] The GaN(0001) substrates were N+ (Si doped) with a maximum off-cut of 0.33 degrees. To clean the single-crystal GaN wafers, the samples were dipped in dilute HF (50:1 H_2O:HF) for 5 mins at 27 °C, rinsed with deionized water, dipped in Nano-strip at 80 °C for 10 mins, rinsed again with deionized water, and then blown dry with nitrogen.[85] The GaN wafers were then attached to a Si(111) wafer using 9 mm diameter carbon adhesive tape (SPI Supplies). After transfer to the vacuum chamber, the sample was further cleaned with 30 cycles of the following reaction sequence: 5 s TMG exposure; 5 s purge; 30 s HABS exposure; 5 s purge; and a 300 s HABS exposure. These conditions were close to previous *in situ* cleaning procedures reported for GaN samples.[85]

C. *Ex situ* Film Analysis

The GaN films were analyzed using a variety of *ex situ* techniques. The film thickness, index of refraction, n, and extinction coefficient, k, were determined using a spectroscopic ellipsometer (Model M-2000, J.A Woollam Co., Inc.). The SE data was fitted with a Tauc-Lorentz model using the CompleteEASE software package (J.A. Woollam Co., Inc.) to obtain the film thickness and optical properties.

The crystallinity of the GaN films was determined using grazing incidence X-ray diffraction (GIXRD) at the Naval Research Laboratory. The diffraction patterns were obtained with an x-ray diffractometer (SmartLab System, Rigaku) using Cu-Kα irradiation at an incident

angle of 0.3 °. The diameter of the GaN crystallites was estimated based on the width of the diffraction peaks using the Scherrer formula.[86]

The TEM images of the GaN films were recorded at the National Institute of Science and Technology in Boulder (NIST-Boulder). The cross sectional sample for TEM was prepared by focused ion beam (FIB) Ga milling (Auriga Dual Beam FIB, Carl Zeiss)[87] after deposition of a protective platinum layer. Low-energy Ar ion milling at 850 eV was used to remove the FIB-induced surface damage. The sample was imaged at 200 kV in a high resolution transmission electron microscope (HRTEM) (JEM-ARM200F TEM, JEOL).[87] This HRTEM contained an aberration-corrected probe for scanning transmission electron microscopy (STEM).

The film composition was determined by X-ray photoelectron spectroscopy (XPS) analysis using an X-ray photoelectron spectrometer (PHI 5600) at the University of Colorado. The spectrometer used a monochromatic Al-Kα source at 1486.6 eV. The pass energy was 29.35 eV and the step size was 0.25 eV. An electron beam neutralizer was used during the XPS measurements. XPS depth-profiling and surface carbon removal were conducted using argon ion sputtering. The XPS data was collected using Auger Scan (RBD Instruments). The XPS data was analyzed in CASA XPS (Casa Software Ltd.).

IV. Results and Discussion

A. Film Growth and Characterization Using Spectroscopic Ellipsometry

The GaN films were grown at room temperature (27 °C) and 100 °C using the stepwise sequence of exposures shown in Figure 2.1. The exact reaction sequence was: TMG pressure transient of ~1 mTorr; purge of 15 s; HABS exposure of 100 s; purge of 90 s; electron exposure of 120 s; NH_3 pressure transient of ~1 mTorr; purge of 90 s; and electron exposure of 120 s. The

electron energy was 50 eV and the electron emission current from the filament was 150 μA. The electron current incident on the sample during the electron exposures was ~75 μA for 120 s.

Figure 2.3 shows a photo of a GaN film on a Si(111) wafer after 600 reaction cycles at 27°C. The GaN film was clearly visible on the Si(111) wafer and appeared as a gradient of colors ranging from light blue to dark brown. This GaN film has dimensions of ~3.0 cm x 1.5 cm. The vacuum chamber background pressure before the 600 cycles was 5×10^{-9} Torr. During the purge portion of the reaction sequence, the background pressure increased to ~2×10^{-8} Torr during the 600 cycles.

After the GaN film growth, *ex situ* spectroscopic ellipsometry was used to measure the film thickness on the Si(111) wafer. Film thicknesses varied across the Si(111) wafer from 80 nm close to the electron gun to 30 nm away from the electron gun. This range of film thicknesses is attributed to the varying electron beam flux across the surface. The electron gun emits electrons in a Gaussian spatial distribution. The incident electron flux was 55^{o} from the surface normal of the Si(111) wafer. The electron beam also is diverging because of space-charge effects that are more severe at low electron energies. These factors cause the electron beam diameter to increase with propagation distance from the electron gun. The electrons impacting the far side of the Si(111) wafer travel approximately twice the distance from the electron gun source as electron impacting the near side of the Si(111) wafer. More uniform film thicknesses would be obtained with incident electron fluxes that are normal to the surface. However, these incident electron fluxes from the electron gun would still have a Gaussian spatial distribution. Electron fluxes that are even more uniform could also be obtained by extracting electrons from the positive column of a DC glow discharge plasma.[88]

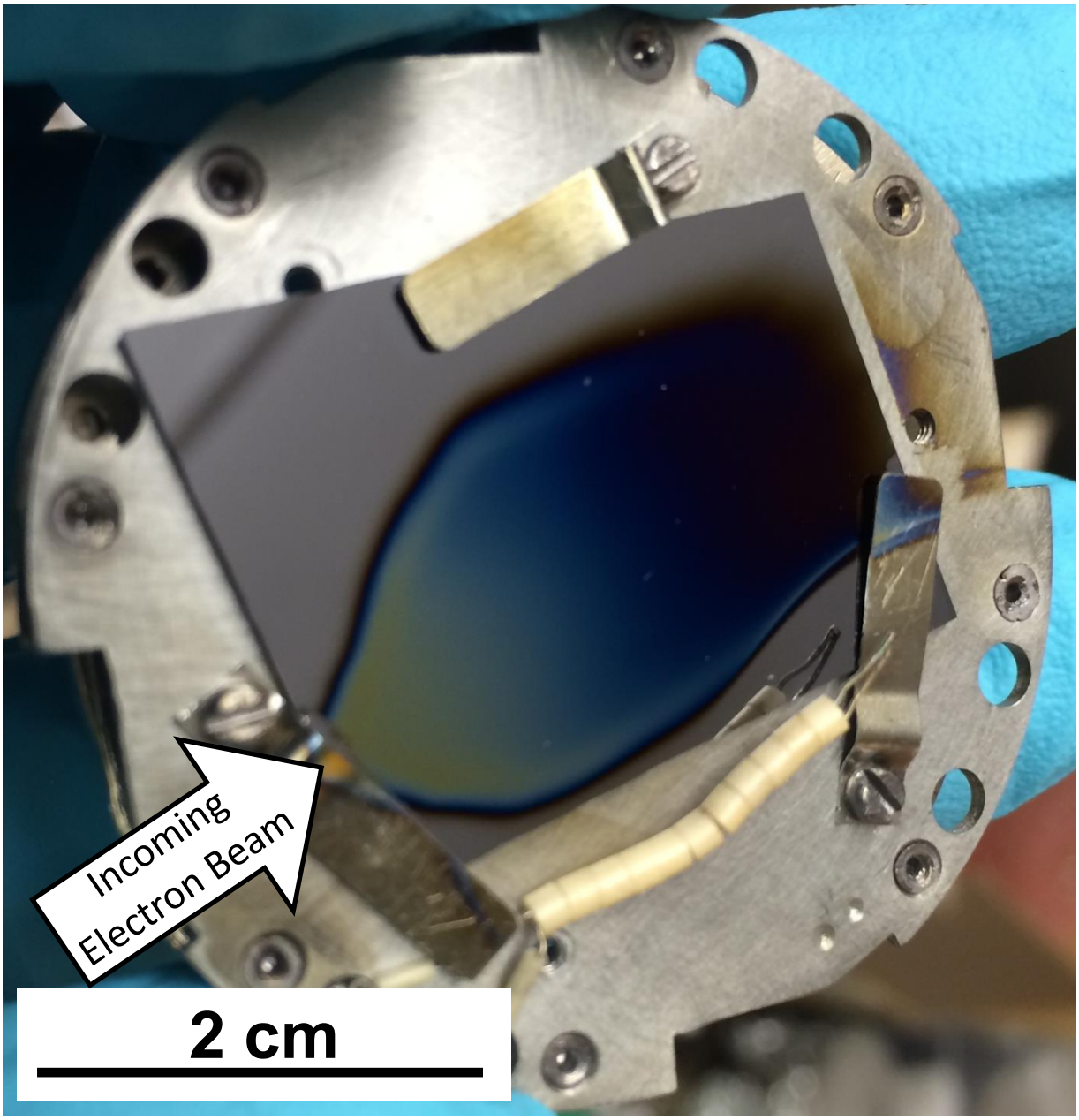

Figure 2.3: Photo of GaN film grown on Si(111) substrate at 27 °C.

To determine GaN film growth rates on the Si(111) wafer, the film thicknesses were measured using spectroscopic ellipsometry at various positions along the gradient as shown in Figure 2.4a. Thickness measurements were performed after 150, 250, 300, 400 and 600 reaction cycles and are summarized in Figure 2.4b. Figure 2.4b reveals that there is a linear increase in film thickness versus number of reaction cycles. The slight deviations from linearity for the thicknesses after 250 and 400 cycles may be caused by the difficulty in manually replicating the same locations on the various samples. The growth rate varied from 0.9 to 1.3 Å /cycle across the three positions shown in Figure 2.4a. Slightly smaller GaN growth rates were also observed at 100 °C.

The measured GaN growth rates from 0.9 to 1.3 Å /cycle at room temperature are believed to be obtained under self-limiting reactant exposures. Additional in situ ellipsometry measurements performed after the completion of the experimental results displayed in Figure 2.4 revealed that the ~1 mTorr pressure transients for the reactants were sufficient for the surface reactions to reach completion. In contrast, the GaN growth rate dependence on electron exposure time was not self-limiting. The in situ ellipsometer experiments have revealed that the GaN growth rate increases for longer electron exposure times. The rate of increase does begin to level off for electron exposure times >60 s. However, the GaN growth rate is still increasing for electron exposure times as long as 250 s. This behavior is consistent with only a small loss of hydrogen coverage resulting from hydrogen ESD as discussed later in Sect. IV.F.

The GaN growth rates from 0.9 to 1.3 Å /cycle are somewhat smaller than the previous GaN growth rates reported by thermal GaN ALD. Thermal ALD experiments using TEG and NH_3 as the reactants obtained GaN growth rates of ~1.9 Å / cycle.[53] Other thermal ALD

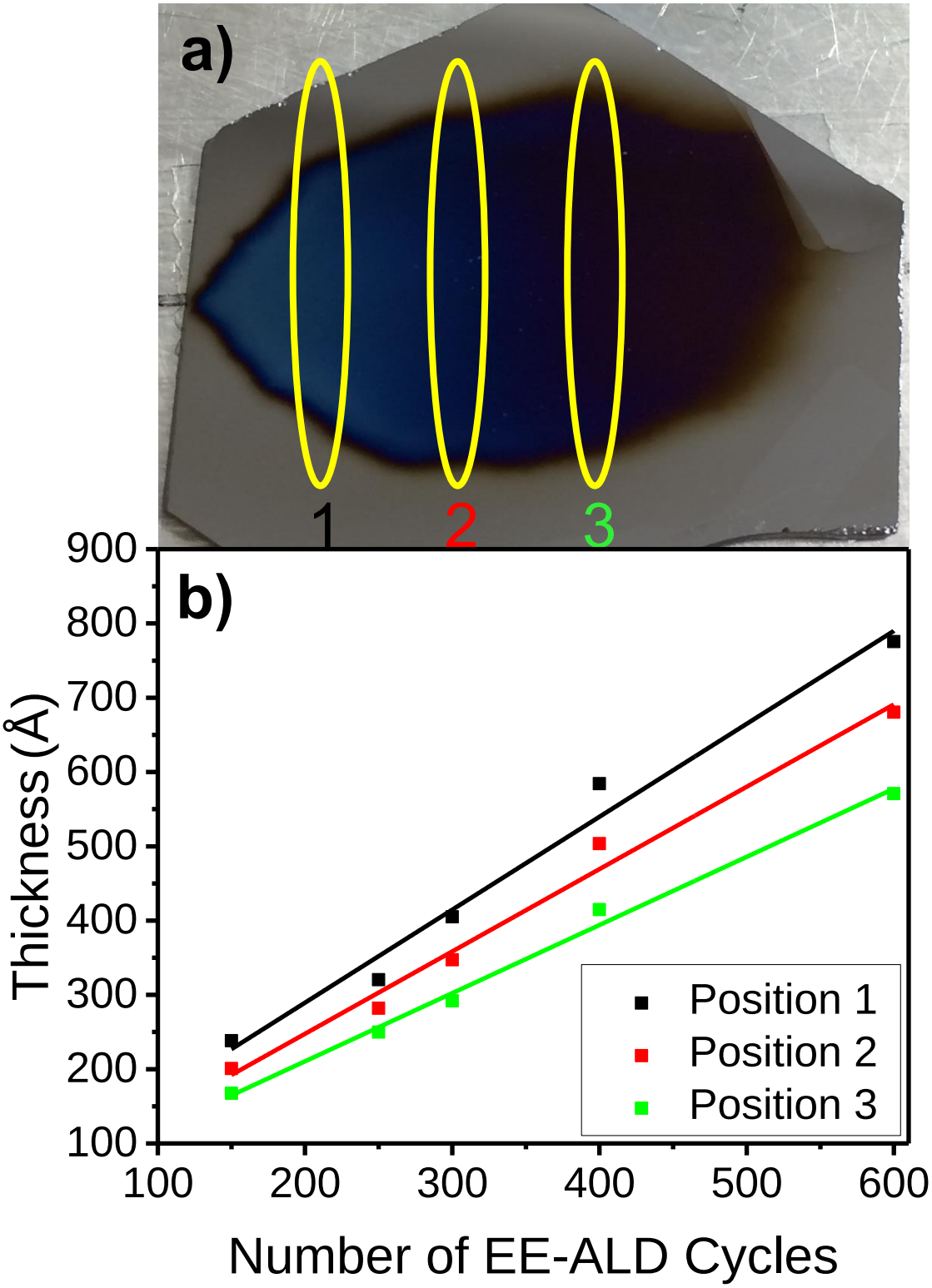

Figure 2.4: (a) GaN film on Si(111) wafer showing three positions for analysis using spectroscopic ellipsometry. (b) Thickness of GaN versus number of reaction cycles at the three positions.

investigations using $GaCl_3$ and NH_3 as the reactants have measured growth rates of ~2 Å / cycle[57] and ~3 Å / cycle.[58] Additional thermal ALD studies using GaCl and NH_3 as the reactants have obtained growth rates of ~2.5 Å / cycle.[55,56] However, plasma ALD studies using TMG and NH_3 as the reactants have reported smaller GaN growth rates of ~0.22 Å / cycle[60] and ~0.51 Å / cycle.[59]

Control experiments were performed to understand the growth mechanism. The first control experiment replaced the electron gun exposures at 50 eV after the TMG/H and NH_3 exposures with an equivalent length purge for 300 cycles. All other conditions remained the same as described for the growth of the GaN film shown in Figure 2.3. Subsequently, *ex situ* spectroscopic ellipsometry and XPS measurements observed no film growth.

Experiments were also performed by removing the precursor doses while maintaining all other reaction conditions for 300 cycles. No film growth was observed by *ex situ* spectroscopic ellipsometry measurements without the TMG doses. Likewise, the reactions performed without NH_3 doses showed no film growth. Control experiments were also performed without HABS exposures. All other reaction conditions were maintained and a 100 s purge replaced the HABS exposure. *Ex situ* spectroscopic ellipsometry measurements observed film growth with a growth rate consistent with the growth rates obtained using the HABS exposures. However, *ex situ* XPS analysis revealed a carbon contamination of 27 at.% for GaN films grown at 27 °C.

Spectroscopic ellipsometry was used to characterize the optical properties of the GaN films. Figure 2.5 shows the index of refraction, n, and the extinction coefficient, k, of the GaN films grown on the Si(111) wafers. The extinction coefficients indicate that the GaN films begin to absorb radiation at energies slightly greater than 3 eV. This absorption threshold is consistent with the bandgap for bulk GaN of 3.4 eV.[3,12] In addition, the index of refraction of the GaN

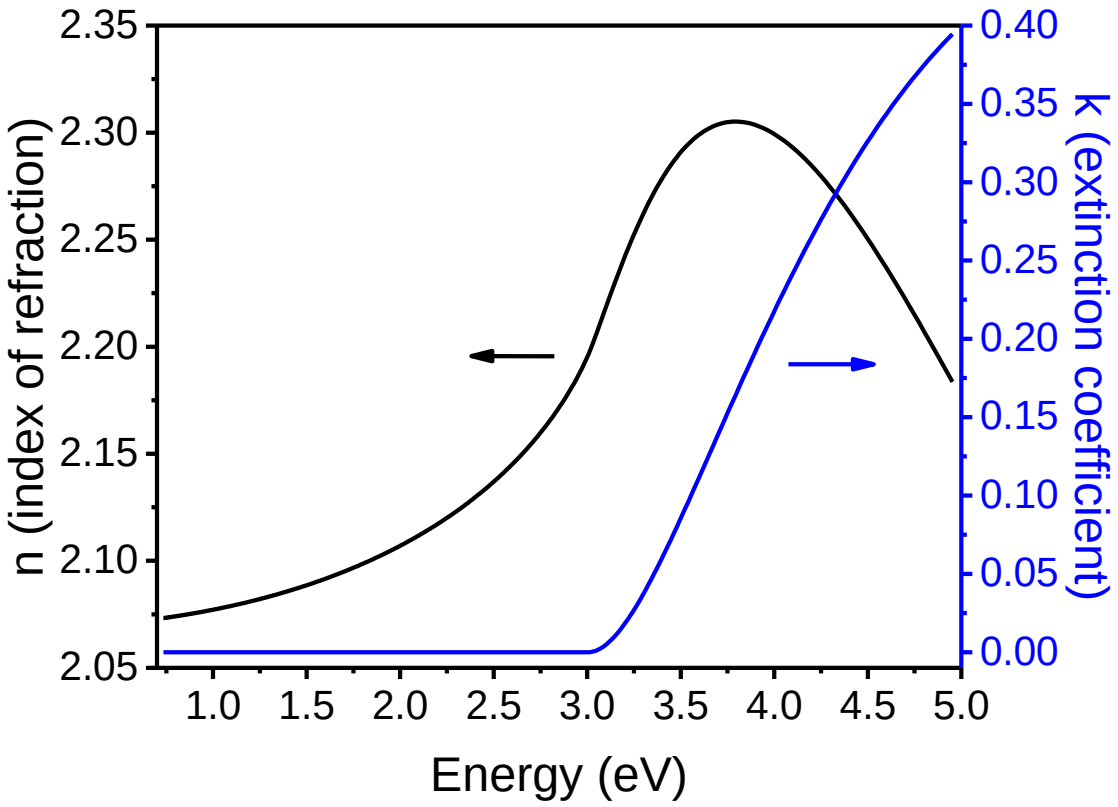

Figure 2.5: Index of refraction, n, and extinction coefficient, k, versus radiation energy for the GaN film on Si(111) wafer.

films is n=2.07 at 1.0 eV and reaches a peak value of approximately n=2.3 at energies above the bandgap energy. These results are slightly smaller than the values of n= 2.33 at 1.0 eV and n=2.67 at 3.38 eV reported in the literature.[89] The smaller refractive indices may result from the high carbon concentration in the polycrystalline GaN films.

B. Crystallinity from GIXRD Measurements

The crystallinity of the GaN films was established using grazing incidence x-ray diffraction (GIXRD) and transmission electron microscopy (TEM). GIXRD results for the GaN films grown on Si(111) wafers are shown in Figure 2.6. Figure 2.6a shows the results for a GaN film grown at 27 °C using 807 reaction cycles. This film had a thickness of ~1200 Å at position 1 as defined in Figure 2.4. Figure 6b displays the results for a GaN film grown at 100 °C using 827 reaction cycles. This film had a thickness of ~600 Å at position 1 as defined in Figure 2.4. For comparison, the XRD results for a crystalline wurtzite GaN powder are shown in Figure 2.6c.[90,91] The Miller indices are associated with each peak and the length of the lines indicates the relative intensities.

A comparison between Figures 6b and 6c indicates that the strong 100, 002 and 101 diffraction peaks of crystalline wurtzite GaN are clearly observed in the GaN film grown at 100 °C. All of the other lower intensity peaks for crystalline wurtzite GaN are also present in the GaN film grown at 100 °C. The major difference is that the peaks in Figure 2.6b are broadened relative to the peaks for crystalline GaN powder.[92] This broadening is consistent with a fine-grained, polycrystalline GaN film grown at 100 °C. The size of the GaN crystallites in the GaN film grown at 100 °C was estimated from the width of the diffraction peaks using the Scherrer equation. This estimate yields GaN crystallites with a diameter of 5-7 nm.

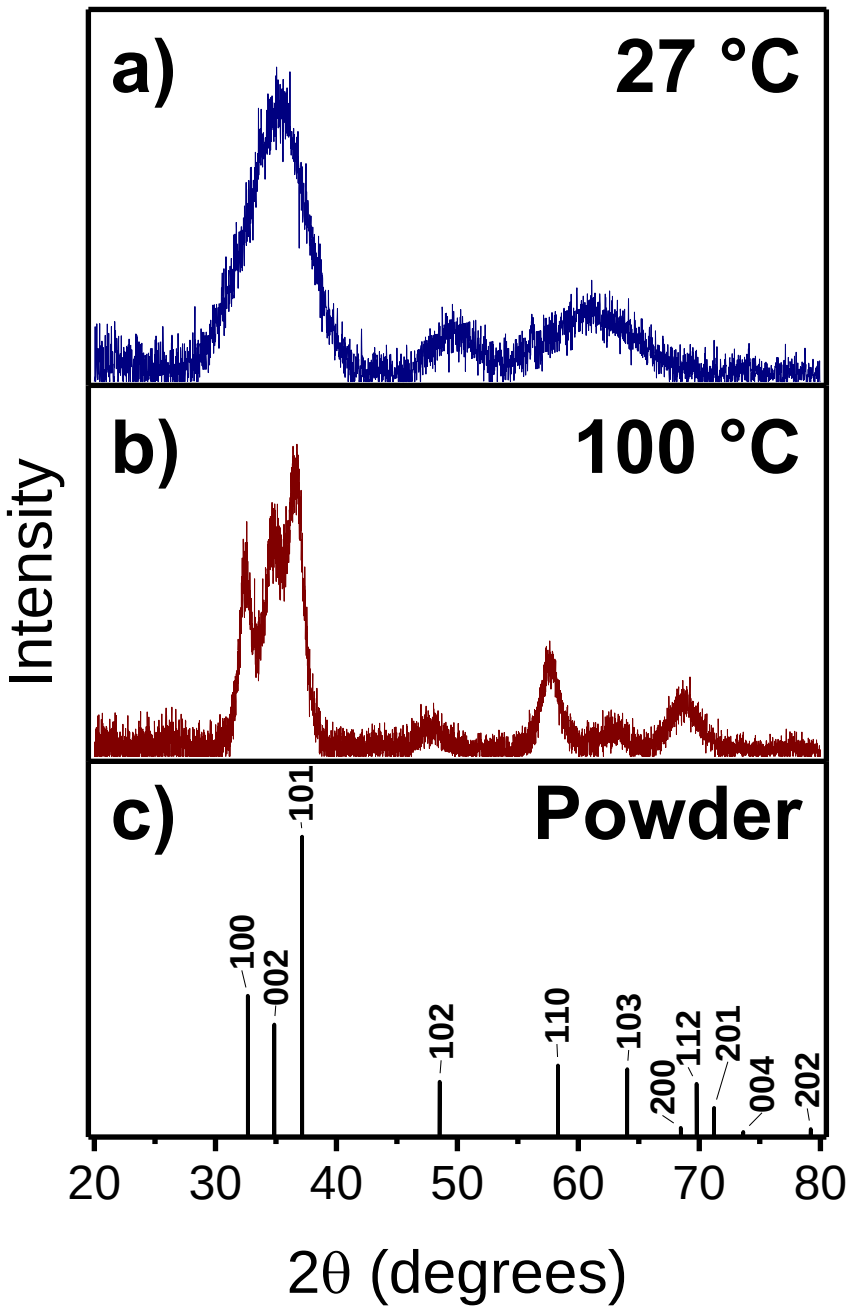

Figure 2.6: GIXRD of GaN films grown on Si(111) wafers at (a) 27 °C and (b) 100 °C. (c) Positions and intensities of diffraction peaks for crystalline wurtzite GaN powder.

The diffraction peaks in Figure 2.6a for the GaN films grown at 27 °C are broader than the diffraction peaks for the GaN films grown at 100 °C in Figure 2.6b. The broadening leads to a coalescence of the strong 100, 002 and 101 diffraction peaks of crystalline wurtzite GaN into one broad peak. The lower intensity peaks are also broader and are slightly shifted relative to the diffraction peaks of crystalline wurtzite GaN powder. This increased broadening suggests that the polycrystalline grain size is smaller for the GaN films grown at 27 °C. The diameter of the GaN crystallites in the GaN film grown at 27 °C was estimated to be 2-5 nm based on the width of the diffraction peaks using the Scherrer equation.

For comparison, GaN films were also grown on the Ga-face of single-crystal GaN(0001) wafers at 27 °C and 100 °C to determine if the GaN films would grow epitaxially on a crystalline GaN substrate. Figure 2.7 shows a picture of a GaN film grown on a single-crystal GaN(0001) wafer on a Si(111) wafer after 500 reaction cycles at 27 °C following the same procedure as employed for the GaN film shown in Figure 2.3. A GaN film is again observed on the Si(111) wafer in agreement with Figure 2.3. A GaN film is not visible on the single-crystal GaN(0001) wafer because the optical characteristics of the deposited GaN film are nearly identical to the underlying single-crystal GaN(0001) wafer.

The GaN films grown on the Ga-face of single-crystal GaN(0001) wafers were also analyzed using *ex situ* GIXRD measurements performed at the Naval Research Laboratory. The GIXRD measurements showed broad diffraction peaks centered at ~36 ° and ~62 °. In addition, sharp diffraction peaks were also observed as expected from the underlying single-crystal GaN substrate. These results were consistent with a polycrystalline GaN film on the GaN(0001) single-crystal substrate with no evidence for homoepitaxial growth. The results at 27 °C and 100 °C were similar although the diffraction peaks were broader for the GaN films grown at 27 °C.

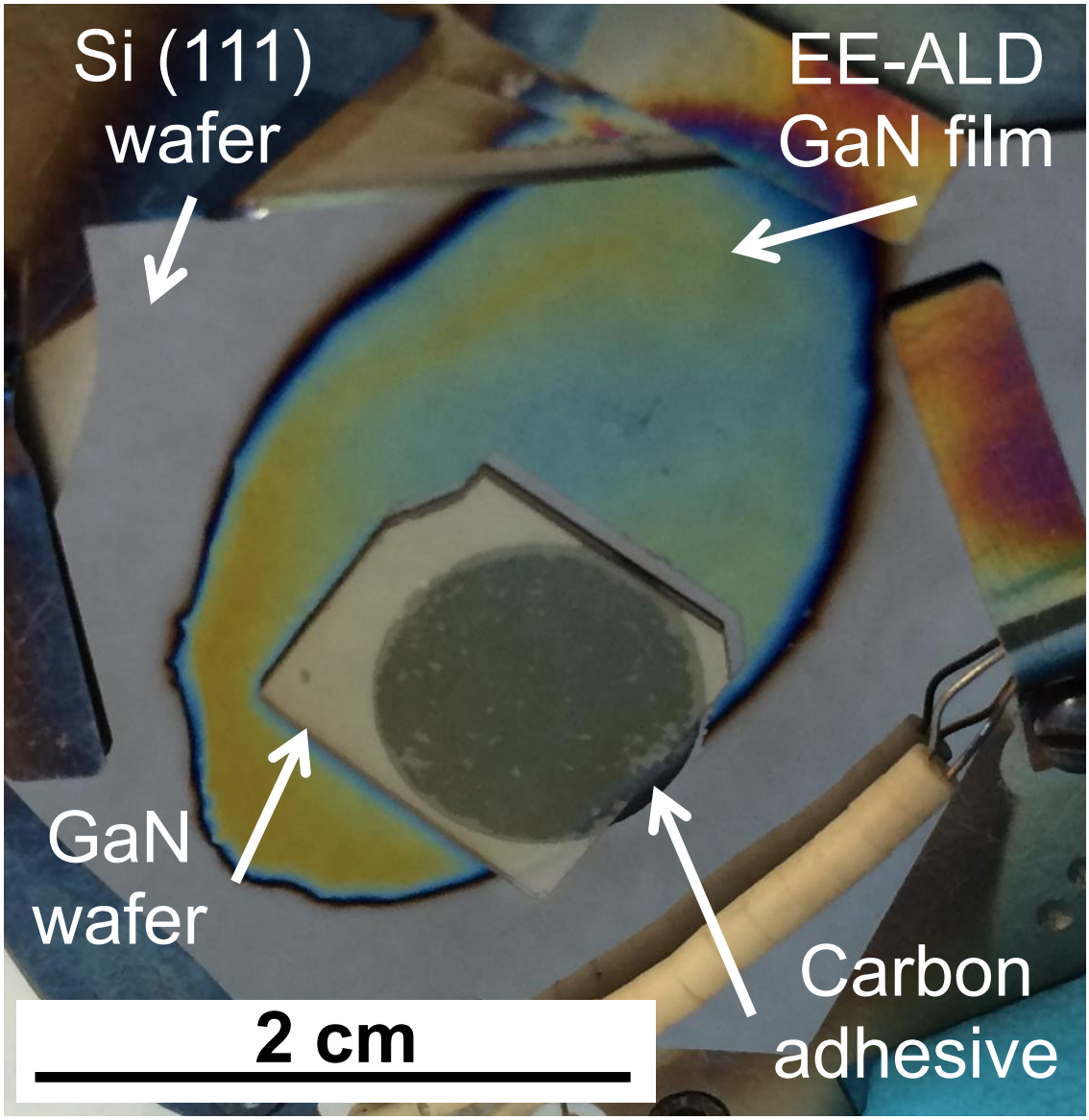

Figure 2.7: Photo of GaN film grown at 27 °C on a single-crystal GaN(0001) substrate attached to a Si(111) wafer using a carbon adhesive.

C. Crystallinity from TEM Measurements

The crystallinity of the deposited GaN films was also verified by TEM imaging. Figure 2.8a shows a cross-sectional TEM image of a GaN film grown at 27 ºC on a Si(111) wafer using 600 reaction cycles. The crystallites in the GaN films are randomly oriented with no preferred direction. The diameters of the GaN crystallites grown at 27 °C vary from 2 to 5 nm. Crystallinity is also observed in Figure 2.8b for the GaN films grown at 100 ºC on a Si(111) wafer using 600 reaction cycles. The crystallites in the GaN films are again randomly oriented with no preferred direction. However, the diameters of the GaN crystallites grown at 100 °C are larger and vary from 5-10 nm. For the GaN films grown at both 27 °C and 100 °C, the crystallite sizes and absence of texturing are in excellent agreement with the XRD measurements.

Figure 2.9 shows high resolution TEM (HRTEM) contrast imaging of a cross-section of a GaN film on the Si(111) wafer. This GaN film was grown at 100 °C using 630 reaction cycles. The TEM image clearly reveals the presence of crystalline GaN grains with random orientations. The GaN crystallites show no epitaxial growth preference on the Si(111) wafer. The lack of epitaxy may result from the thin amorphous layer with a thickness of ~1 nm at the interface between the Si(111) wafer and the GaN film. This amorphous layer may be attributed to carbon contamination on the initial Si(111) wafer. In agreement with the results in Figure 2.8b, the GaN crystallites have diameters ranging from 5-10 nm.

D. Composition from XPS Depth-Profiling Measurements

The cross-sectional composition of the GaN films grown on Si(111) wafers was determined using XPS depth-profiling measurements. Initial XPS depth-profiling measurements revealed that the GaN films oxidized upon exposure to atmosphere. To evaluate the stoichiometry of the GaN films without atmospheric oxidation, an Al capping layer was deposited on the GaN films as a sacrificial oxidant. This Al capping was deposited using

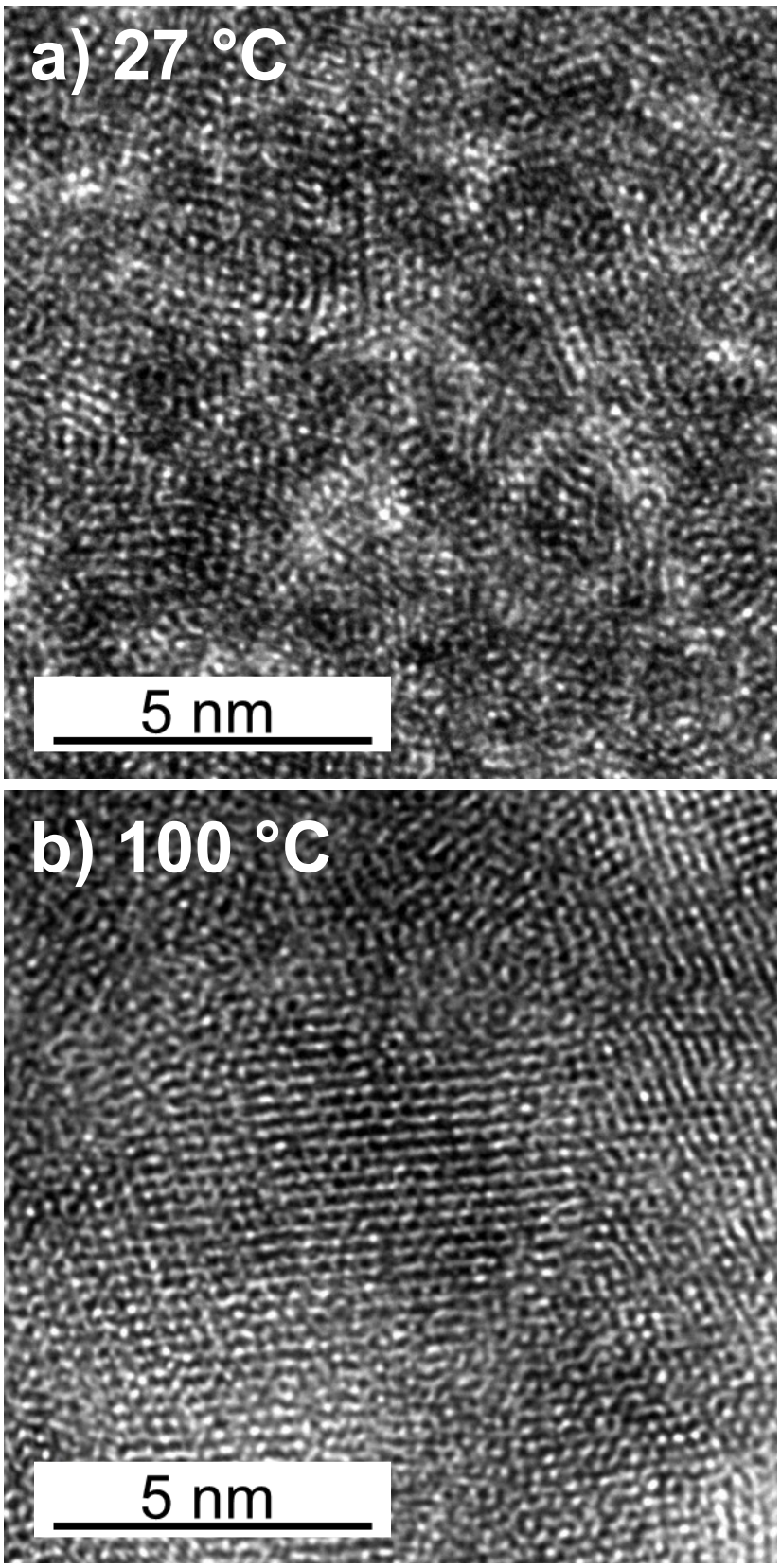

Figure 2.8: Cross-sectional HRTEM phase contrast images of GaN films grown on Si(111) wafer at (a) 27 °C and (b) 100 °C.

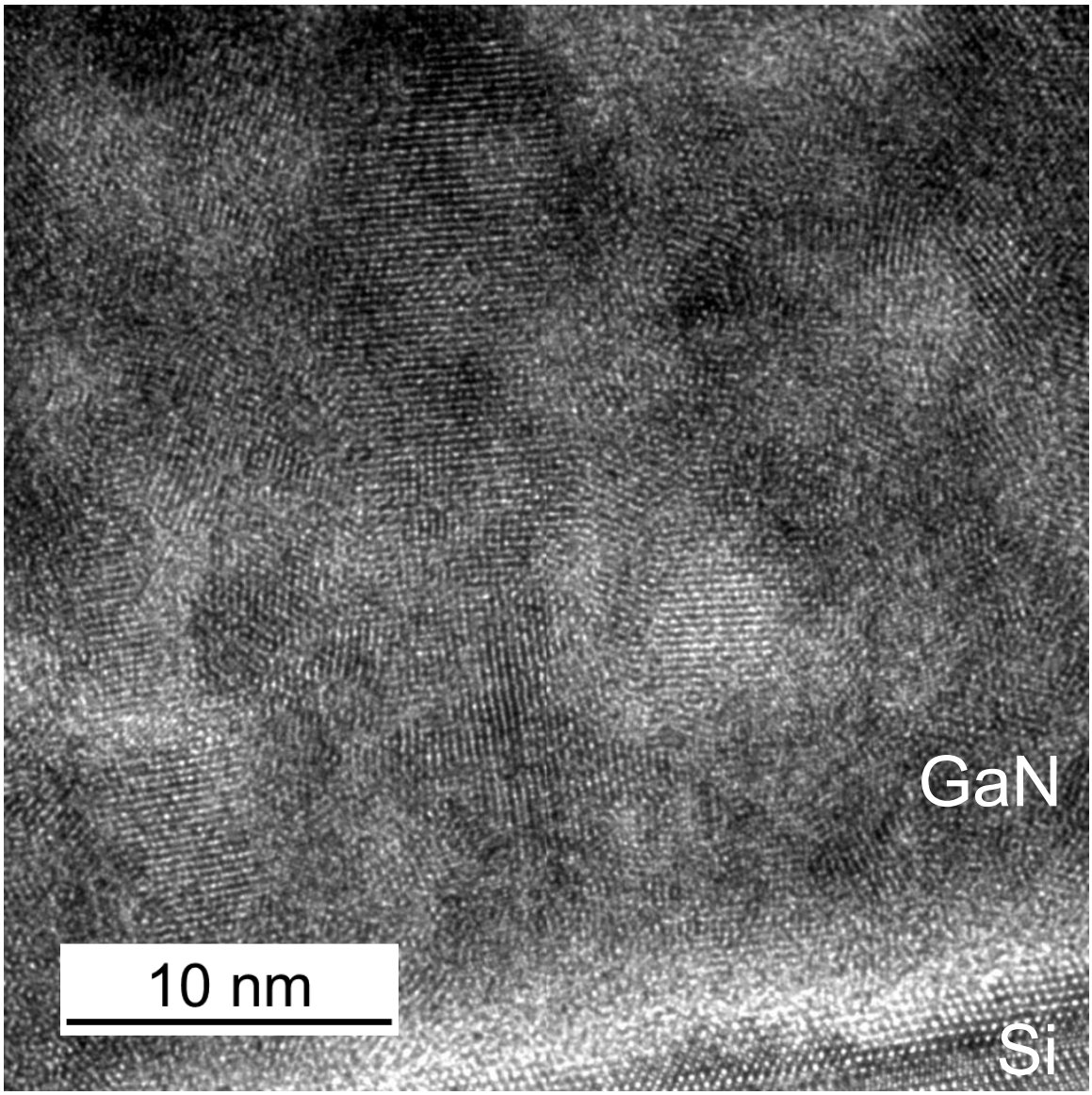

Figure 2.9: Cross-sectional HRTEM phase contrast image of the GaN film grown on Si(111) wafer at 100 °C.

sequential exposures to trimethylaluminum (TMA) and hydrogen radicals from the HABS.

For the XPS depth-profiling results shown in Figure 2.10, the Al capping layer was deposited using 575 reaction cycles of TMA and hydrogen radicals at 100 °C. Figure 2.10 shows that the Al capping layer is oxidized at the surface. This oxidation is attributed to atmospheric exposure. The oxygen profile is consistent with oxygen diffusion into the Al film. The Al capping layer also contains ~20 at.% of nitrogen. This nitrogen is believed to result from the high background pressures of residual NH_3 remaining in the vacuum chamber from the previous GaN growth during the deposition of the Al capping layer. Al metal films are expected to be reactive with residual NH_3.

Figure 2.10 also shows the XPS depth-profiling results for the GaN film under the Al capping layer that was grown at 28 °C using 600 reaction cycles. The Al-capped GaN film displays a region of stoichiometric GaN with oxygen levels below the XPS detection limit under the Al cap. However, the GaN film also shows a significant carbon contamination of ~ 20 at.%. Carbon contamination was present in all the GaN films examined with XPS depth profiling grown at both 27 °C and 100 °C. The carbon concentrations were in the range of 12-35 at.% (average: 23 at.%) for the films grown at 27 °C and 10-20 at.% (average: 13 at.%) for the films grown at 100 °C. The carbon concentrations could not be lowered by longer hydrogen radical exposures or higher hydrogen radical fluxes using the HABS.

Carbon contamination is known to be present in GaN grown using either TMG or TEG and the level of carbon contamination increases at lower growth temperatures.[93] To understand this contamination, many experiments were performed to determine the origin of the carbon in the GaN films. At the end of these GaN film growth studies, an *in situ* Auger spectrometer was added to the vacuum chamber. This Auger spectrometer characterized the carbon on the surface

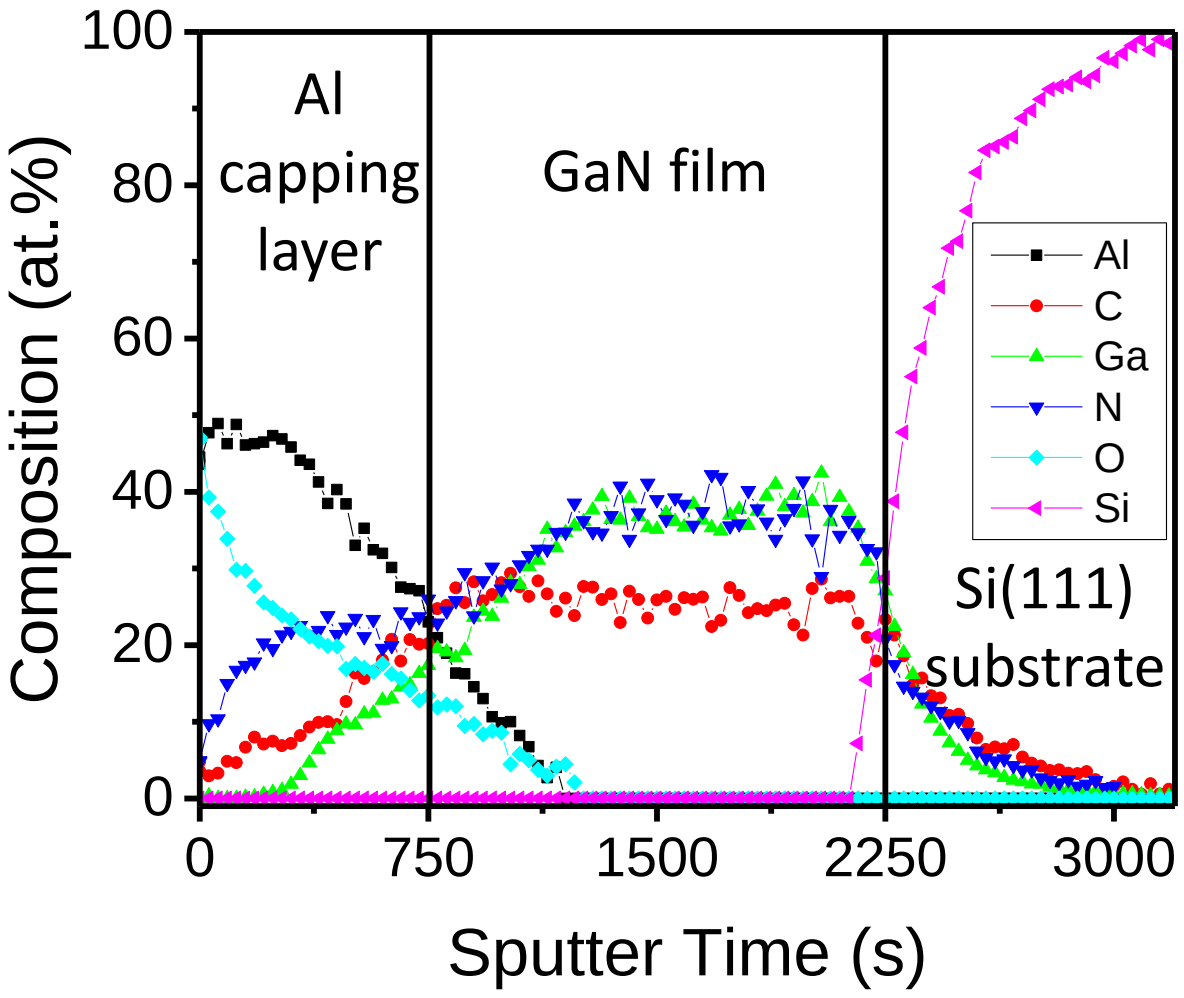

Figure 2.10: XPS depth profile of GaN film grown on Si(111) wafer showing oxygen-free stoichiometric GaN with some carbon contamination. An Al capping layer protected the GaN film from oxidation.

after each step in the reaction cycle. These Auger experiments revealed that the HABS was not removing the carbon after the TMG exposures. In fact, the carbon levels were higher after the HABS exposures. Experiments also revealed that the HABS could not remove the initial carbon on the Si(111) substrate. Carbon concentrations were again larger after the HABS exposures.

The carbon in the GaN films may result from the pyrolysis of residual TMG in the chamber on the hot surfaces of the HABS. TMG pyrolysis in flow tubes[94] and on hot surfaces[95] is known to produce methyl radicals. The decomposition of TMG on GaN(0001) during temperature programed desorption also yields methyl radicals.[96] Over the course of many GaN growth experiments, TMG pyrolysis may produce a HABS source contaminated with carbon. Subsequent inspection of the HABS revealed bluish-back discolorations on the HABS surfaces that were consistent with a carbon film buildup over the course of many GaN growth experiments. In addition, residual TMG pressures in the chamber during the HABS step of the reaction sequence may also directly produce methyl radicals.[95]

In spite of the carbon contamination, the GaN films still display crystallinity as shown in Figures 2.6, 2.8, and 2.9. Consequently, the carbon is believed to be present at the grain boundaries between the GaN crystallites. Earlier studies have correlated "yellow" luminescence with carbon in GaN.[97] Other investigations have observed that the "yellow" luminescence emanates from grain boundaries in GaN.[98] The carbon could also be substituted for nitrogen or gallium in the GaN crystal or exist in interstitial sites.[99] However, carbon at the grain boundaries is the more likely possibility. At carbon concentrations as high as 10-20 at.%, the carbon would alter the GaN crystallinity and preclude the agreement between the x-ray diffraction peaks from the GaN film grown at 100 °C and the crystalline wurtzite GaN powder that was observed in Figure 2.6.

E. Mass Spectrometry Measurements of H_2 Desorption and Etch Products

Quadrupole mass spectrometry measurements were performed during the sequential reaction cycles that define GaN film growth on Si(111) wafers. These experiments determined if the electron exposures could desorb enough H_2 and other possible species to be detected by the mass spectrometer. In particular, the mass spectrometer signals from the desorbed H_2 could be used to quantify the ESD and its dependence on electron energy. The presence of other desorbed species generated by the electron exposure may also determine if the electron beam could desorb Ga or N etch species from the growing GaN surface.

The mass spectrometer monitored a variety of species in the gas phase during the electron exposures. These species can be assigned to hydrogen (m/z=2), methyl species (m/z=15, 14), ammonia species (m/z=17, 16), water (m/z=18, 17), gallium isotopes (m/z= 71, 69) and gallium hydrides (m/z=72, 70). Figure 2.11 shows the ion currents for a variety of species during the electron beam exposure following the HABS exposure. The ion currents are ordered relative to the magnitudes of their ion currents.

The electron current from the electron gun starts to increase at ~75 s. The electron current reaches its maximum current at ~100 s. The electron current incident on the sample remains at its maximum current of ~75 μA for 120 s. The ion currents at m/z=2 (H_2^+) in Figure 2.11b and m/z=69 ($^{69}Ga^+$) and m/z=70 ($^{69}GaH^+$) in Figure 2.11d increase in conjunction with the electron current. In contrast, the ion currents at m/z= 18 (H_2O^+) in Figure 2.11d and m/z=16 and 17 (NH_2^+ and NH_3^+) in Figure 2.11a are relatively constant during the increase in electron current. The ion current at m/z=15 (CH_3^+) in Figure 2.11c shows only a very small increase with the electron current.

The ion current at m/z=2 (H_2^+) increases with the electron current and indicates that H_2 is desorbed to produce dangling bond sites. Other species containing gallium such as gallium

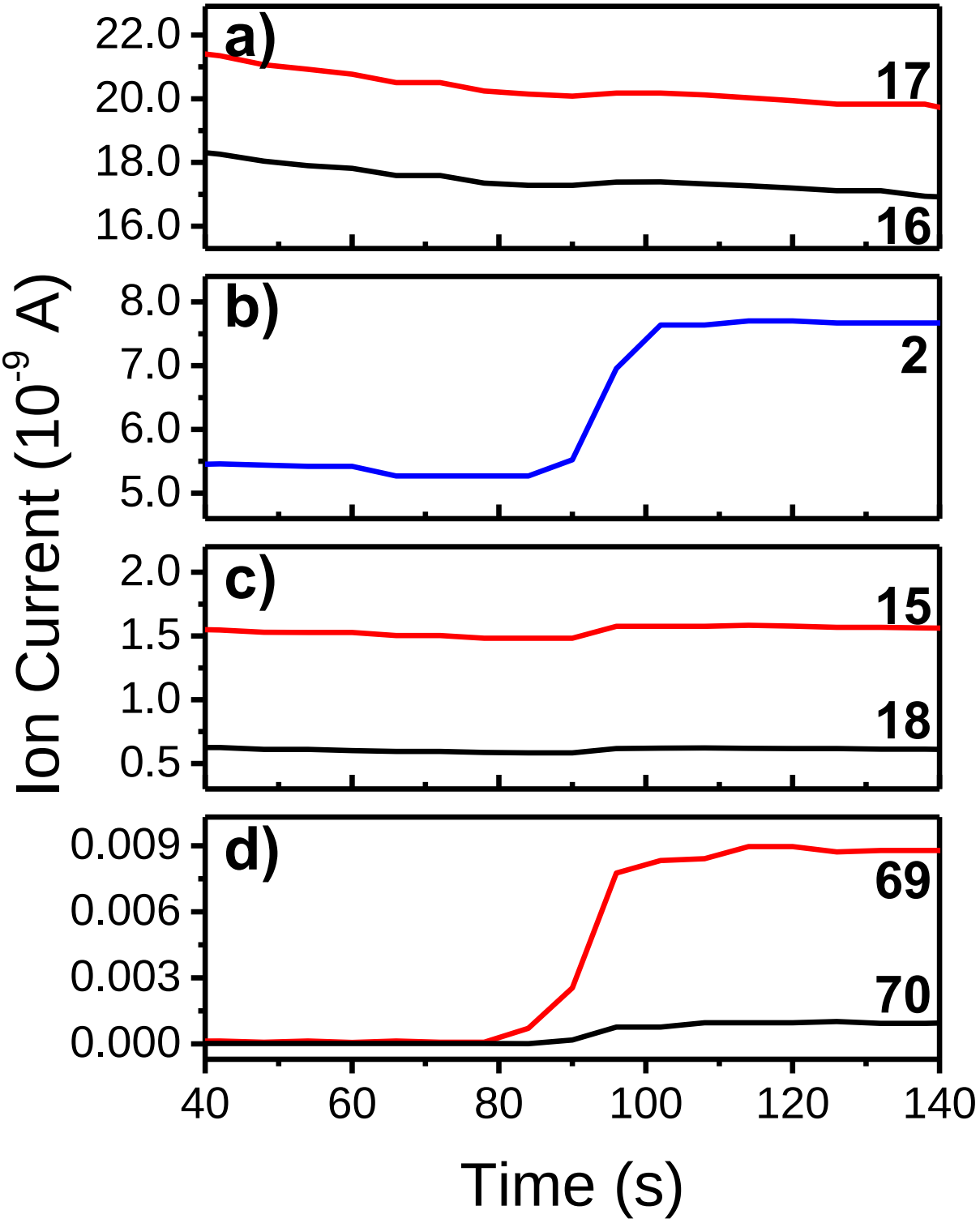

Figure 2.11: Ion currents for: (a) m/z= 16 and 17; (b) m/z=2; (c) m/z=15 and 18; and (d) m/z=69 and 70 during the GaN growth on Si(111) wafers after the end of the HABS exposure. The electron current is turned on at ~75 s and reaches its maximum value at ~100 s.

hydrides at m/z = 69, 70, 71, and 72 also increase with the electron current. The m/z=69 species is assigned to $^{69}Ga^+$. The m/z = 70 species is attributed to $^{69}GaH^+$. The m/z = 71 species is assigned to either $^{71}Ga^+$ or $^{69}GaH_2^+$. The m/z = 72 species is attributed to either $^{69}GaH_3^+$ or $^{71}GaH^+$, respectively. These ion currents are consistent with the existence of gallium hydrides and the etching of the GaN film. These etching products suggest that the observed GaN growth may result from competing deposition and etching processes. GaN etching with low energy electrons has previously been observed for GaN samples in contact with hydrogen radicals from a H_2 plasma.[100]

The pressure changes resulting from the electron exposure were quantified by measuring the ion currents before and during the electron exposures. The H_2 pressure changes during the electron exposures after the TMG/H and NH_3 reactions were nearly identical. The ion current changes at m/z =2 (H_2^+) versus electron energy are shown in Figure 2.12a. At each energy, the ion current change increased with electron current from the electron gun and stayed elevated during the 120 s electron exposure. The H_2 pressure prior to the electron exposures was ~2.7 x 10^{-9} Torr using the calibration of the ion current to H_2 pressure of ~2 A/Torr. Figure 2.12a shows that the desorbed H_2 has an electron energy threshold at ~25 eV. Pronounced H_2 desorption signals are observed at the electron energy of 50 eV used for GaN film growth. Larger H_2 desorption signals that increase progressively with electron energy are measured at higher electron energies.

The ion current changes for m/z=69 after the TMG/H and NH_3 exposures were also nearly identical and are shown versus electron beam energy in Figure 2.12b. The gallium hydride species all exhibited a similar dependence on the electron beam energy. The ion current for the gallium hydride species increased with electron current and stayed elevated during the

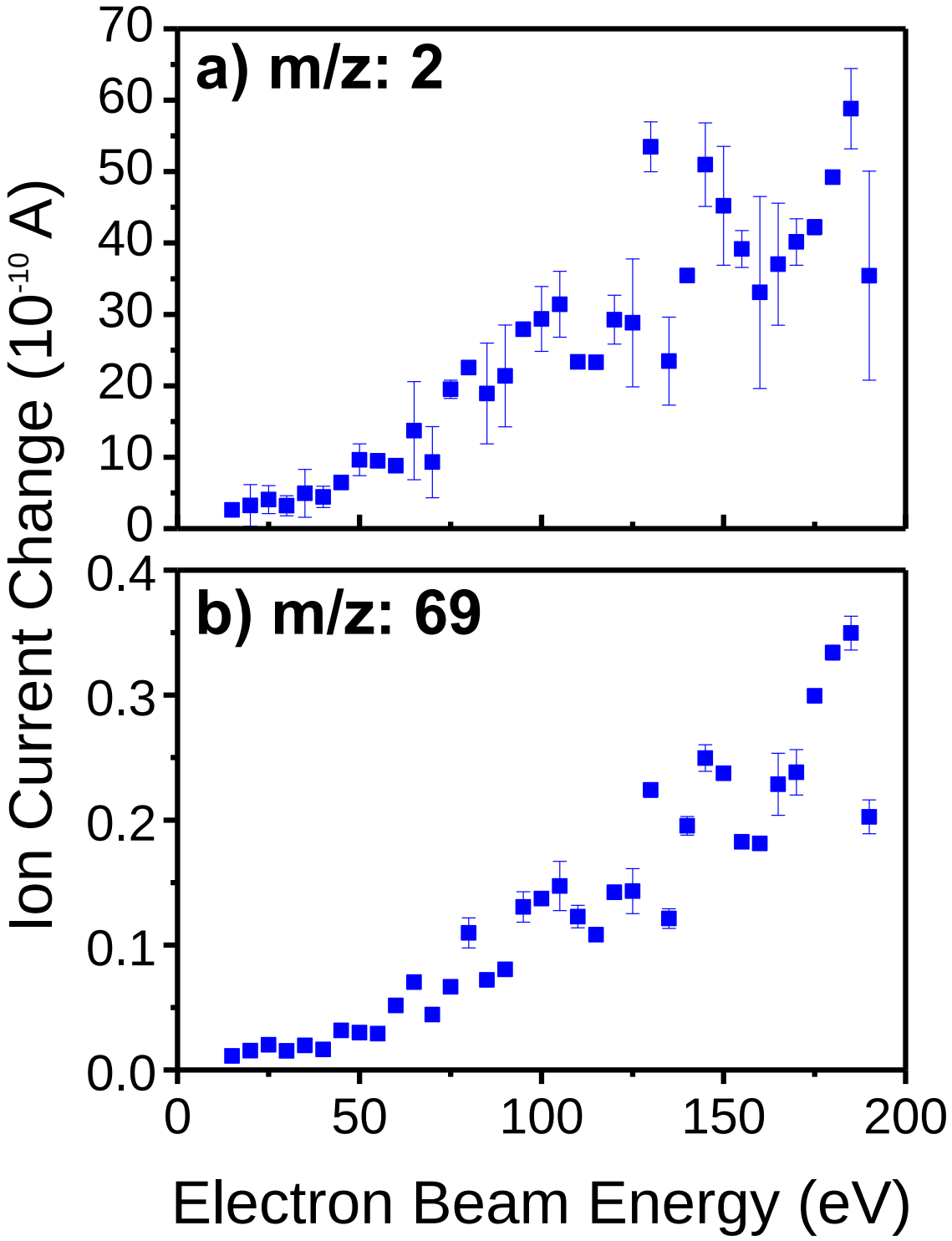

Figure 2.12: Ion currents for (a) m/z=2 and (b) m/z=69 versus electron beam energy during the electron exposures during GaN growth on Si(111) wafers. The ion currents were nearly identical after the TMG/H and NH_3 reactions.

120 s electron exposure at each electron energy. Figure 2.12b shows that the desorbed m/z=69 species begins to increase progressively at electron energies > 50 eV. Small m/z=69 ion current changes are observed at the electron energy of 50 eV used for GaN film growth.

A comparison between Figures 12a and 12b can be used to speculate on the optimum electron energy to grow the GaN film. Optimum growth may be related to the ratio between the H_2 ion current change and the gallium hydride ion current change. Higher ratios may predict higher GaN film growth relative to GaN etching. Based on this criteria, electron energies of 50 eV may represent a compromise between reasonable H_2 desorption with minimal desorption of gallium hydride etching products. Additional growth experiments at other electron energies are needed to test this hypothesis.

Other ESD systems also observe an energy threshold and an increase in the desorption yield versus electron energy. For example, a pronounced energy threshold at ~24 eV was observed for H desorption from Si(100)-(1x1).[66,68,101] Energy thresholds are also observed for the ESD of neutral alkalis for alkali halide substrates.[102] The thresholds correspond to electron excitation of substrate core levels.[102] The energy threshold for Cl^+ ESD from Cl on Si(100) also corresponds to the Cl 3s core level.[103] The ESD of alkali halide layers from W(110) also shows energy thresholds that are consistent with alkali and halide core levels.[104]

F. Constant Ion Currents during Electron Exposures

Figure 2.11 shows that the ion currents for m/z=2 (H_2^+) and m/z=69 ($^{69}Ga^+$) remain constant during the electron beam exposure at 50 eV. The steady ion currents provide no evidence of depletion of the hydrogen coverage over the 120 s electron beam exposure. These constant ion currents suggest that the electron exposure only removes a small fraction of the hydrogen from a large reservoir of hydrogen on the surface. This explanation can be tested by

estimating the amount of hydrogen desorbed based on the electron flux and the hydrogen ESD cross section from GaN.[63]

The normalized hydrogen coverage, Θ/Θ_0, will be reduced by hydrogen ESD according to $\Theta/\Theta_0 = \exp[-\sigma D]$.[66,68] σ is the hydrogen ESD cross section in cm^2 and D is the electron dose in electrons/cm^2. The hydrogen ESD cross section is $\sigma = 2 \times 10^{-17}$ cm^2 at 90 eV.[63] This hydrogen ESD cross section at 90 eV will be used as an estimate for the hydrogen ESD cross section at 50 eV. The electron current of 75 μA over a surface area of 5 cm^2 yields an electron flux of $\Phi = 9.4 \times 10^{13}$ electrons/(cm^2 s). This flux for a duration of 1 second yields an electron dose of D= 9.4×10^{13} electrons/cm^2. The normalized hydrogen coverage after a 1 s electron beam exposure is then determined as $\Theta/\Theta_0 = \exp[-\sigma D] = 0.998$. Approximately 0.2% of the initial hydrogen coverage is desorbed in 1 second. After a 120 s electron beam exposure, the normalized hydrogen coverage remains fairly high and is calculated to be $\Theta/\Theta_0 = 0.80$.

The small predicted changes in the hydrogen coverage may be even smaller if the hydrogen ESD cross section is lower at 50 eV than the hydrogen ESD cross section at 90 eV. A smaller hydrogen ESD cross section at 50 eV would be expected given the results shown in Figure 2.12a. The small predicted reduction in hydrogen coverage is consistent with the constant m/z=2 (H_2^+) ion current versus electron beam exposure observed in Figure 2.11. If there is little change in the hydrogen coverage, then the hydrogen ESD effectively occurs from a constant hydrogen source. The increase in GaN growth rate with increasing electron exposure time is also consistent with the small reduction in hydrogen coverage resulting from hydrogen ESD.

The H_2 pressure change during the electron beam exposure can also be used to estimate the H_2 desorption yield from the surface. Figure 2.11c shows a change in ion current of ~2×10^{-9} A for m/z=2 (H_2^+) during the electron beam exposure. The calibration of the ion current to the

H_2 pressure is ~2 A/Torr. Therefore, the ion current change of ~2 x 10^{-9} A represents a H_2 pressure change of ~1 x 10^{-9} Torr. This H_2 pressure change can be converted to a H_2 throughput, Q, using Q= SP where S is the chamber pumping speed and P is the H_2 pressure change. With a H_2 pumping speed of 125 L/s for the turbomolecular pump (HiPace 300C), the throughput is Q=4.1 x 10^{12} molecules/s.

Given that the increased throughput from H_2 ESD occurs from a surface area of ~5 cm^2, the H_2 flux from the surface area exposed to the electron beam is Q/5 = 8.2 x 10^{11} molecules/(cm^2 s). The initial hydrogen coverage is assumed to be ~8.5 x 10^{14} H atoms/cm^2 based on hydrogen in the (2x2)H structure with three of every four Ga surface atoms bonded to H.[84] Therefore, the H_2 flux of 8.2 x 10^{11} molecules/(cm^2 s) represents the desorption of 1.6 x 10^{12} atoms/(cm^2 s) or only ~0.2% of the initial hydrogen coverage in 1 second. These estimates of hydrogen ESD flux from the H_2 pressure increase during the electron beam exposure in 1 second are in good agreement with the predicted loss of hydrogen coverage in 1 second based on the hydrogen ESD cross sections.

The surface hydrogen coverage could also be repopulated by a reservoir of hydrogen in the underlying GaN film. Hydrogenation of GaN can result from GaN processing steps such as H_2 plasma exposures.[105,106] For the GaN growth in this study, the hydrogenation of GaN could take place during the HABS exposure. If the bulk hydrogen diffusion is fast enough, then this hydrogen from the HABS exposure may repopulate the surface hydrogen coverage and help maintain the constant H_2 and gallium hydride desorption during the electron exposure. The hydrogen lost during ESD could also be replenished by the surface diffusion of hydrogen from the surface area surrounding the area exposed to the electron gun. Similar refilling of depleted

areas by surface diffusion was the basis of previous laser induced thermal desorption measurements of surface diffusion.[107,108]

Another possibility is that the NH_3 background pressure may react with the dangling bonds created by hydrogen ESD during the electron exposures. The ion currents shown in Figure 2.11a reveal that a large NH_3 background pressure is present during GaN growth. NH_3 adsorption from this NH_3 background pressure would add additional hydrogen to the surface that could be desorbed again through hydrogen ESD. This process would deliver a continuous supply of hydrogen to the surface and also allow nitrogen to be added to the growing GaN film. The actual NH_3 dose would then serve only to replenish the NH_3 background pressure. However, the ion currents for m/z=16 and 17 (NH_3^+ and NH_2^+) in Figure 2.11a do not show any evidence of a decrease coinciding with the electron exposure. The loss of NH_3 required to refill the dangling bond sites created by hydrogen ESD may be negligible. The slight reduction of the NH_3 background pressure over time in Figure 2.11a is attributed to slow NH_3 pumping.

If the loss of hydrogen coverage from hydrogen ESD is small or if hydrogen refills the dangling bonds from hydrogen reservoirs or NH_3 adsorption, then the TMG and NH_3 exposures during the sequential reactions would encounter a GaN surface that is largely passivated by hydrogen. TMG may adsorb on the GaN surface through Lewis acid-Lewis base interactions. TMG is a strong Lewis acid.[109] The nitrogen atoms on the GaN surface have lone pairs that can serve as Lewis bases. At the low temperatures of GaN growth, TMG may be able to adsorb to the surface and remain on the surface until the next electron beam exposure. The electrons may then facilitate the reaction between adsorbed TMG and the NH_3 background pressures. NH_3 may adsorb on dangling bonds and deliver nitrogen during the electron exposures because NH_3 has a

high background pressure. NH_3 may also adsorb at Ga surface sites through Lewis acid-Lewis base interactions.

The mass spectrometer results for m/z=2 (H_2^+) in Figure 2.11 provide a useful measure of the hydrogen ESD process. The constant ion current for m/z=2 (H_2^+) during the electron beam exposure suggests that the hydrogen ESD process is not depleting the hydrogen coverage as implied by the stepwise sequence of surface reactions shown in Figure 2.1. GaN growth must be occurring by alternative mechanisms at close to full hydrogen coverage. One possible alternative mechanism is illustrated in Figure 2.13. In this growth mechanism, the adsorption of TMG and NH_3 occurs primarily through Lewis acid-Lewis base interactions. The hydrogen ESD facilitates Ga-N bond formation from species in the initial Lewis acid-Lewis base complex. Additional experiments will be required to unravel the complexity of the electron-enhanced film growth at low temperatures.

G. Electron Enhancement for Other Thin Films and Competing Growth and Etching

This work has demonstrated that electron enhancement via hydrogen ESD can be used to grow crystalline GaN films at room temperature and 100 °C. Hydrogen ESD can occur from other materials such as silicon,[65-69] diamond[36] and TiO_2.[37] Hydrogen ESD could facilitate the low temperature growth of these materials. Other surface species, such as halogens, could also be desorbed to induce low temperature film growth.[38] Consequently, this electron enhanced growth technique could facilitate the low temperature deposition of a wide range of other materials. Future possibilities include the electron enhanced growth of: silicon with Si_2H_6; SiC with Si_2H_6 and $CH_2=CH_2$; and diamond with $CH_2=CH_2$.

The competing etching during ESD revealed by the mass spectrometer measurements is an associated electron-induced process. This competing etching process may also be beneficial. Material that is not part of a crystalline lattice may be more favorably etched by the electron

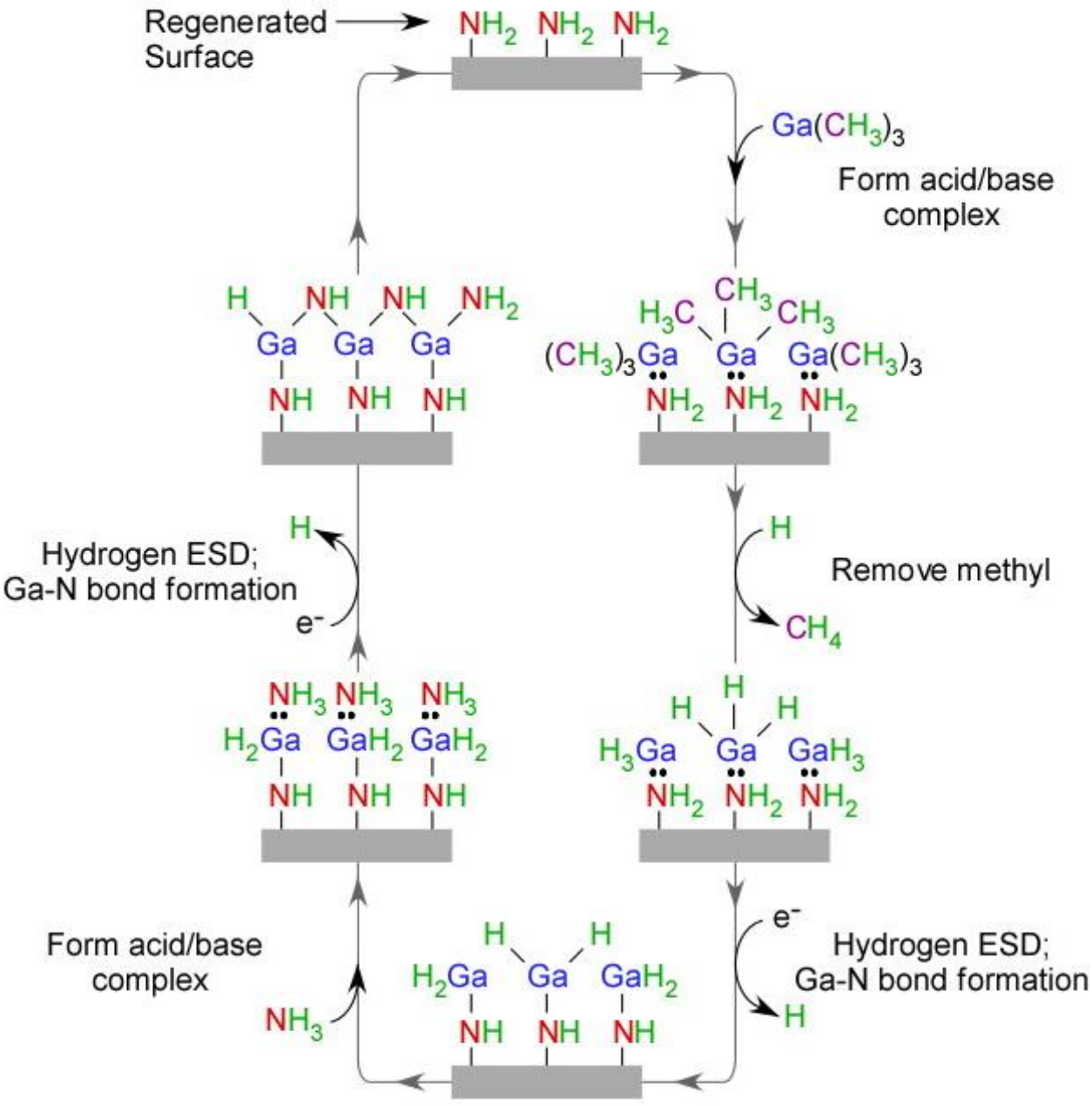

Figure 2.13: Alternative growth mechanism for electron-enhanced GaN growth using sequential surface reactions.

beam. The electrons would then both lead to film growth and also provide a means to remove amorphous material. The competing growth and etching processes may be required to obtain the crystalline GaN films at low temperatures. A similar competing process between growth and etching has been proposed to explain the smoothing of diamond films during diamond CVD.[110,111]

V. Conclusions

The growth of crystalline GaN thin films at low temperatures was demonstrated using low energy electrons at 50 eV. Electrons are able to desorb hydrogen from the GaN surface and produce dangling bonds that facilitate Ga-N bond formation. GaN films were deposited over areas > 5 cm^2 at room temperature and 100 °C on Si(111) wafers. The GaN growth procedure was a cycle of reactions similar to the reaction sequences employed for GaN ALD. TMG, H radicals and NH_3 were employed as the reactants. The electrons were included in the reaction cycle after the TMG/H and NH_3 exposures.

The GaN films grew linearly with the number of reaction cycles. The GaN film thicknesses were correlated with the electron flux and the GaN films were thicker closer to the electron gun. Linear growth rates from 0.9 to 1.3 Å/cycle were measured depending on the electron flux. GIXRD analysis of the GaN films was consistent with polycrystalline films in the wurtzite crystal structure. TEM images also showed crystalline grains with diameters between 2-10 nm depending on temperature. The GaN films that were capped with Al contained no oxygen. However, the carbon concentration in the GaN films was between 10-35 at.%. The carbon concentration may have resulted from TMG pyrolysis on the hot surfaces of the hydrogen atom beam source (HABS) that produces CH_3 radicals.

The pressure of H_2 and various GaN etch products increased during the electron beam exposures during the reaction cycles. The constant ion currents for the H_2 and gallium hydride etch products during the electron beam exposures suggested that the reduction in hydrogen coverage resulting from hydrogen ESD is negligible. Alternatively, hydrogen rapidly refills the dangling bond sites from hydrogen reservoirs. The ion currents corresponding to the H_2 and GaN etch products increased with electron beam energy from 25 to 200 eV. These mass spectrometry results indicate that the electron enhanced GaN growth occurs concurrently with competing GaN etching. The competing etching may be able to remove amorphous GaN and produce crystalline GaN at low temperatures. The ability of ESD to remove hydrogen or other surface species may facilitate the low temperature growth of a wide range of materials.

VI. Acknowledgements

This work was supported by Defense Advanced Research Projects Agency (DARPA) under grant W911NF-13-1-0041. The authors thank Brian Holloway, Tyler McQuade and Anne Fischer from DARPA for their support and helpful comments. The authors also are grateful to John Russell and Chip Eddy from the Naval Research Laboratory for useful discussions and for providing the single-crystal GaN wafer. The authors also thank Andres Jaramillo-Botero and William Goddard from the California Institute of Technology for many useful suggestions. In addition, the authors acknowledge Kenneth Smith and Donald David from the University of Colorado Integrated Instrument Development Facility for their help with system design, development and computer interfacing.

Chapter 3: Electron Enhanced Atomic Layer Deposition of Silicon Thin Films at Room Temperature[112]

Jaclyn K. Sprenger[1], Huaxing Sun[1], Andrew S. Cavanagh[1] & Steven M. George[1,2]

[1]Department of Chemistry and Biochemistry, University of Colorado, Boulder, CO 80309; [2]Department of Mechanical Engineering, University of Colorado, Boulder, CO 80309.

I. Abstract

Silicon thin films were deposited at room temperature with electron-enhanced atomic layer deposition (EE-ALD) using sequential exposures of disilane (Si_2H_6) and electrons. EE-ALD promotes silicon film growth through hydrogen electron stimulated desorption (ESD) that creates reactive dangling bonds and facilitates Si_2H_6 adsorption at low temperatures. Without hydrogen ESD, silicon growth relies on thermal pathways for H_2 desorption and dangling bond formation at much higher temperatures. An electron flood gun was utilized to deposit Si films over areas of ~1 cm^2. The silicon film thickness was monitored *in situ* with a multi-wavelength ellipsometer. A threshold electron energy of ~25 eV was observed for the Si film growth. A maximum growth rate of ~0.3 Å/cycle was measured at electron energies of 100-150 eV. This growth rate is close to the anticipated growth rate assuming dissociative Si_2H_6 adsorption on dangling bonds on representative single-crystal silicon surfaces. The Si growth rate also displayed self-limiting behavior as expected for an ALD process. The silicon growth rate was self-limiting at larger Si_2H_6 pressures for a fixed exposure time and at longer electron exposure times. The silicon growth rate versus electron exposure time yielded a hydrogen ESD cross section of $\sigma = 5.8 \times 10^{-17}$ cm^2. *Ex situ* spectroscopic ellipsometry showed good conformality in thickness across the ~1 cm^2 area of the Si film. Si EE-ALD should be useful for depositing ultrathin silicon films on thermally sensitive substrates, avoiding silicide formation and filling high aspect ratio structures.

II. Introduction

Silicon is one of the most important semiconductor materials and is foundational for microelectronic devices. Silicon is usually deposited by chemical vapor deposition (CVD) at high temperatures ranging from 600-1100 °C with various silane and chlorosilane precursors.[113-117] At the low end of this temperature range, the silicon growth rate is dominated by surface kinetic processes.[113,114] At the high end of this temperature range, the silicon growth rate is determined by reactant mass transport.[113,114]

The surface kinetic processes that limit silicon growth at low temperatures are either H_2 desorption using silane precursors or HCl desorption using chlorosilane precursors.[113-115] The strong Si-H bond energy of ~90 kcal/mol and the recombinatory H_2 kinetics lead to high desorption temperatures.[118-120] The desorption temperatures are ~370-600 °C for H_2 desorption from dihydride and monohydride species.[118,119,121-123] The minimum Si growth temperatures using silanes are correlated with the H_2 desorption required to create dangling bonds that can adsorb additional silane precursors resulting in silicon growth.[115]

Silicon growth could occur at much lower temperatures if hydrogen could be desorbed by non-thermal means. One possible non-thermal hydrogen desorption mechanism is electron stimulated desorption (ESD).[66,124,125] ESD can occur through a number of processes such as the Menzel-Gomer-Redhead and Knotek-Feibelman mechanisms.[31-33,126] ESD has been previously used for surface analysis to image chemical bond directionality and thermal disorder in adsorbed species using electron stimulated desorption ion angular distribution (ESDIAD).[62,127-132] ESD is also a component of electron beam induced deposition (EBID) which uses high energy electrons for the direct writing of nanostructures.[133] However, ESD has not been used for macroscopic thin film growth.

Hydrogen removal by ESD from silicon surfaces has also been achieved using scanning tunneling microscopy (STM) techniques.[77,134,135] STM-ESD desorbs hydrogen and leaves behind dangling bonds on the silicon surface.[77,79,82,134-136] These dangling bonds are very reactive and readily adsorb other precursors. The remaining hydrogen acts as a mask to prevent adsorption and provides a pathway for hydrogen desorption nanolithography.[82] The dangling bonds can be reacted with precursors to form nanoscale features such as oxide,[77,80] Fe,[134] and TiO_2[137] nanoscale lines on Si(100) surfaces. Multiple Si monolayers over nanoscale areas of 100 x 100 nm^2 have also been fabricated on Si(100) using sequential hydrogen ESD and disilane exposures.[138,139]

GaN electron-enhanced growth was recently performed to demonstrate the feasibility of electron-enhanced macroscopic thin film growth.[140] GaN CVD usually requires temperatures of 800-1100 °C using precursors such as $Ga(CH_3)_3$ and NH_3.[25,141,142] For GaN electron-enhanced growth, film growth was performed at much lower temperatures of room temperature and 100°C using sequential reaction cycles with $Ga(CH_3)_3$, H radical, NH_3, and electron exposures.[140] GaN growth rates up to 1.3 Å/cycle were observed for electron energies of 50 eV. In addition, X-ray diffraction and transmission electron microscopy measurements revealed that the GaN films were polycrystalline.[140]

In this paper, sequential exposures of Si_2H_6 and low energy electrons are used to grow silicon films over areas of ~1 cm^2 by electron-enhanced ALD (EE-ALD) at room temperature. The Si EE-ALD films were grown in a stepwise sequence as illustrated in Figure 3.1. The silicon growth rate was measured using *in situ* ellipsometry as a function of electron energy up to 200 eV. Silicon growth was also studied versus Si_2H_6 and electron exposures to determine if the sequential reactions are both self-limiting. In addition, the film composition was evaluated using

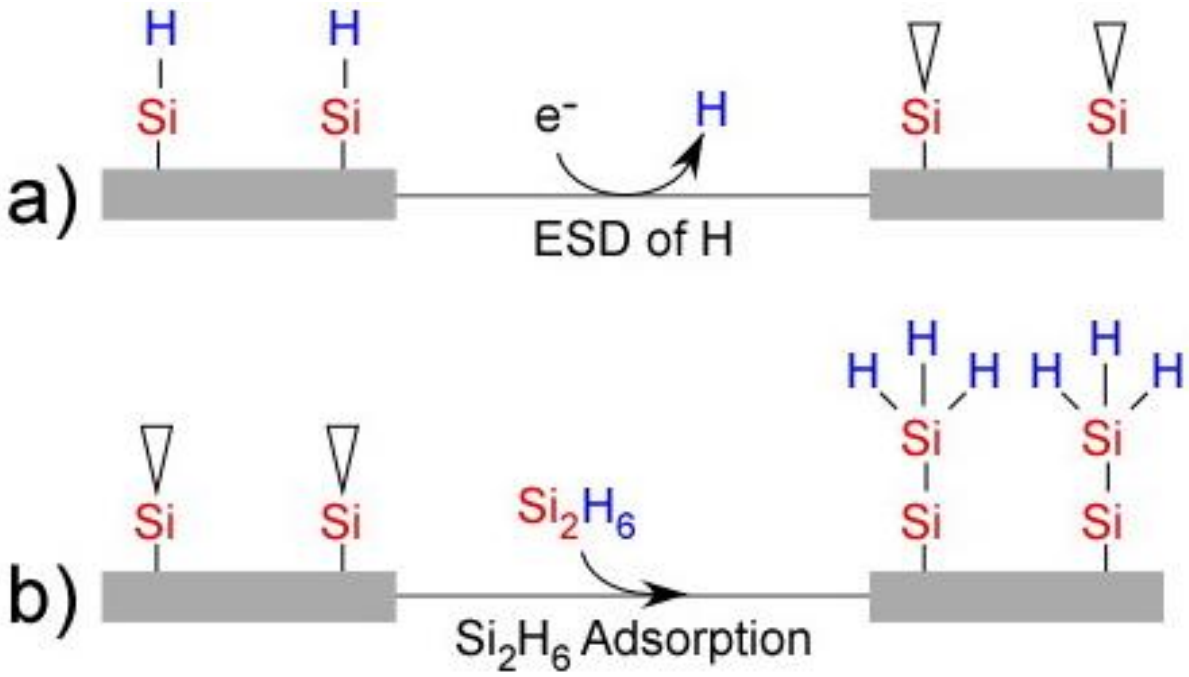

Figure 3.1: Proposed growth mechanism for Si electron-enhanced atomic layer deposition (EE-ALD) using disilane as the reactant.

in situ Auger electron spectroscopy (AES) and *ex situ* X-ray photoelectron spectroscopy (XPS). These studies demonstrate that non-thermal desorption of hydrogen using ESD can be used to deposit silicon films at room temperature.

III. Experimental

A. Vacuum Chamber

The silicon films were grown in a vacuum chamber that is similar to the vacuum chamber that has been described previously.[140] This experimental apparatus contains a sample load lock, a main vacuum chamber pumped with an ion pump and a turbomolecular pump, and a sample analysis chamber containing an Auger electron spectroscopy (AES) spectrometer that is pumped with an ion pump. A schematic of this experimental apparatus is shown in Figure 3.2. The main chamber also contains an electron gun (Model FRA-2x1-2, Kimball Physics Inc.), a mass spectrometer (PrismaPlus QMG 220, Pfeiffer Vacuum) and hot cathode and cold cathode pressure gauges. The sample analysis chamber also includes a hot cathode pressure gauge.

Compared with the previous study of GaN electron-enhanced thin film growth,[140] the electron flood gun in this investigation was oriented normal to the substrate surface. In addition, a different cathode material was used in the electron gun. The cathode was comprised of a tantalum disc secured to a tungsten-rhenium (95%-5%) filament. This filament composition was an improvement over the previous filament made from yttria-coated iridium. The yttria-coated iridium filament would eventually fail after repeated disilane precursor exposures. The observed failure mechanisms included reduction of the yttria layer and silicide formation leading to increased resistance and decreased melting point. The electron flood gun produced electron energies from 5 to 1000 eV at electron currents of 1 nA to 400 μA.

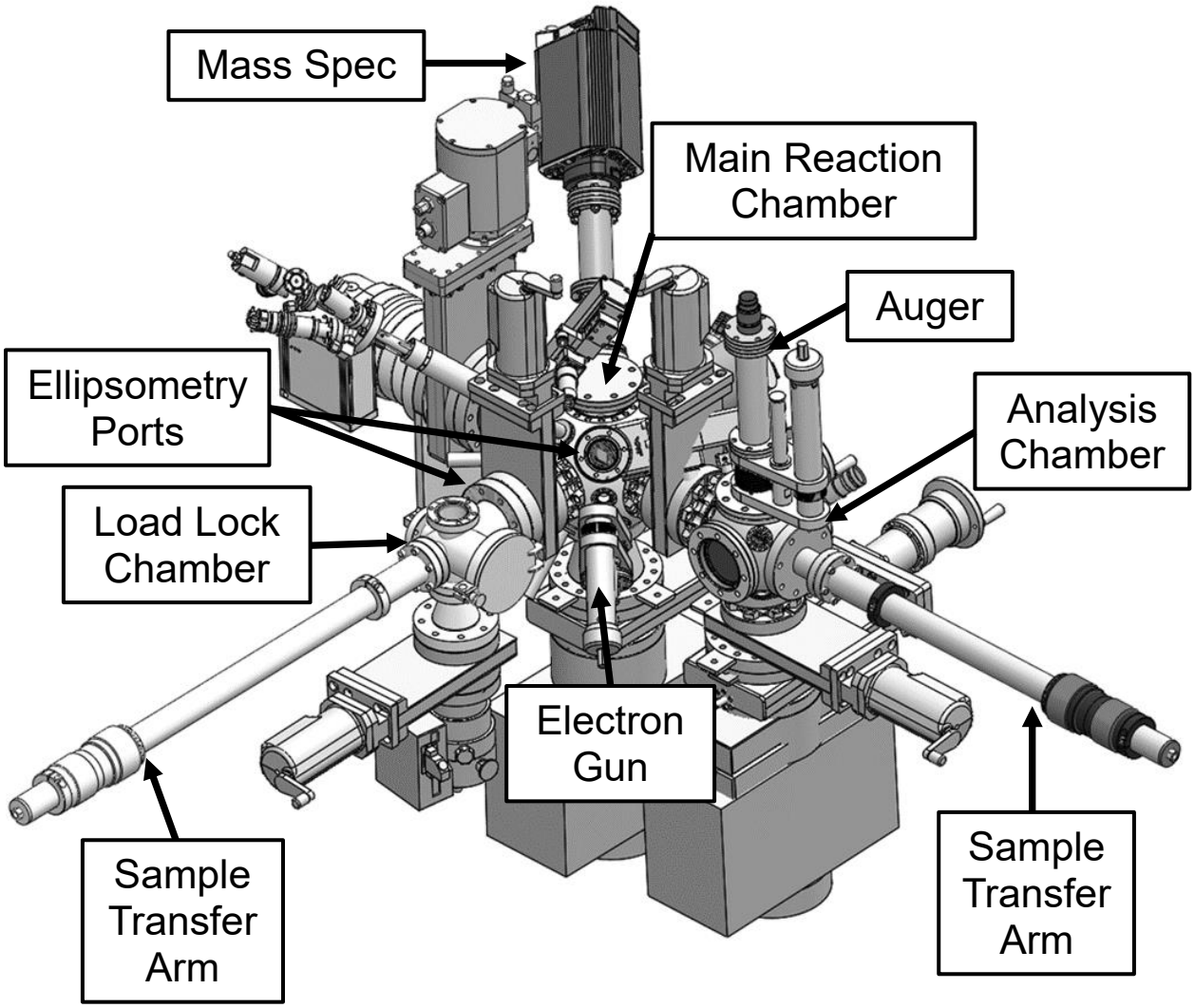

Figure 3.2: Schematic of experimental apparatus showing sample load lock, main chamber and sample analysis chamber.

Some additional experimental changes were also made compared with the earlier study of electron-enhanced GaN growth.[140] The hydrogen atom beam source (HABS) (MBE-Komponenten GmbH) was moved to the surface analysis chamber for initial substrate surface cleaning. The new location for the HABS placed the hydrogen radical outlet within 1 cm of the substrate and normal to the surface. This location greatly increased the flux of hydrogen radicals to the surface and produced more efficient surface cleaning.

B. Chemicals and Materials

Si films were grown using disilane (Si_2H_6; 99.998%, Voltaix). Films were deposited on boron-doped Si (111) substrates (Silicon Valley Microelectronics, Inc.) that had been capped with either an Al_2O_3 ALD thin film or a $Zn_{0.55}Mg_{0.45}O$ ALD thin film grown in a different reactor. These buffer films were employed to facilitate analysis of the Si films using the compositional analysis techniques. Prior to loading in the reaction chamber, the substrates were rinsed with acetone and methanol, and then dried with N_2.

Substrates were loaded into the load lock chamber and the background pressure was reduced to 1×10^{-6} Torr. The chamber and substrate were irradiated with a UV lamp for 30 minutes (mini-Z, RBD Instruments) to desorb water from the substrate surface and chamber walls. After the pressure in the load lock chamber was reduced to approximately 1×10^{-8} Torr, the substrate and sample stage were transferred into the main chamber. The main chamber and substrate were irradiated with UV light for 30 minutes. After irradiation, the substrate was transferred to the analysis chamber and exposed to hydrogen radicals created by the HABS using hydrogen gas (H_2; research grade, Airgas) at 1×10^{-5} Torr for 30 minutes. The hydrogen radical flux at the surface was estimated to be 5×10^{15} atoms cm^{-2} s^{-1}. The substrate was then returned to main chamber for the growth experiments. The EE-ALD was performed after the main chamber reached a base pressure of 5×10^{-10} Torr.

The Si substrate was exposed to electrons with an energy of 0-200 eV for 0-480 s. The electron current emitted from the electron gun during electron exposures was 100 μA for the growth experiments. All reactions were performed at room temperature (27˚C). The Si_2H_6 exposures were defined by pressure transients of 0-0.4 mTorr for <300 ms. These Si_2H_6 exposures were created using Si_2H_6 pressures of 0-10 Torr behind a pulsed valve (Parker Hannifin Corp.). The pulsed valve was open for 100 ms. Chamber pressures >0.4 mTorr caused the *in situ* cold cathode gauge to shut off and were not quantifiable.

Silicon CVD from Si_2H_6 on the hot yttria-coated iridium electron gun filament progressively led to the formation of silicides on the filament. Eventually, the filament failed and required replacement. The electron gun filament was changed to a tungsten-rhenium filament to mitigate this problem. In addition, as a precaution to prolong the life of the filament, wait times of 5 minutes were conducted after each electron gun exposure to allow the filament to cool to prevent Si CVD on the filament. The minimum Si CVD temperature is ~400 °C.[143] Achieving filament temperatures of <400 °C was the goal of these wait times.

A typical EE-ALD reaction sequence consisted of an electron gun exposure at 100 eV for 60 s with an electron emission current of 100 μA. A 300 s wait time was conducted to allow the electron gun filament to cool sufficiently. The surface was then exposed to a disilane dose of approximately 0.15 mTorr for <300 ms. A 30 s purge was performed to clear the chamber of disilane precursor. Three *in situ* ellipsometry scans of 1 s each were then recorded to determine the silicon film thickness. Another 120 s was utilized to allow the electron gun filament to warm up to temperature. This sequence was then repeated to reach the desired film thickness. Approximately 8.5 minutes were required to complete one full cycle of Si EE-ALD.

C. *In situ* Film Analysis

The reaction chamber was equipped with an *in situ* multi-wavelength ellipsometer (FS-1, Film Sense) to measure the film thickness and film growth rate. Measurements were performed at an incidence angle of 55°. Prior to the EE-ALD, a scan of the substrate was recorded to establish the baseline. The film growth was determined using a Cauchy model. During growth, three consecutive 1 s scans were collected 30 s after each Si_2H_6 exposure. Film thicknesses obtained from these three scans were averaged together to determine the film thickness after each Si_2H_6 exposure. Growth rates were determined from film thicknesses over 5 reaction cycles for each set of reaction parameters. The plots of thickness versus number of EE-ALD cycles were linear.

Film composition was determined with *in situ* Auger electron spectroscopy (AES) (microCMA, RBD Instruments). The AES spectrometer scanned a kinetic energy range of 30-730 eV with a step size of 1 eV. The electron beam potential was 2.5 kV with a filament current of 2.6 A. The AES data was collected and processed using CMapp (RBD Instruments) software.

D. *Ex situ* Film Analysis

The Si films were analyzed using a variety of *ex situ* techniques. Additional film thickness measurements were performed using a spectroscopic ellipsometer (Model M-2000, J.A Woollam Co., Inc.). This ellipsometer was equipped with focusing probes that reduced the beam size to ~300-400 μm and allowed for spatial mapping of the ~1 cm^2 growth area. Data was collected at 65° and 70° incidence angles. The SE data was fitted with a Cody-Lorentz model using CompleteEASE (J.A Woollam Co., Inc.) software.

The film composition was determined by X-ray photoelectron spectroscopy (XPS) analysis using an X-ray photoelectron spectrometer (PHI 5600). The spectrometer used a monochromatic Al-Kα source at 1486.6 eV. The pass energy was 29.35 eV and the step size was

0.25 eV. An electron beam neutralizer was used during the XPS measurements. XPS depth-profiling and surface carbon removal was conducted using argon ion sputtering. The XPS data was collected using Auger Scan (RBD Instruments) software. The XPS data was analyzed in CASA XPS (Casa Software Ltd.) software.

The Si films were studied using grazing incidence X-ray diffraction (GIXRD) to determine if the films were crystalline. These GIXRD studies were performed with an X-ray diffractometer (D1 System, Bede Scientific Inc.). The GIXRD utilized Cu-Kα irradiation at an incidence angle of 0.3°.

IV. Results and Discussion

A. Film Growth and Characterization Using *in situ* Multi-Wavelength Ellipsometry

The film thicknesses versus number of EE-ALD cycles are shown in Figure 3.3. These *in situ* measurements were performed after each Si_2H_6 exposure. The reaction conditions consisted of an electron energy of 50 eV, electron exposure times of 60 s, and Si_2H_6 doses of 0.15 mTorr for <300 ms. The Si films show a slight nucleation delay of ~35 cycles when grown on a Si(111) substrate that had been capped with an Al_2O_3 ALD film with a thickness of ~200 Å. After the nucleation delay, the film thickness versus number of EE-ALD cycles was linear. The growth rate of 0.15 Å/cycle was determined by fitting the linear portion of the data in Figure 3.3. This growth rate is consistent with sub-monolayer silicon growth.

The growth rate of the Si films was dependent on the electron energy used for hydrogen ESD. Figure 3.4 shows the film thickness versus cycle number for electron energies of 30, 88 and 150 eV. The experiments were performed with electron exposure times of 60 s and Si_2H_6 dose pressures of 0.15 mTorr for <300 ms. The film thickness versus cycle number is linear.

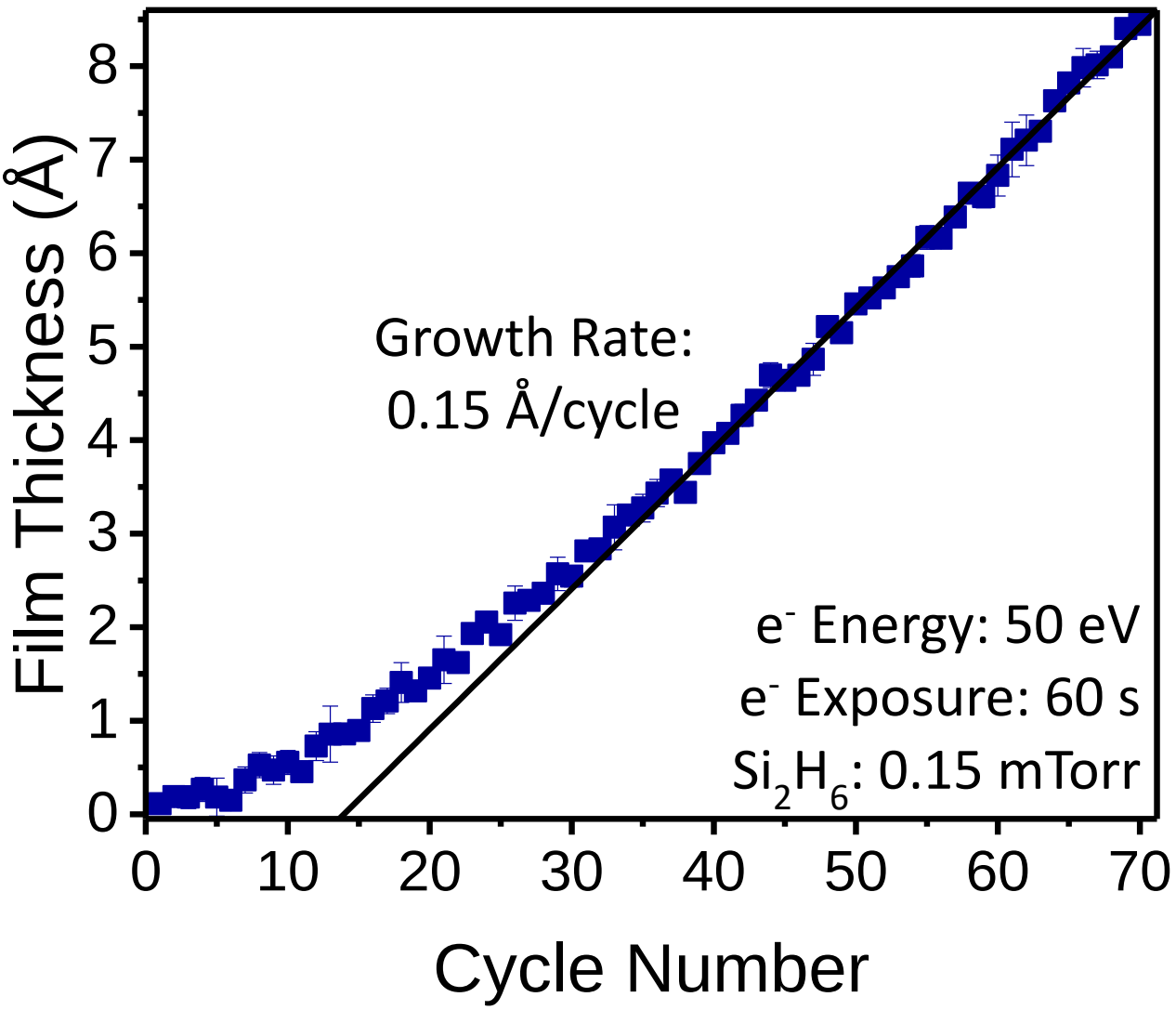

Figure 3.3: Si EE-ALD on an Al_2O_3/Si(111) substrate displaying a growth rate of 0.15 Å/cycle after an initial nucleation period of ~35 cycles. Electron energy was 50 eV, electron exposure time was 60 s, and Si_2H_6 dose pressure was 0.15 mTorr for <300 ms.

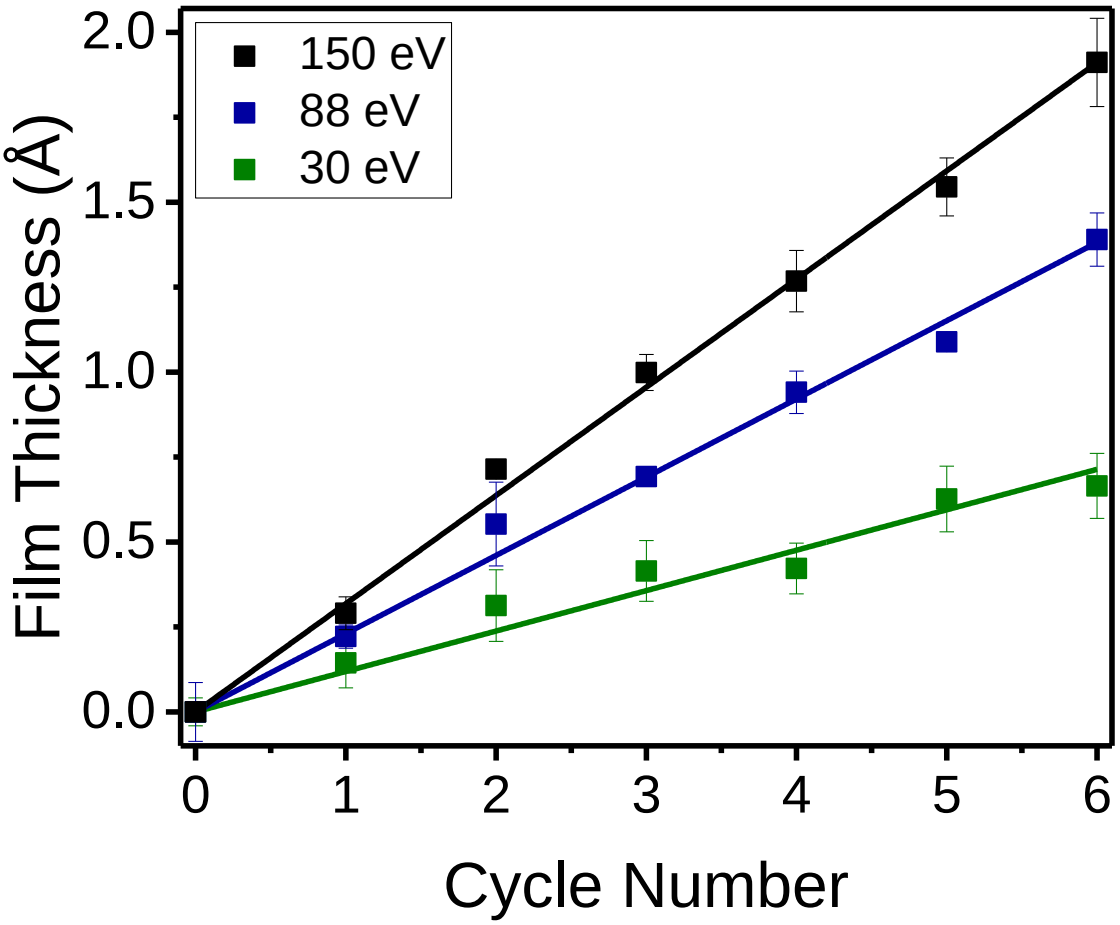

Figure 3.4: Film thickness versus number of reaction cycles for electron energies of 30, 88 and 150 eV. Electron exposure time was 60 s and Si_2H_6 dose pressure was 0.15 mTorr for <300 ms.

The silicon growth rate is larger at the higher electron energies. Silicon growth rates of approximately 0.1, 0.2, and 0.3 Å/cycle were obtained at 30, 88 and 150 eV, respectively.

Figure 3.5 summarizes the silicon growth rate dependence on electron energy from 0-200 eV. Measurements are displayed for two separate sample sets and illustrate the reproducibility of the results. The silicon growth was linear at all of the electron energies. All experiments were performed with electron exposure times of 60 s and Si_2H_6 dose pressures of 0.15 mTorr for <300 ms.

Little to no Si film growth is observed until reaching the threshold for silicon growth at an electron energy of ~25 eV. The threshold for silicon growth at ~25 eV is close to the measured threshold for hydrogen ESD from silicon at ~23 eV.[124,144-146] This threshold is believed to represent the energy required to excite two holes into Si-H valance bonds. This excitation yields hydrogen desorption and leaves behind a dangling bond.[124,144,145]

Figure 3.5 reveals that the silicon growth rate is ~0.15 Å/cycle between 50-80 eV before increasing rapidly around 85-90 eV. An increase in hydrogen ESD from silicon was also measured earlier at ~100 eV.[124] This increase is likely correlated with the Si 2p core-level binding energy at 99 eV. Desorption of hydrogen at this energy is attributed to electron removal from the Si 2p core level and an Auger decay to the Si 2p core level leaving a hole in the Si-H bond.[124]

A fairly constant silicon growth rate of ~0.27 Å/cycle is measured between 100-150 eV. Subsequently, Figure 3.5 shows that there is a decrease in the silicon growth rate at ~155 eV. In contrast, there is a corresponding increase in the hydrogen ESD from silicon.[124] This increase was attributed to electron removal from the Si 2s core level and an Auger decay to the Si 2s core level at 150 eV that desorbs hydrogen. For the silicon growth rates shown in Figure 3.5, the

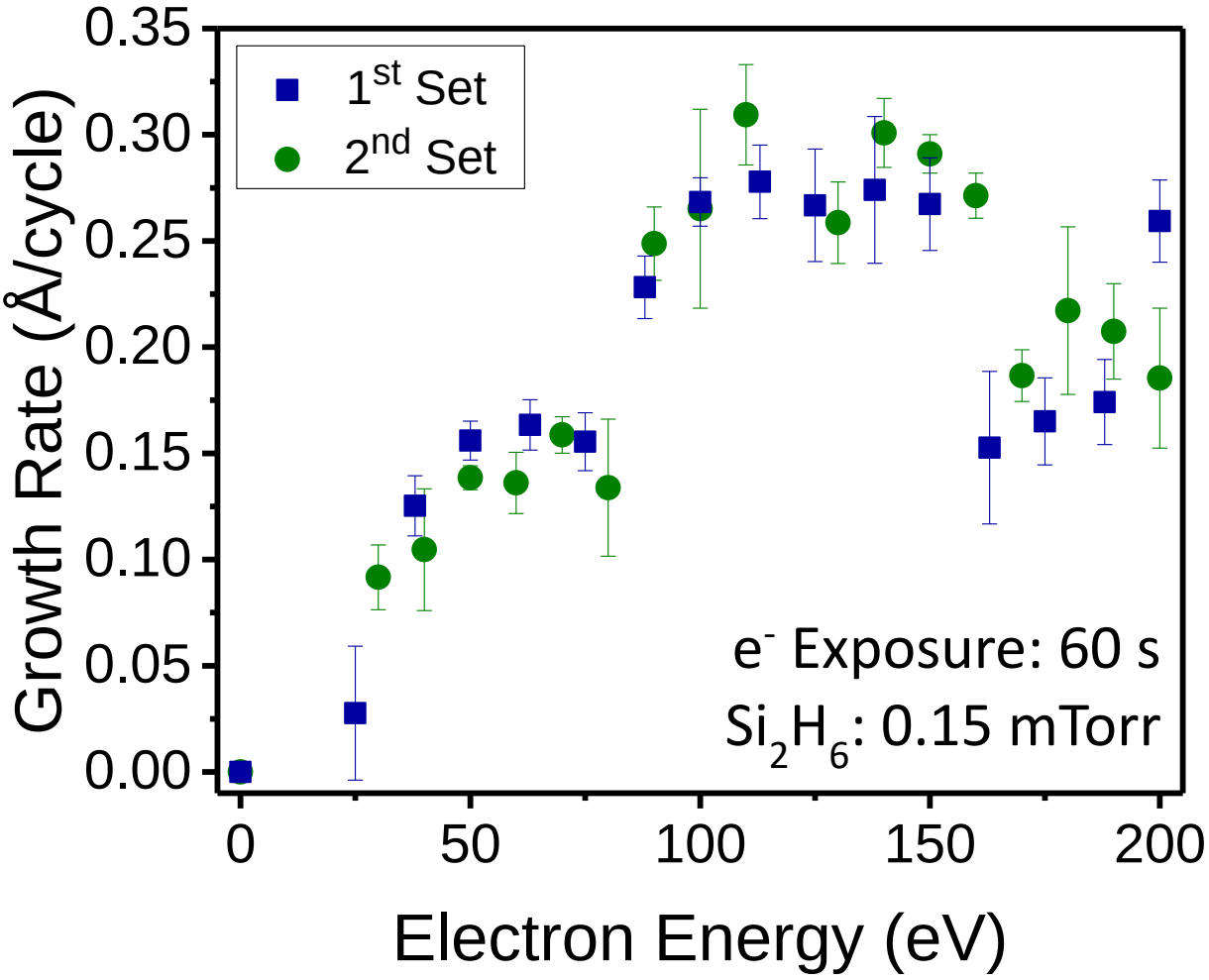

Figure 3.5: Growth rate for Si EE-ALD films versus electron energy. Electron exposure time was 60 s and Si_2H_6 dose pressure was 0.15 mTorr for <300 ms.

Auger decay to the Si 2s core level is believed to desorb Si species in addition to hydrogen. This competing Si etch process is observed as a decrease in the silicon growth rate.

B. Self-Limiting Growth Characterization

Experiments were performed to determine if the silicon growth rate was self-limiting at larger Si_2H_6 exposures. These investigations were conducted by varying the Si_2H_6 pressure behind the pulsed valve from 1 – 10 Torr for a valve open time of 100 ms. These Si_2H_6 doses resulted in chamber pressure excursions of 0 – 0.4 Torr for < 300 ms. Experiments were also performed to determine if the silicon growth was self-limiting at longer electron exposure times. These investigations varied the electron exposure time at a constant electron current with an electron energy of 100 eV.

Figure 3.6 shows the dependence of the silicon growth rate on the Si_2H_6 dose pressure for a Si_2H_6 pressure transient of <300 ms. As the Si_2H_6 dose pressure increases, there is a corresponding increase in silicon growth rate until self-limiting behavior is observed for Si_2H_6 dose pressures greater than 0.15 mTorr. The limiting factor is believed to be the consumption of available dangling bonds. After Si_2H_6 exposures sufficient to react with all of the available dangling bonds, there is no additional increase in the silicon growth rate at higher Si_2H_6 dose pressures.

Figure 3.7 displays the silicon growth rate versus the electron exposure time. These measurements were again performed with an electron energy of 100 eV and electron exposure times of 60 s. The Si_2H_6 dose pressure was 0.15 mTorr for <300 ms. The silicon growth rate increases rapidly with electron exposure time and levels off at ~0.32 Å/cycle for electron exposure times longer than 120 s. This self-limiting behavior is believed to result from the

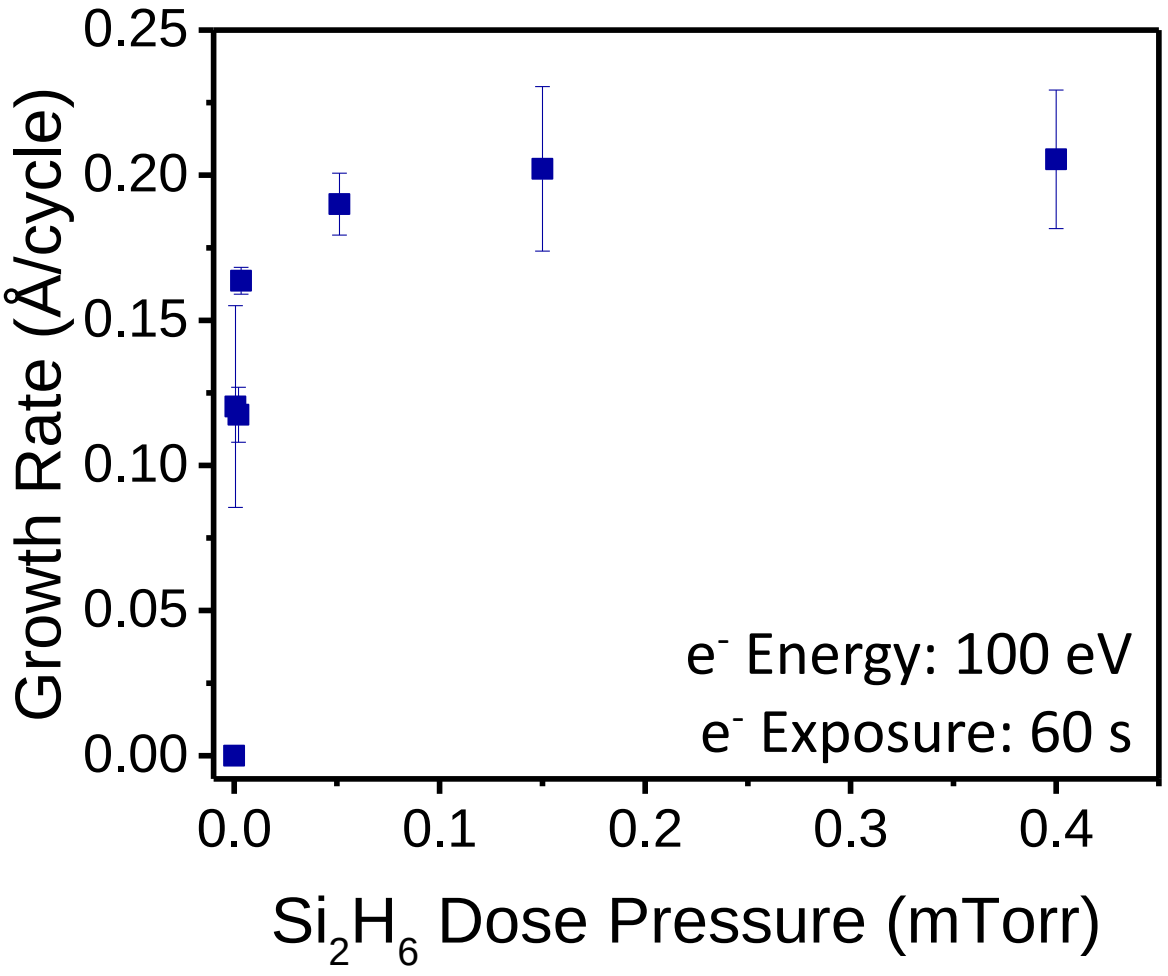

Figure 3.6: Growth rate versus Si_2H_6 dose pressures for exposure times of <300 ms. Electron energy was 100 eV and electron exposure time was 60 s.

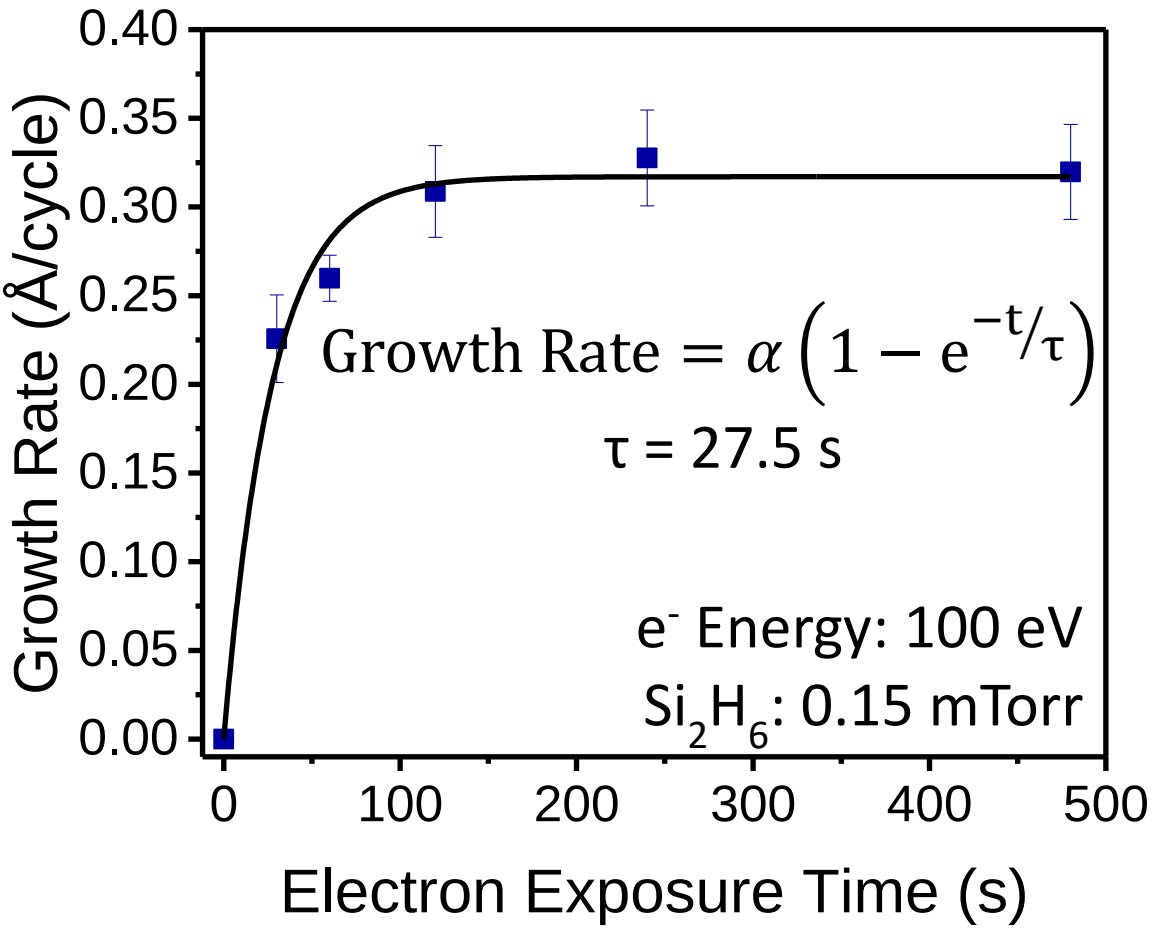

Figure 3.7: Growth rate of Si EE-ALD films versus electron exposure times. Electron energy was 100 eV and Si_2H_6 dose pressure was 0.15 mTorr for <300 ms. Silicon growth rate was proportional to $(1 - e^{-t/\tau})$. Hydrogen ESD cross section determined from τ was $\sigma = 5.8 \times 10^{-17}$ cm^2.

production of a limiting number of dangling bonds that can adsorb Si_2H_6 during the subsequent Si_2H_6 exposure.

The silicon growth rate of ~0.32 Å/cycle obtained from the results in Figure 3.7 is the maximum silicon growth rate given the available reaction parameters. This silicon growth rate can be compared with the silicon growth rate measured earlier using STM-ESD to desorb hydrogen followed by disilane adsorption on the dangling bonds. Sequential cycles of hydrogen desorption from Si(100) by STM-ESD and disilane adsorption produced silicon growth rates of ~0.43 Å/cycle.[138] This silicon growth rate is close to the silicon growth rate of ~0.32 Å/cycle obtained from Figure 3.7.

The slightly smaller growth rate for EE-ALD may reflect the differences between the Si(100) surface used in the STM-ESD work and the silicon surfaces in this work. In addition, the hydrogen ESD was conducted at 7 eV in the STM-ESD experiments compared with the electron energies of 100 eV for the results in Figure 3.7. The mechanism for STM-ESD at these lower electron energies is believed to involve multiple vibrational excitation of the Si-H bond.[136] The different electron energies and ESD desorption cross sections may affect the amount of hydrogen that can be desorbed from the silicon surfaces. Fewer dangling bonds on the silicon surface would lead to less Si_2H_6 adsorption and lower silicon growth rates.

Disilane (Si_2H_6) will dissociatively adsorb on dangling bonds on silicon surfaces. At room temperature and lower temperatures, Si_2H_6 will adsorb and produce SiH_3 and SiH_2 features in the infrared absorption vibrational spectrum.[147,148] Based on the vibrational spectra and identical measured sticking coefficients for Si_2H_6 and Si_2D_6 on Si(100) and Si(111)7x7 surfaces, disilane is believed to dissociatively adsorb by breaking the Si-Si bond to produce $–SiH_3$ surface surfaces.[149,150] However, some infrared absorption studies and theoretical analysis also suggests

that Si_2H_6 can adsorb by breaking a Si-H bond to produce Si-H and Si-Si_2H_5 surface species.[151,152]

Both Si-Si and Si-H bond-breaking adsorption pathways for Si_2H_6 would require at least two dangling bonds on the silicon surface. The silicon growth rate of ~0.32 Å/cycle can be used to estimate the number of dangling bonds on the silicon surface that react with Si_2H_6 assuming that each Si_2H_6 molecule that adsorbs requires two dangling bonds. The silicon growth of ~0.32 Å/cycle is consistent with the deposition of 1.6×10^{14} Si/cm^2 per cycle assuming a silicon number density of 5.0×10^{22} Si/cm^3. A deposited silicon coverage of 1.6×10^{14} Si/cm^2 per cycle would require at least 1.6×10^{14} dangling bonds/cm^2 per cycle.

This required dangling bond coverage of 1.6×10^{14} dangling bonds /cm^2 per cycle is less than the dangling bond coverage of 3.4×10^{14} dangling bonds/cm^2 on the reconstructed Si(100)2x1 surface and 3.1×10^{14} dangling bonds/cm^2 on the reconstructed Si(111)7x7 surface. However, the –SiH_3 species may decompose further upon adsorption to produce additional hydrogen by $SiH_3 \rightarrow SiH_2 + H$.[114,115,147] This decomposition would require additional dangling bonds and a total dangling bond coverage of at least 3.2×10^{14} dangling bonds/cm^2. This estimated required dangling bond coverage is very close to the dangling bond coverage on the reconstructed Si(100)2x1 and Si(111)7x7 surfaces.

C. Hydrogen ESD Cross Section

The hydrogen ESD cross section at 100 eV can be determined from the silicon growth rate versus electron exposure time at 100 eV presented in Figure 3.7. This determination assumes that the silicon growth is occurring as the result of hydrogen ESD producing dangling bonds. These dangling bonds then react with Si_2H_6 molecules to produce silicon growth. If there are no dangling bonds produced by hydrogen ESD, then no silicon growth should occur.

This behavior was confirmed by control experiments where the electron exposures were replaced with a wait time and every other reaction step remained the same. These control experiments revealed that the electrons were essential for silicon growth.

Assuming that the silicon surface is hydrogen terminated, hydrogen ESD produces a coverage of dangling bonds that is inversely proportional to the hydrogen surface coverage, Θ_H. The rate of change in the hydrogen surface coverage during hydrogen ESD can be described by:[153,154]

$$d\Theta_H/dt = -\Phi\sigma\Theta_H \quad (3.1)$$

In Equation 1, Φ is the electron flux across the surface (e^-/cm^2s), σ is the total hydrogen desorption cross section (cm^2), and $\Theta_H(t)$ represents the hydrogen surface coverage as a function of time. Solving the above differential equation results in:

$$\Theta_H/\Theta_{H0} = \exp(-\Phi\sigma t) \quad (3.2)$$

where Θ_{HO} is the initial hydrogen coverage. Equation 2 can be rewritten in terms of the time constant, τ, in (s), where $\tau = (1/\Phi\sigma)$. This definition of τ yields:

$$\Theta_H/\Theta_{H0} = \exp(-t/\tau) \quad (3.3)$$

Equation 3 describes the hydrogen coverage on the surface. The remaining coverage should be comprised of dangling bond sites. Therefore, the dangling bond coverage, Θ_{DB} can be expressed as:

$$\Theta_{DB}/\Theta_{DB0} = 1 - \exp(-t/\tau) \quad (3.4)$$

where Θ_{DBO} is the maximum dangling bond coverage which is equivalent to Θ_{HO}. This treatment assumes that the dangling bond sites produced by hydrogen ESD do not undergo reconstruction.

Based on the initial assumption that the silicon growth rate is proportional to the dangling bond coverage given by Equation 4, the silicon growth rate, R_{Si}, is:

$$R_{Si} = \alpha [1 - \exp(-t/\tau)] \quad (3.5)$$

In Equation 5, α represents the maximum silicon growth rate assuming ideal conditions with no reactants besides Si_2H_6 competing for the dangling bonds. The experimental results in Figure 3.7 at 100 eV can be fit by Equation 5. The line in Figure 3.7 shows the fit with α = 0.32 Å/cycle and τ = 27.5 s.

The electron stimulated hydrogen desorption cross section can then be obtained from these fitting parameters. The earlier definition of $\tau = (1/\Phi\sigma)$ can be rearranged to yield an equation for the cross section:

$$\sigma = 1/\Phi\tau \quad (3.6)$$

In Equation 6, the electron flux is defined as Φ= I/Ae where I is the electron current, A is the electron beam area and e is the charge of an electron. In these experiments, I = 100 μA and A = 1 cm^2. Using these experimental parameters together with τ from the fit to Figure 3.7, the hydrogen ESD cross section at 100 eV is $\sigma = 5.8 \times 10^{-17}$ cm^2.

As a comparison, the hydrogen ESD cross section measured on Si(100) at 100 eV is $\sigma = 7 \times 10^{-19}$ cm^2.[124] The hydrogen ESD cross section measured on Si(111) at 100 eV is $\sigma = 9 \times 10^{-20}$ cm^2.[66] The deuterium ESD cross section is lower than the hydrogen ESD cross section. The deuterium ESD cross section measured on Si(111) at 100 eV is $\sigma = 2 \times 10^{-21}$ cm^2.[125]

Additional STM measurements of the ESD cross section at lower electron energies of 7-30 eV on Si(100) are $\sigma = 3 \times 10^{-20} - 4 \times 10^{-21}$ for hydrogen and $\sigma = 7 \times 10^{-23}$ for deuterium.[134-136]

The hydrogen ESD cross section of $\sigma = 5.8 \times 10^{-17}$ cm^2 measured in this study is over 80 times larger than the hydrogen ESD cross section of $\sigma = 7 \times 10^{-19}$ cm^2 measured on Si(100). The reason for this difference is not known at this time. One possibility is that the hydrogen ESD cross section is sensitive to the underlying structure of the silicon surface. Single-crystal silicon surfaces were employed in the previous investigations. The degree of crystallinity of the Si EE-ALD films is not known and the silicon films may have been amorphous. In addition, the silicon surfaces in this EE-ALD study contained carbon impurities at a concentration of ~10 at.% as discussed in the following section. Surface impurities may influence the hydrogen ESD cross section.

D. Composition from *in situ* AES and *ex situ* XPS Depth-Profiling Measurements

The surface composition of the Si film was established by *in situ* AES measurements. Prior to Si EE-ALD deposition, the AES scans of the surface showed only Al and O AES signals from the Al_2O_3 ALD buffer film with some carbon impurities. The Si AES signal from the underlying Si(111) wafer was below the AES detection limit. After 1300 cycles of Si EE-ALD film growth at room temperature, a strong Si AES peak was observed at 93 eV as shown in Figure 3.8. The Al AES signal was below the detection limit. The loss of the Al AES signal is expected because the Si EE-ALD film has a thickness of 185 Å as determined from *in situ* ellipsometry.

In addition to the strong Si AES peak, Figure 3.8 also observes O and C impurities at 6 at.% and 21 at.%, respectively. The C impurities may result from hydrocarbon adsorption on the dangling bonds formed by hydrogen ESD. However, the level of C impurities increased with

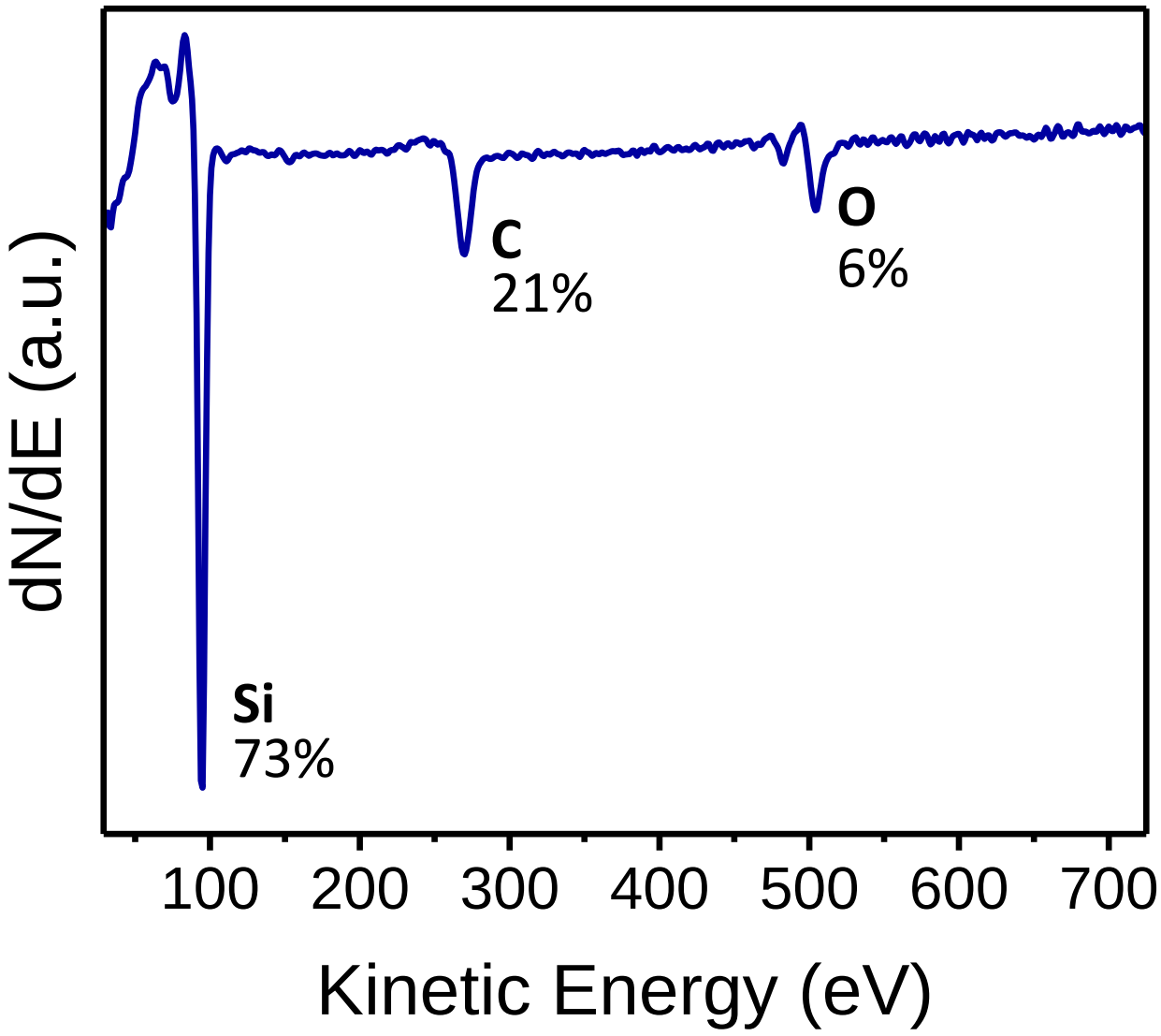

Figure 3.8: AES analysis of film grown using 1300 Si EE-ALD reaction cycles. Electron energy was 100 eV, electron exposure time was 60 s, and Si_2H_6 dose pressure was 0.15 mTorr for <300 ms.

each successive AES scan. Little increase in the C impurities was observed when the sample resided in the chamber for 24 hours. This behavior led to the conclusion that the electron filament within the AES spectrometer was at least partly responsible for producing carbon species that adsorbed onto the surface.

Figure 3.9 shows the *ex situ* XPS depth profile for a Si EE-ALD film grown at room temperature using 1000 Si EE-ALD reaction cycles on a $Zn_{0.55}Mg_{0.45}O$ ALD thin film on the Si(111) wafer. This Si film had an initial thickness of ~250 Å. The *ex situ* XPS scans reveal an oxidized silicon film resulting from atmospheric exposure. In addition, carbon is observed at ~10 at.% throughout the Si film. This result confirms that the *in situ* AES measurements were influenced by carbon produced by the AES measurements.

These XPS measurements of ~10 at.% for the carbon concentrations are more representative of the Si EE-ALD growth. Carbon could originate from residual hydrocarbons in the vacuum chamber that compete with disilane for the dangling bonds after hydrogen ESD. Mass spectrometry measurements observed low levels of methyl and other carbon species in the vacuum chamber. These species also increased in pressure during the electron exposures with the hot electron gun filament.

E. Spatial Profile of Deposition Area and XRD Measurements

The Si EE-ALD films are dependent on the electron flux to the surface as demonstrated in Figure 3.7. The Si film grew only where the electron flux was present. Figure 3.10 shows a picture of the Si film on the Si(111) wafer attached to the sample stage. This Si film was grown using 1350 cycles of Si EE-ALD with an electron energy of 50 eV, electron exposure time of 60 s and Si_2H_6 dose pressure of 0.15 mTorr for <300 ms. The deposited silicon film is visible as a circular ~1 cm^2 area on the Al_2O_3 ALD film on the Si(111) surface. The Si film growth area is

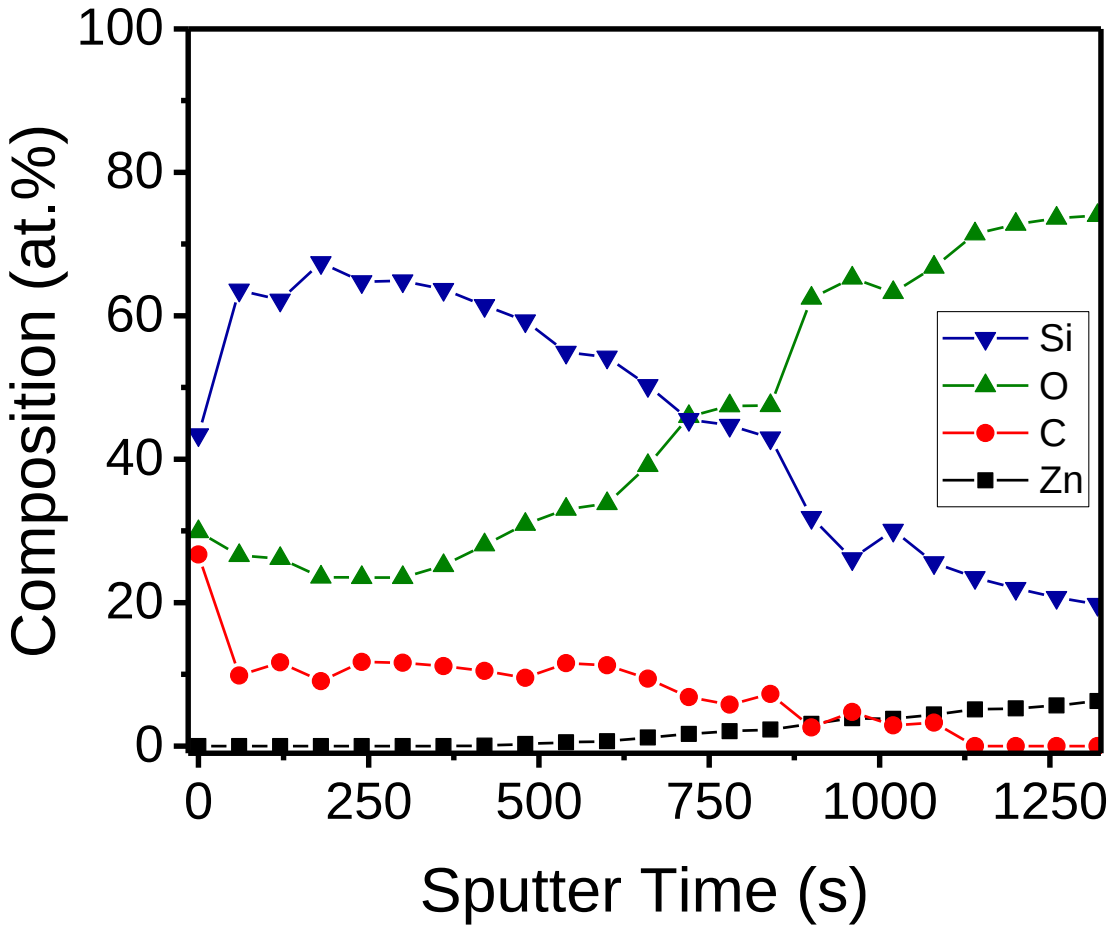

Figure 3.9: XPS depth-profile of film grown on Si(111) wafer with a $Zn_{0.55}Mg_{0.45}O$ ALD buffer layer using 1000 Si EE-ALD reaction cycles. Electron energy was 100 eV, electron exposure time was 60 s, and Si2H6 dose pressure was 0.15 mTorr for <300 ms.

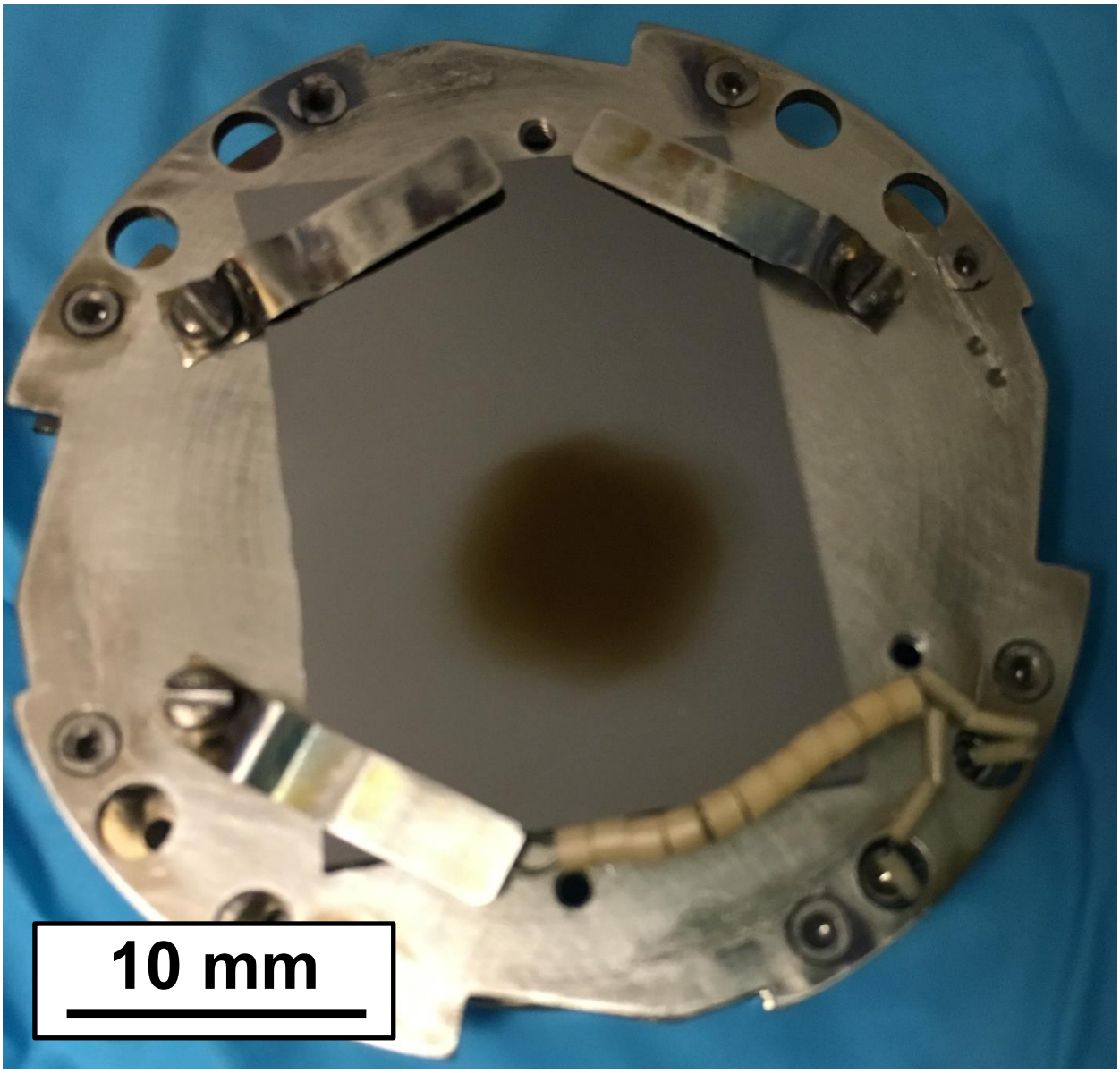

Figure 3.10: Photo of growth area on Si(111) wafer with a ~200 Å Al_2O_3 ALD buffer layer. Film was grown using 1350 Si EE-ALD reaction cycles. Electron energy was 50 eV, electron exposure time was 60 s, and Si_2H_6 dose pressure was 0.15 mTorr for <300 ms.

symmetric resulting from the incident electron flux at the surface normal and the Gaussian spatial distribution of the electron beam. Previous studies of GaN electron-enhanced growth observed growth areas that were not symmetric because the electron beam was incident on the substrate at 55° from the surface normal.[140]

Ex situ spectroscopic ellipsometry was also used to measure the film thickness and spatial profile across the Si(111) wafer. Figure 3.11 shows the thickness profile for the growth area observed in Figure 3.10. The Si film has a thickness of ~140 Å. The Si EE-ALD growth rate determined from this thickness was 0.14 Å/cycle. This Si EE-ALD growth rate is consistent with the Si EE-ALD growth rate observed at 50 eV in Figure 3.5.

Figure 3.11 reveals that the Si film shows a thickness variation of <10 Å across the ~1 cm^2 growth area. In addition, there is a sharp decrease in Si film thickness near the edge of the growth area. This fairly "flat top" with steep edges suggests that the hydrogen ESD has produced a self-limiting dangling bond coverage over much of the growth area. The dangling bond coverage then drops off rapidly near the edge of the growth area. A saturation of the dangling bond coverage over the middle of the Gaussian spatial profile of the electron beam is consistent with the saturation of the growth rate versus electron exposure time observed in Figure 3.7.

GIXRD measurements of the Si EE-ALD films did not reveal any diffraction peaks. The GIXRD results are consistent with an amorphous structure for the Si EE-ALD films following atmospheric exposure. The extensive oxidation of the Si EE-ALD films revealed by the *ex situ* XPS depth profile measurements probably removed any crystallinity that may have been present prior to atmospheric exposure. In addition, the carbon impurities at ~10 at.% would also be expected to remove silicon crystallinity.

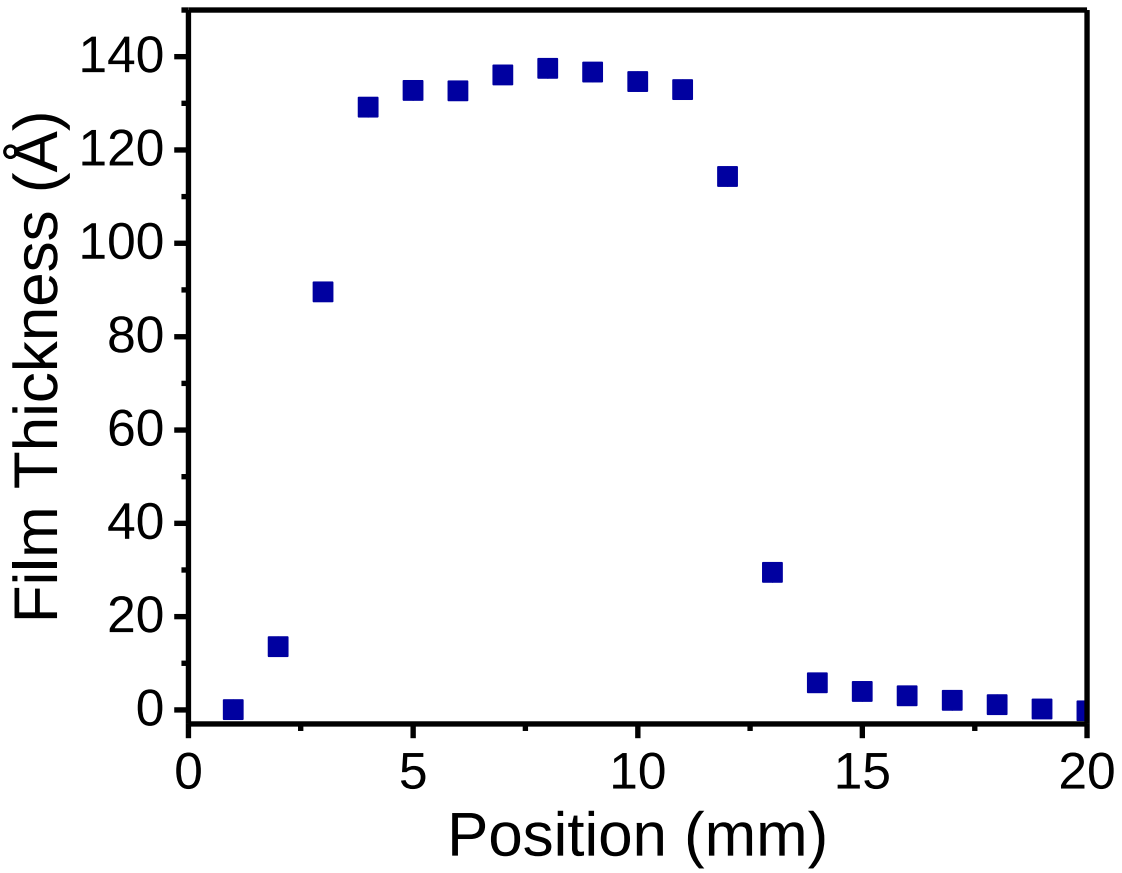

Figure 3.11: Film thickness versus spatial position for growth area observed in Figure 3.10. Film thickness is uniform over most of the region exposed to the electron beam.

In situ capping of the silicon films may prevent oxidation and facilitate the observation of crystallinity. The crystallinity might also be observed by growing much thicker Si EE-ALD films that would prevent the diffusion of oxygen deep into the bulk of the silicon films. Improvements in film crystallinity should also be possible by producing higher purity silicon films through the reduction of residual hydrocarbon species in the vacuum chamber. The effect of residual hydrocarbon species is magnified by the delay between the production of dangling bonds by the electron flux and the subsequent Si_2H_6 exposure. The long wait times of 5 minutes required for the electron gun filament to cool probably contributed to higher carbon impurities in the Si EE-ALD films.

F. Applications of Si EE-ALD

Si EE-ALD will be useful to deposit ultrathin silicon films at room temperature. Low temperatures are required for silicon deposition on polymer and other thermally fragile substrates. Silicon deposited on polymer foils can be used to fabricate flexible silicon devices such as solar cells, displays, sensors and thin film transistors.[155-158] The silicon films could also be doped using hydrides, such as B_2H_6 and PH_3, that are good candidates for hydrogen ESD following their adsorption on silicon dangling bonds. The room temperature deposition of silicon will also allow the integration of silicon with other materials by eliminating thermal expansion mismatch problems that occur when cooling down from higher temperatures.

Low temperatures are also needed to deposit silicon on substrates that would react with silicon to form silicides at higher temperature. One key application is the fabrication of Mo/Si multilayers for extreme ultraviolet (EUV) mirrors.[159] The Mo/Si multilayer mirrors have high reflectivity at λ=13.5 nm for EUV lithography for advanced semiconductor processing.[160] However, silicide formation at temperatures >210°C causes interface roughness that degrades the

reflectivity.[160,161] Silicon EE-ALD at low temperatures may provide extremely conformal silicon deposition and offer advantages to the sputter deposition techniques that are currently employed to fabricate the Mo/Si multilayer mirrors.[159]

In addition, there are other applications that may benefit from the directional properties of the electron flux during Si EE-ALD. If the electron flux is at normal incidence to the substrate, then surfaces that are parallel to the electron flux will receive very little flux compared with surfaces that are normal to the electron flux. For example, sidewalls of trenches may be parallel to the electron flux and receive very little flux. This geometry would favor "bottom-up" filling of the trench.[162] The Si EE-ALD would occur first at the bottom of the trench and proceed up the trench with negligible deposition on the sidewalls. This "bottom-up" filling could be useful for filling high aspect ratio structures.

V. Conclusions

Silicon films were grown at room temperature using EE-ALD techniques with sequential exposures of disilane and low energy electrons in the range of 25-200 eV. The silicon film growth at low temperature results from hydrogen ESD on the silicon surface. The hydrogen removal forms dangling bonds that are able to adsorb Si_2H_6 during the subsequent Si_2H_6 exposure. The Si EE-ALD was self-limiting with respect to the Si_2H_6 exposure and the electron exposure time. The silicon films grew linearly with number of reaction cycles and growth rates of up to ~0.3 Å/cycle were observed at electron energies of 100-150 eV. These growth rates are close to the expected growth rates assuming disilane adsorption on the dangling bonds on reconstructed single-crystal silicon surfaces.

The Si EE-ALD was dependent on the electron energy. Silicon growth had a threshold around 25 eV and showed a maximum growth rate between 100 - 150 eV. The silicon growth

rate then decreased above 155 eV. There was a correlation between the silicon growth rates and the silicon core electron energies. This correlation argues that at least part of the silicon growth mechanism is related to electron removal from silicon core levels and the resulting Auger decay. Fitting the silicon growth rate versus electron exposure time yielded a hydrogen ESD cross section of $\sigma = 5.8 \times 10^{-17}$ cm^2.

The silicon films were grown using an electron flood gun that produced silicon film growth over areas of ~1 cm^2. The silicon growth was very uniform over the area irradiated by the electron beam. The Si EE-ALD films contained carbon concentrations of ~10 at.%. The carbon impurity is believed to result from residual hydrocarbons in the vacuum chamber that compete with disilane for the dangling bonds during silicon film growth. Si EE-ALD should find application for depositing ultrathin silicon films on thermally fragile substrates, preventing silicide formation, and for "bottom up" filling.

VI. Acknowledgements

This work was supported by Defense Advanced Research Projects Agency (DARPA) under Grant W911NF-13-1-0041. The authors thank Tyler McQuade and Anne Fischer from DARPA for their support and helpful comments. The authors also acknowledge Kenneth Smith and Donald David from the University of Colorado Integrated Instrument Development Facility for their help with system design, development and computer interfacing. In addition, the authors thank Jonas Gertsch and Diane Lancaster for growing the ALD buffer layers.

Chapter 4: Electron Enhanced Atomic Layer Deposition of Boron Nitride Thin Films at Room Temperature[163]

Jaclyn K. Sprenger[1], Huaxing Sun[1], Andrew S. Cavanagh[1], Alexana Roshko[2], Paul Blanchard[2] & Steven M. George[1,3]

[1]Department of Chemistry and Biochemistry, University of Colorado, Boulder, CO 80309; [2]National Institute of Standards and Technology, Boulder, CO 80305; and [3]Department of Mechanical Engineering, University of Colorado, Boulder, CO 80309.

I. Abstract

Electron-enhanced atomic layer deposition (EE-ALD) was used to deposit boron nitride (BN) thin films at room temperature using sequential exposures of borazine ($B_3N_3H_6$) and electrons. Electron stimulated desorption (ESD) of hydrogen surface species and the corresponding creation of reactive dangling bonds facilitated borazine adsorption by reducing the required deposition temperature for BN films. *In situ* ellipsometry measurements showed that the BN films grew linearly versus the number of EE-ALD cycles. Maximum growth rates of ~3.2 Å/cycle were measured at electron energies of 80-160 eV. BN film growth was self-limiting versus borazine and electron exposures as expected for an ALD process. The calculated hydrogen ESD cross section was $\sigma = 3.9 \times 10^{-14}$ cm^2. *Ex situ* spectroscopic ellipsometry (SE) showed good uniformity in thickness across the ~1 cm^2 area of the BN film defined by the electron beam. *Ex situ* x-ray photoelectron spectroscopy (XPS) and *in situ* Auger spectroscopy revealed high purity boron-rich BN films with C and O impurity levels <3 at.%. *Ex situ* grazing incidence x-ray diffraction (GIXRD) measurements observed peaks consistent with textured, hexagonal BN. High-resolution transmission electron microscopy (HR-TEM) observed hexagonal and turbostratic BN aligned with the c-axis parallel to the substrate surface. Given the BN EE-ALD growth rate of ~3.2 Å/cycle that is close to the distance of 3.3 Å between BN planes in hexagonal BN, the HR-TEM images suggest that approximately one monolayer of BN

is deposited every BN EE-ALD cycle. In addition, TEM and scanning TEM/electron energy loss spectroscopy (STEM/EELS) measurements of BN EE-ALD on trenched wafers observed preferential BN EE-ALD on the top horizontal surfaces of the wafer and little deposition on the more vertical sidewalls of the trenches. This selective deposition on the horizontal surfaces suggests that EE-ALD may enable bottom-up fill of vias and trenches.

II. Introduction

Electron-enhanced processes, such as electron-enhanced atomic layer deposition (EE-ALD), can drastically reduce the temperatures required for thin film growth. The temperature reduction occurs because electrons can desorb surface species by electron stimulated desorption (ESD) to create very reactive "dangling" bonds. Precursors can then adsorb efficiently on the dangling bonds. Without ESD, thin film growth relies on thermal pathways for the desorption of surface species that require much higher temperatures. EE-ALD lowers the thermal budget and enables the deposition of thin films on thermally sensitive substrates.

Electron-enhanced thin film growth has been demonstrated previously for the deposition of polycrystalline GaN[140] and amorphous Si[164] at room temperature. The polycrystalline GaN films were deposited using sequential surface reactions, similar to atomic layer deposition (ALD) processes, using $Ga(CH_3)_3$ (trimethylgallium (TMG)), NH_3 (ammonia) and electron exposures as the reactants. Hydrogen radical beam exposures were employed after the $Ga(CH_3)_3$ exposures to replace the CH_3 groups with H surface species. The electron exposures removed surface hydrogen by hydrogen ESD. GaN growth rates of 1.3 Å/cycle were observed at room temperature at electron energies of 50 eV. The GaN growth rates were higher for larger electron fluxes.

Amorphous Si films were also deposited using sequential surface reactions using Si_2H_6 (disilane) and electron exposures as the reactants. The electron exposures again removed surface hydrogen by hydrogen ESD. Si growth rates of 0.3 Å/cycles were measured at room temperature at electron energies of 100 eV. The Si growth was self-limiting versus Si_2H_6 dose pressures for fixed electron exposure times. The Si growth was also self-limiting versus electron exposure time for fixed Si_2H_6 exposures. Changes in the silicon growth rate were also observed at electron energies corresponding with Si core level energies.

In this paper, boron nitride (BN) EE-ALD is examined using borazine ($B_3N_3H_6$) and electrons as the reactants. BN is found in many forms such as hexagonal, cubic and wurtzite BN. Hexagonal and cubic BN are analogous to graphite and diamond, respectively. Hexagonal BN is an insulating material with the same sp^2 hybridized layer structure as graphene. Hexagonal BN is known for its high thermal stability and chemical inertness. 2D materials such as graphene can be grown on hexagonal BN.[165,166] Monolayers of hexagonal BN are also used as the dielectric layer in field effect transistors.[167-169] Cubic BN is known for its high hardness and high elastic modulus.

The growth of hexagonal BN films requires very high temperatures. The standard technique for hexagonal BN growth is chemical vapor deposition (CVD) that is performed at temperatures of 800 – 1000 ˚C.[170,171] Some lower temperature BN CVD processes are employed at 400 ˚C. However, these BN CVD films generally require a post-deposition annealing process at 1000 ˚C.[172] BN ALD has been defined using BCl_3 and NH_3 as the precursors at deposition temperatures of 225 – 325 ˚C.[173-177] BN ALD has also been accomplished using BBr_3 and NH_3 as the reactants. Higher temperatures of 750 ˚C were required to obtain the turbostratic structure. The crystallographic order was less for films deposited at 400 ˚C. One of the goals of this

research was to reduce the required deposition temperature for hexagonal BN films using EE-ALD.

The reduction in deposition temperature for BN film growth using EE-ALD is achieved by ESD of hydrogen from the surface.[178,179] ESD can occur through several different processes including the Menzel-Gomer-Redhead and Knotek-Feibelman mechanisms.[31-33,126] The Menzel-Gomer-Redhead mechanism involves the excitation of a bonding orbital electron into an antibonding state that, upon relaxation, results in the dissociation of the bond and desorption of the surface species. The Knotek-Feibelman mechanism is an Auger process where a core-binding electron is displaced by the incident electron flux. A valence level electron loses energy to fall into the resulting hole and another valence electron absorbs the lost energy to leave the surface species. The ESD of hydrogen results in the creation of highly reactive "dangling" bond sites where precursors can be adsorbed with little to no activation barrier.

The BN EE-ALD films were grown using sequential cycles of borazine ($B_3N_3H_6$) and low energy electron exposures. BN films covered an area of ~1 cm^2 and were grown at room temperature (27 ˚C) and 100 ˚C using electron energies from 50-450 eV. All EE-ALD reactions were performed in an ultra-high vacuum (UHV) chamber to preserve the highly reactive "dangling" bonds after ESD. BN film growth was characterized by *in situ* multi-wavelength ellipsometry, Auger spectroscopy, and mass spectroscopy. The character and crystallinity of these BN films was studied using a variety of *ex situ* techniques including spectroscopic ellipsometry (SE), grazing incidence x-ray diffraction (GIXRD), x-ray photoelectron spectroscopy (XPS), and transmission electron microscopy (TEM).

BN EE-ALD films were also deposited on trenched wafers to evaluate EE-ALD on high aspect ratio structures. These BN EE-ALD films were analyzed using TEM and scanning

TEM/electron energy loss spectroscopy (STEM/EELS). These studies were designed to determine if the EE-ALD films were selective for deposition on horizontal surfaces. Selective deposition on horizontal surfaces could be useful for the bottom-up filling of trenches or vias during semiconductor fabrication.

III. Experimental

A. Vacuum Chamber

BN EE-ALD films were grown at room temperature and 100 ˚C in a UHV chamber which has been previously described.[140,164]

B. Chemicals and Materials

BN films were grown using borazine ($B_3N_3H_6$; >95%, Gelest). Immediately prior to each EE-ALD reaction, the borazine bubbler was frozen with liquid nitrogen and remaining gases in the line were pumped out prior to allowing the precursor to thaw. This procedure was repeated in triplicate to ensure the reactant purity as borazine is prone to degradation.[180] Borazine undergoes dehydropolymerization at temperatures greater than 70 ˚C[87,172] and can further decompose to BN and hydrogen gas.[172]

Films were deposited on boron-doped Si(111) substrates (Silicon Valley Microelectronics, Inc.). Prior to loading in the reaction chamber, substrates were rinsed with acetone and methanol, and submerged in Nano-Strip (Cyantec Corporation) for 3 minutes to remove surface contaminants. The silicon native oxide was etched and the surface hydrogen passivated by exposing the substrate to dilute hydrofluoric acid (50:1 H_2O: HF) for 2 minutes.

Substrates were loaded into the load lock chamber and the background pressure was reduced to $1x10^{-6}$ Torr. The load lock chamber and substrate were irradiated for 30 minutes using UV lamps (RBD Instruments) to desorb water from the substrate surface and chamber

walls. After the pressure in the load lock chamber was reduced to approximately 1 x 10^{-8} Torr, the substrate and sample stage were transferred into the reaction chamber. The substrate was again irradiated with UV light for 30 minutes. After irradiation, the substrate was transferred to the analysis chamber and exposed to hydrogen radicals created by the hydrogen atom beam source (HABS) using hydrogen gas (H_2; research grade, Airgas) that brought the background pressure to 1 x 10^{-5} Torr for 30 minutes. The hydrogen radical flux at the surface was estimated to be 5 x 10^{15} H atoms cm^{-2} s^{-1}. Samples were then returned to reaction chamber for the film growth. After the reaction chamber had reached a base pressure of 5 x 10^{-10} Torr, the reaction was initiated.

A typical EE-ALD reaction sequence consisted of an electron gun exposure at 100 eV for 240 s with an electron emission current of 300 μA followed by a 15 s purge. A borazine exposure of approximately 7 x 10^{-2} Torr s was then dosed into the chamber with a following 150 s purge. Three *in situ* ellipsometry scans of 1 s each were recorded 120 s into the purge to determine the BN film thickness. Another 50 s were required for the electron gun filament to warm up to emission temperature. This sequence was repeated the desired number of cycles. Approximately 7.5 minutes were required to complete one full BN EE-ALD cycle.

C. *In situ* Growth Analysis

The reaction chamber was equipped with a variety of *in situ* analysis techniques to observe film growth. Film growth rate and thickness were analyzed with a multi-wavelength ellipsometer (FS-1, Film Sense). An initial baseline scan of the substrate was taken prior to the reaction and film growth was modeled using an n & k model. During growth, three consecutive 1 s scans were collected 120 s after the borazine exposure. Growth rates were calculated by finding the linear line of best fit for the thicknesses measured in 10 consecutive reaction cycles.

In situ film composition was measured by Auger Electron Spectroscopy (AES) using a micro-cylindrical mirror analyzer (microCMA) Auger spectrometer (RBD Instruments). The microCMA Auger spectrometer scanned a kinetic energy range of 30-930 eV with a step size of 1 eV. The beam potential was 3 kV with a filament current of 1.05 A. The AES data was collected and processed using CMapp (RBD Instruments) software.

Additionally, an *in situ* mass spectrometer (PrismaPlus QMG 220M, Pfeiffer Vacuum Inc.) was available for identification of gaseous reaction by-products. The mass spectrometer could measure mass signals up to m/z = 200 amu and had an internal ion current to pressure calibration that allowed partial pressures to be estimated from ion currents.

D. *Ex situ* Film Analysis

The BN films were analyzed using a variety of *ex situ* techniques. The film thickness was determined using a spectroscopic ellipsometer (Model M-2000, J.A Woollam Co., Inc.) equipped with focusing probes which reduced the spot size to ~ 300-400 μm and allowed for spatial mapping of the growth spot. Data was collected at 65˚ and 70˚ incident angles. The SE data was fitted with a B-spline model using CompleteEASE (J.A Woollam Co., Inc.) software.

The film composition was determined by X-ray photoelectron spectroscopy (XPS) analysis using an X-ray photoelectron spectrometer (PHI 5600). The spectrometer used a monochromatic Al-Kα source at 1486.6 eV. The pass energy was 29.35 eV and the step size was 0.25 eV. An electron beam neutralizer was used during the XPS measurements. XPS depth-profiling and surface carbon removal was conducted using argon ion sputtering. The XPS data was collected using Auger Scan (RBD Instruments) software. The XPS data was analyzed in CASA XPS (Casa Software Ltd.) software.

The BN films were studied using grazing incidence X-ray diffraction (GIXRD) to determine if the films were crystalline. These GIXRD studies were performed with an X-ray

diffractometer (D1 System, Bede Scientific Inc.). The GIXRD utilized Cu-Kα irradiation at an incidence angle of 0.3°.

Raman spectra were collected with an InVia Confocal Raman Microscope (Renishaw plc.) using a 785 nm laser. Exposures were 0.02 seconds with 10,000 accumulations. Data was processed with WiRE (Renishaw plc.) software.

Fourier-transform infrared (FTIR) spectra were collected using a Bruker Tensor 27 with a DTGF detector in transmission mode. The aperture was 4 mm, the resolution was 1 cm^{-1} and 100 accumulations were acquired. Data was collected for the 4000 – 1000 cm^{-1} range and processed using OPUS (Bruker) software.

Forward recoil elastic spectroscopy (FRES) measurements was collected with an incident ion beam of 3 MeV He^{+}. The spot size was reduced to 1 mm^2 normal to the source with an incidence angle of 75˚ on the sample.

A lamella of the specimen was prepared for transmission electron microscopy (TEM) examination by focused ion beam (FIB) milling. First, protective metal layers (Ni and Pt) were deposited on the surface and then a Ga-ion beam was used to prepare a thin lamella at 30 then 5 kV. Damage induced by the FIB preparation was removed by subsequent Ar milling at 900 then 500 eV. High-resolution TEM (HR-TEM) phase contrast images were taken at 200 kV with the lamella aligned to the Si[112] zone axis.[181]

IV. Results and Discussion

A. *In situ* Film Growth and Characterization

Growth of EE-ALD BN films was studied with *in situ* multi-wavelength ellipsometry. Linear BN growth rates were observed at various electron energies. Initial film deposition experienced short, approximately 20 cycle, nucleation delays on Si(111) substrates after which

film growth was consistently observed to be linear. Figure 4.1 displays the linear growth behavior of EE-ALD BN at 120 eV, 300 eV, and 400 eV. This data was collected on a previously grown EE-ALD BN film to remove nucleation effects and have consistent optical properties to ease model generation. All other reaction parameters were within self-limiting behavior regimes. The borazine exposure was 7 x 10^{-2} Torr s and the electron emission current was 300 μA for 240 s. At an electron energy 120 eV, the observed growth rate of EE-ALD BN was linear at 3.0 Å/cycle. When the electron energy was increased to 300 eV, a decrease in the linear growth rate to 2.5 Å/cycle was observed. An additional decrease in EE-ALD growth rate was observed for 400 eV that resulted in a linear growth rate of 2.0 Å/cycle. These decreases in growth rate observed at higher electron energies are attributed to a competitive etching process becoming more prominent and acting to bring down the overall growth rate for the EE-ALD BN chemistry.

With varying linear growth rates at different electron energies observed, the impact of electron energy on the EE-ALD growth rate was studied and the results are shown in Figure 4.2. EE-ALD BN films were grown on Si(111). The reaction parameters were the same as those used for the linear growth studies. No film growth was observed with an electron energy of 0 eV. This is consistent with film growth being dependent on the electron flux across the surface. A film growth threshold between 0-40 eV was present. Previous H desorption cross section studies from Si(001) surfaces observed a threshold at 23 eV[178] and previous EE-ALD Si film growth initiated at ~25 eV.[164] Due to limitations with cycling of the electron flood gun, the growth rate in the electron energy region between 0-40 eV could not be effectively probed. A plateau in EE-ALD film growth rates at 3.0 Å/cycle was observed between 80-160 eV. At electron energies greater than 160 eV, the growth rate began to experience an overall decrease that was attributed to an

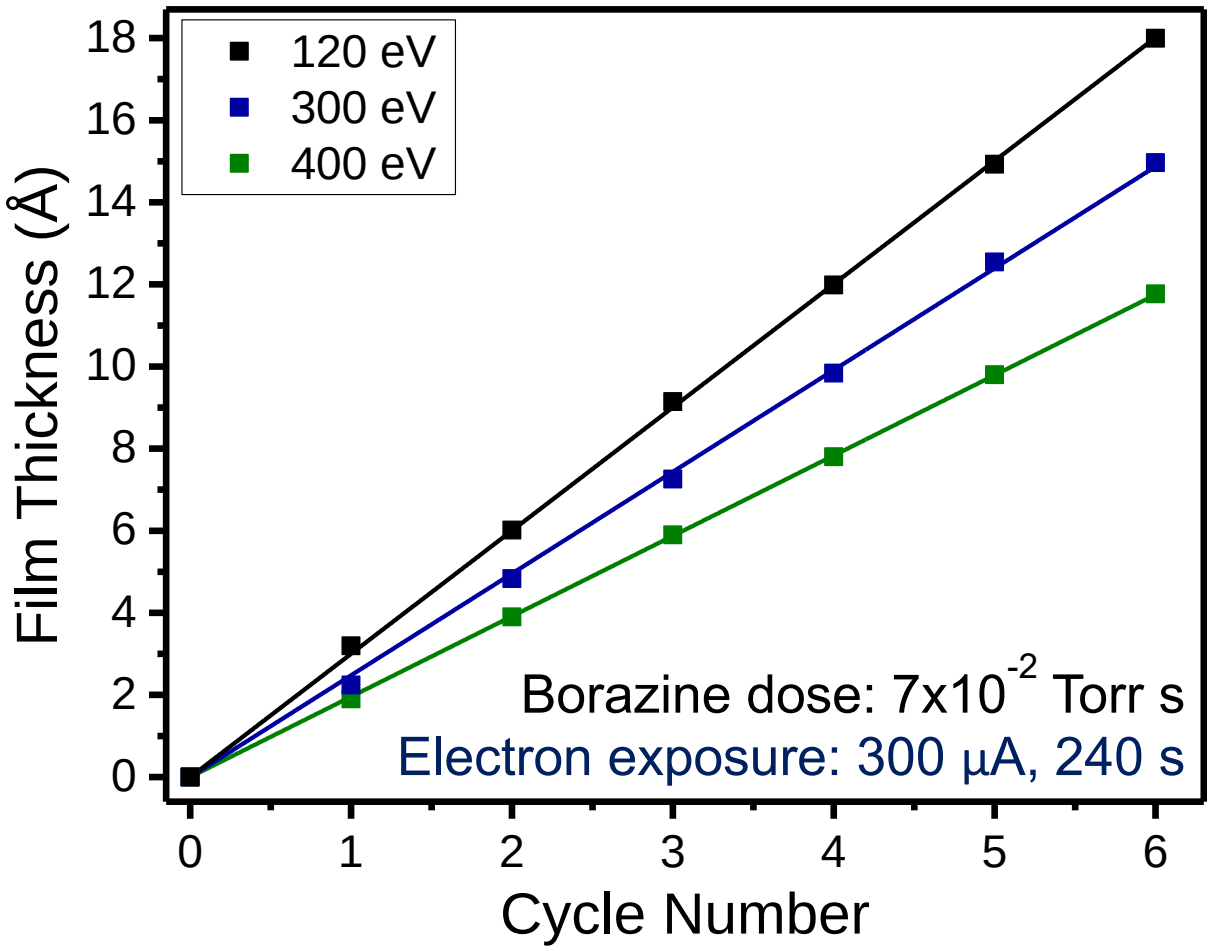

Figure 4.1: Linear growth rate of EE-ALD BN films on Si(111) substrate observed with respect to three different electron energies.

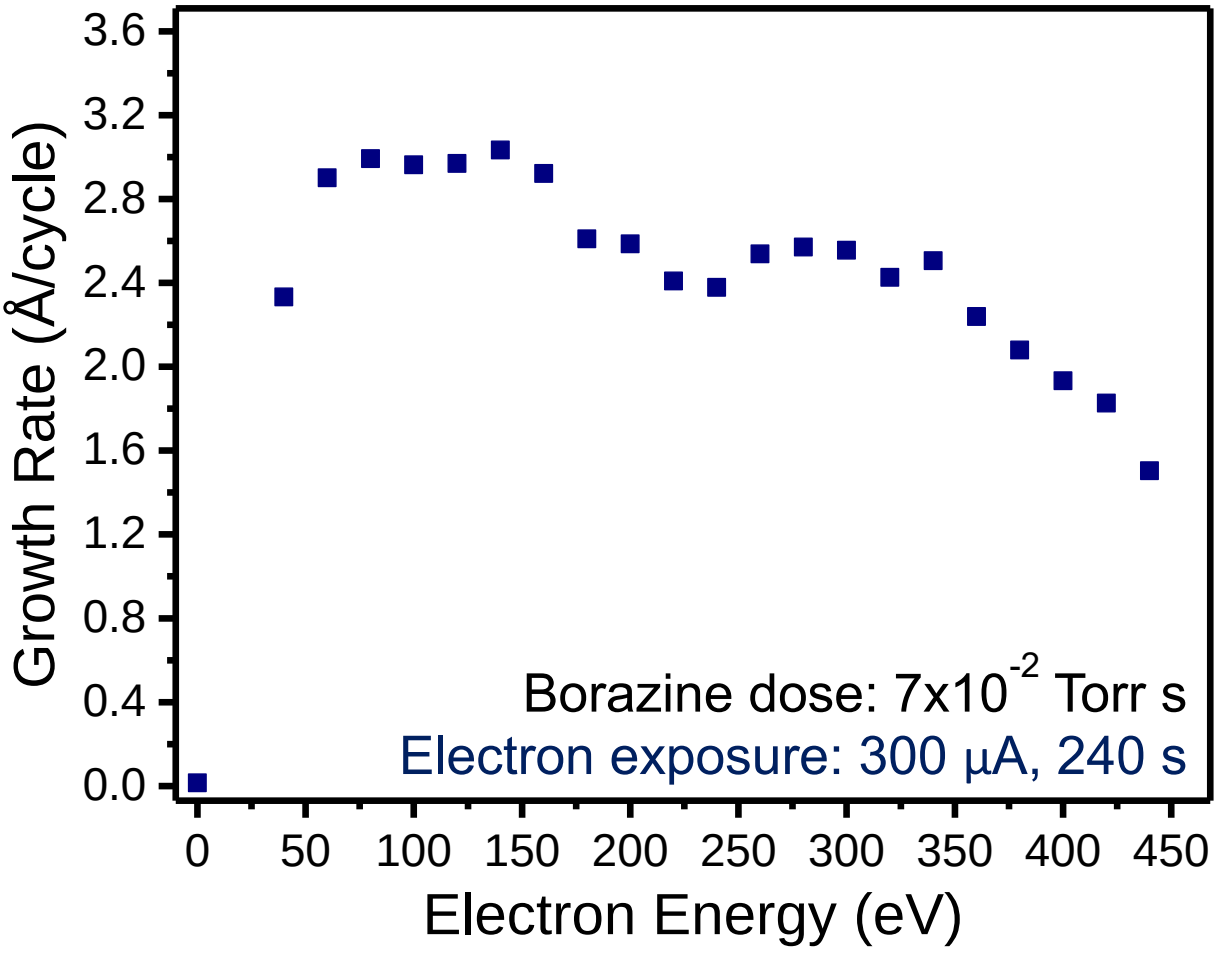

Figure 4.2: Growth rate dependence of EE-ALD BN films on Si(111) substrate based on electron energy used during each exposure.

increase in a competitive etching process of the BN film. By electron energies of 440 eV, the growth rate had halved to 1.5 Å/cycle. It is predicted that at a high enough electron energy, the competitive etch process of BN will outcompete the growth resulting in no film growth.

In order to confirm the ALD-like properties of this BN EE-ALD technique, the self-limiting behavior of BN film growth was studied with respect to each reaction parameter. Each study presented was performed with all reaction parameters, aside from the parameter of interest, held constant under self-limiting conditions. Additionally, each study was performed at 27 ˚C on a previously deposited BN film to avoid the impact of nucleation delays.

Self-limiting behavior with respect to borazine exposure was observed at greater than 7 x 10^{-2} Torr s as shown in Figure 4.3. No growth was observed without the presence of a borazine dose even with repeated electron exposures. The maximum growth rate was found to be approximately 3.0 Å/cycle at self-limiting growth conditions. The behavior of BN EE-ALD film growth was also observed to be self-limiting for electron emission currents greater than 100 μA as shown in Figure 4.4. No film growth was observed without electron exposures. The maximum growth rate found was 3.2 Å/cycle. Due to limitations of the electron gun, it was not feasible to study electron emission currents greater than 500 μA. At an emission current of 500 μA, a slight decrease in growth rate was observed. It is possible that going to higher emission currents would yield partial layer desorption, an overall reduced growth rate and possible improved film quality. Finally, self-limiting behavior was observed with respect to electron exposure time for exposures greater than 240 s as shown in Figure 4.5. Once again, no growth occurred without the present of an electron exposure. The maximum growth rate was found to be approximately 3.2 Å/cycle.

It is possible to calculate the hydrogen ESD cross section from the electron exposure time at 100 eV presented in Figure 4.5. It is assumed that the only method of film growth is through

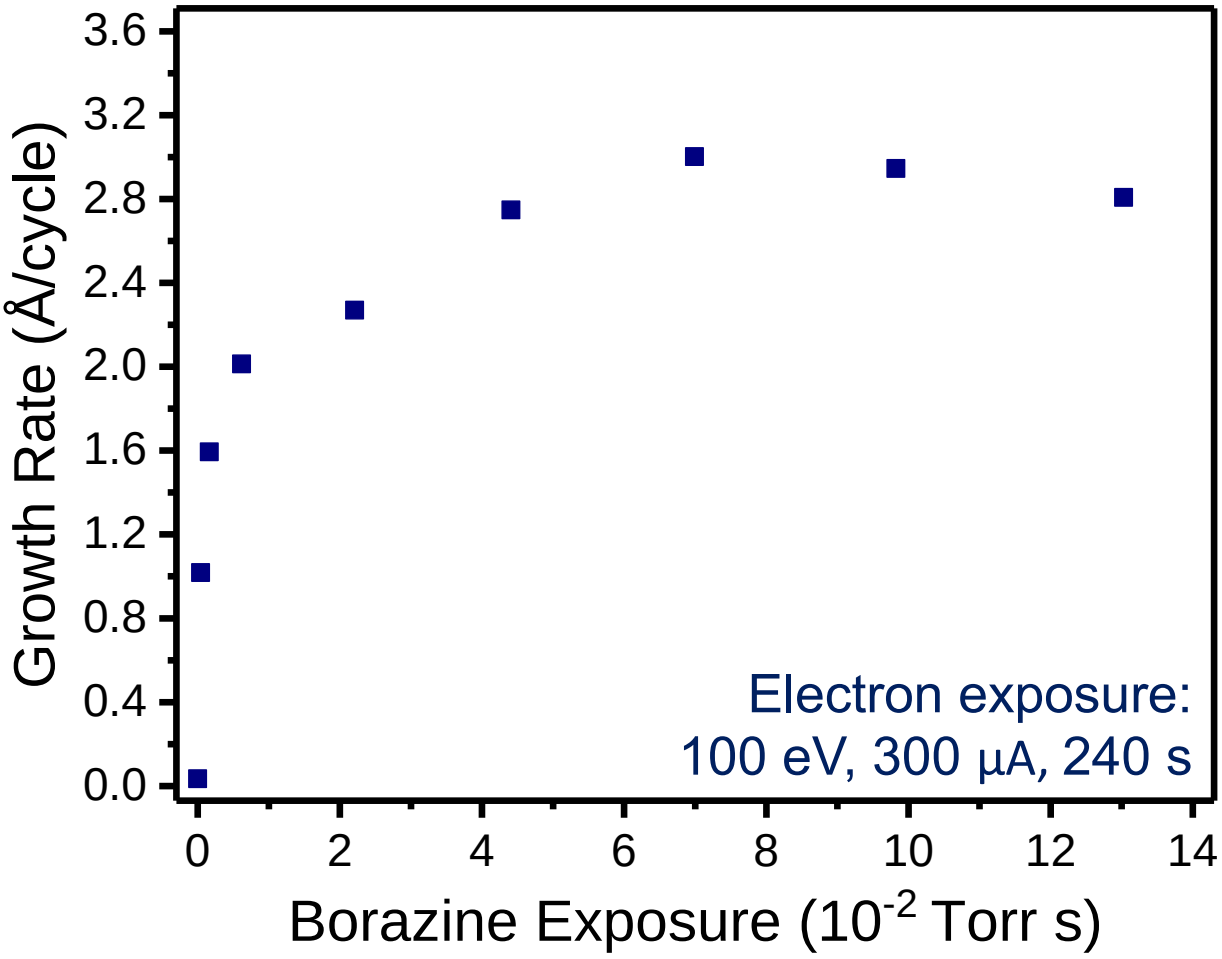

Figure 4.3: Self-limiting BN EE-ALD film growth is observed for borazine exposures greater than 7 x 10^{-2} Torr s.

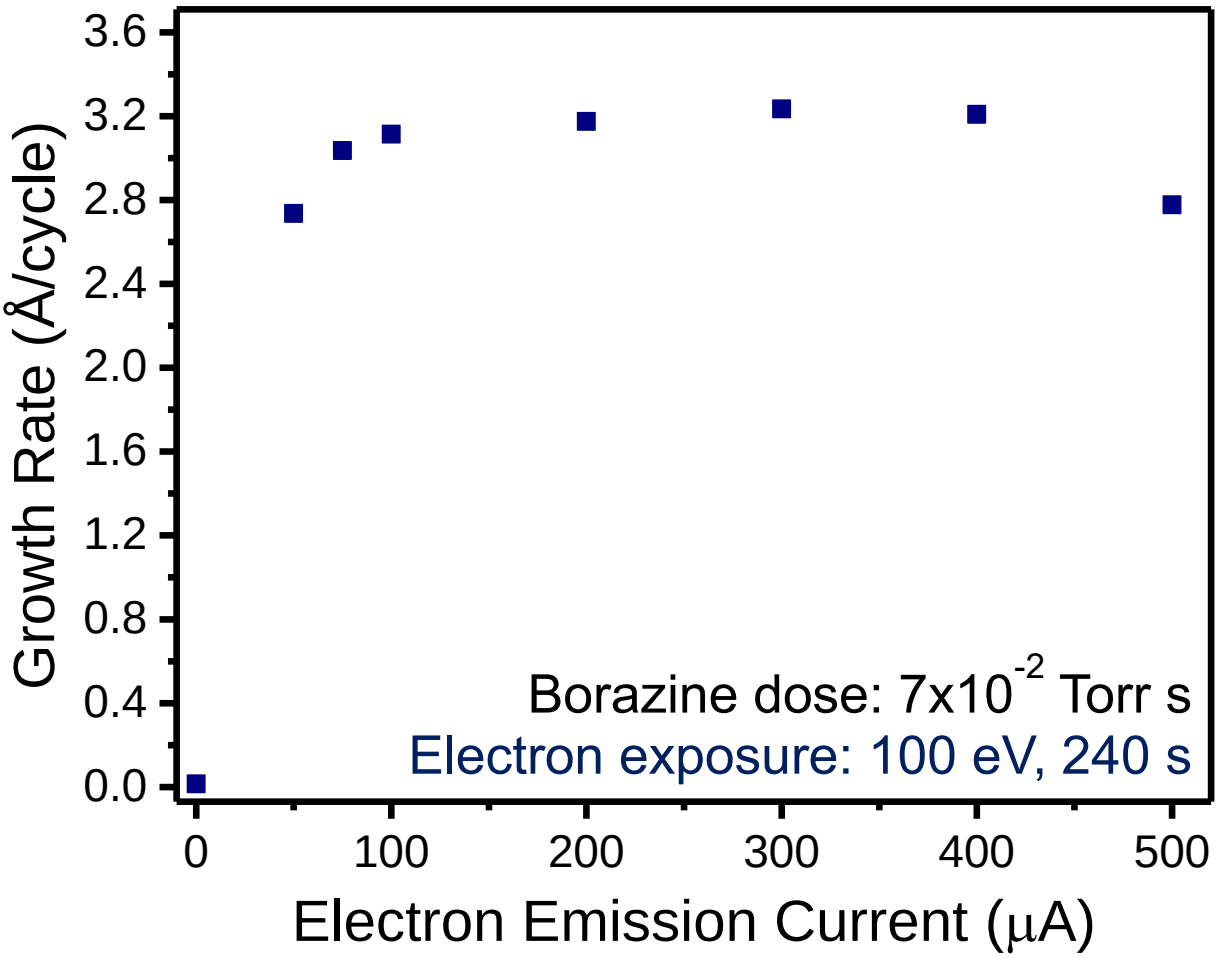

Figure 4.4: Self-limiting BN EE-ALD film growth rate is observed for electron emission currents greater than 100 μA.

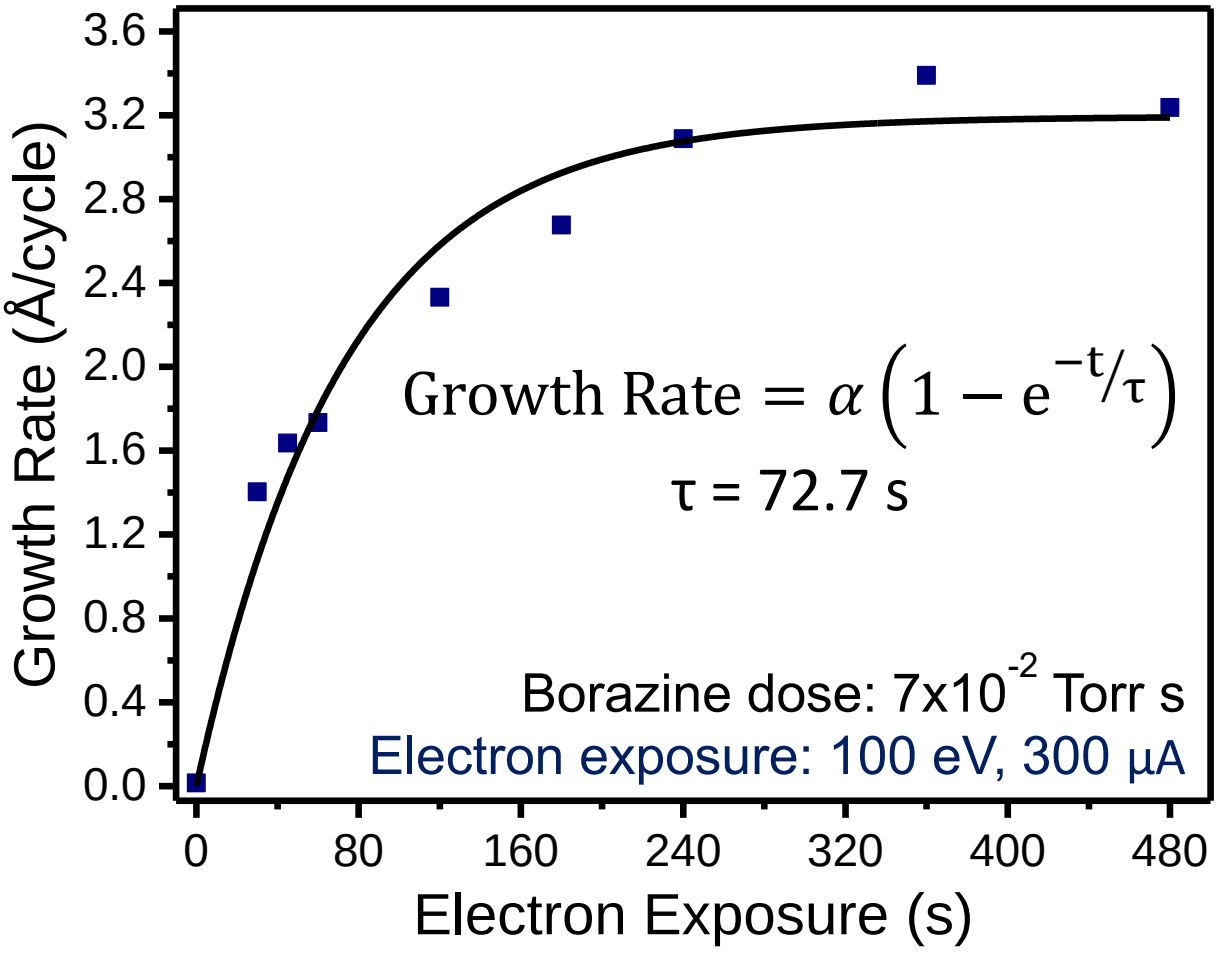

Figure 4.5: Growth rate shows self-limiting behavior with respect to the electron exposure time on the sample. Data is fit in order to determine the time constant, τ, which allows for the calculation of the electron stimulated hydrogen desorption cross section. The cross section was found to be 3.9 x 10^{-14} cm^2.

the creation of "dangling" bonds. Further, it can be assumed that the growth rate of the EE-ALD BN films is proportional to the "dangling" bond coverage. The following equation can therefore be derived:[164,182,183]

$$R_{BN} = \alpha\,[1 - \exp(-t/\tau)] \quad (4.1)$$

In Equation 4.1, R_{BN} represents the BN growth rate, α represents the maximum BN growth rate assuming ideal conditions, and τ is the time constant, in (s). The experimental results in Figure 4.5 can be fit with Equation 4.1 which results in τ = 72.7 s. The definition of τ can be rearranged to yield the hydrogen desorption cross section equation:

$$\sigma = 1/\Phi\tau \quad (4.2)$$

In Equation 4.2, σ is the total hydrogen desorption cross section (cm^2) and Φ is the electron flux across the surface (e^-/cm^2s). The electron flux is defined as Φ= I/Ae where I is the electron current, A is the electron beam area and e is the charge of an electron. For this experiment, I = 300 μA and A = 1 cm^2. The τ from the fit of the experimental results in Figure 5 together with these experimental parameters yield a hydrogen ESD cross section at 100 eV of $\sigma = 3.9 \times 10^{-14}$ cm^2. Mass spectrometry results show an increase in m/z = 2 during electron exposure periods which supports hydrogen ESD as a likely mechanism for film growth.

B. Growth Conformality

BN EE-ALD film growth is dependent on electron flux across the substrate surface as demonstrated in Figure 4.6. The electron flood gun acts as a point source of electrons located approximately 3 cm away and at normal to the substrate surface. The film growth spot is observed to be circular with an area of approximately 1 cm^2. This shape is characteristic of the Gaussian distribution of electrons originating from the electron flood gun. There is no visible BN film growth outside the electron flux region. The film pictured in Figure 4.6 was grown using

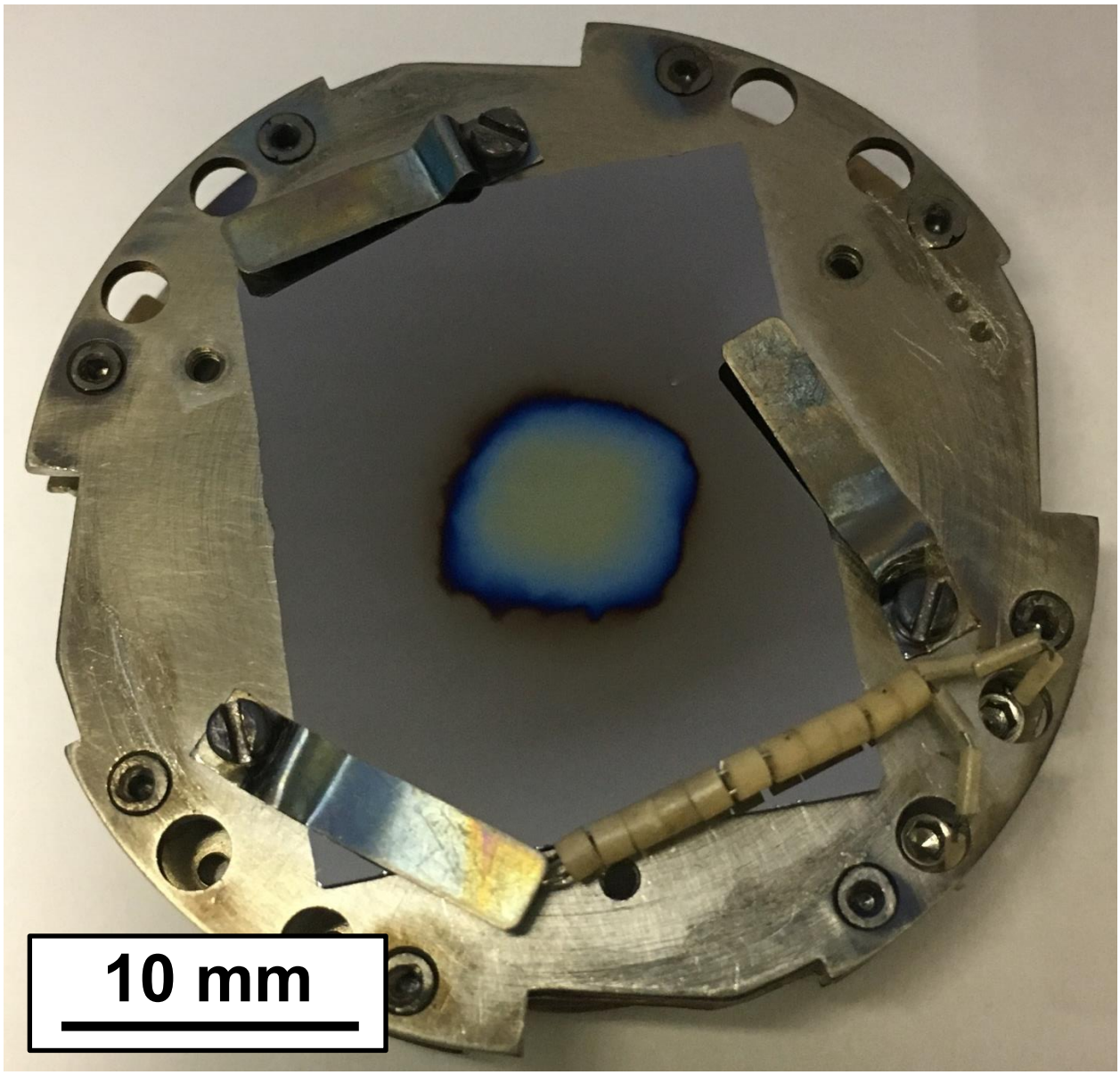

Figure 4.6: Picture of BN film grown at 27 ˚C on a Si(111) substrate.

500 EE-ALD cycles at 27 ˚C on a Si (111) substrate. Self-limiting parameters were used for the deposition with borazine exposures of 7 x 10^{-2} Torr s and electron exposures at 100 eV and 300 μA for 240 s.

Ex situ spectroscopic ellipsometry (SE) was used to acquire a spatial profile of the BN growth spot film thickness. The results of this profile are displayed in Figure 4.7. The film thickness across the deposition area is conformal at approximately 150 nm thick. The spatial profile displayed in Figure 4.7 is of the same sample shown in Figure 4.6. The calculated growth rate is approximately 3.0 Å/cycle. This growth rate is consistent with the growth rates previously observed for BN EE-ALD at 100 eV under self-limiting growth conditions shown in Figures 4.2-4.5.

There is approximately 10 Å in BN film thickness variation across the top of the growth spot observed in Figure 4.7. Additionally, the film thickness drops off very quickly outside the electron flux region. The mesa structure of the growth spot is consistent with hydrogen ESD creating a saturation of “dangling” bond sites on the surface with each cycle. Some BN film is observed outside the electron flux region with a maximum thickness of approximately 50 nm. This growth is attributed to secondary electron scattering and elastic collisions of primary electrons resulting in limited film growth outside the electron flux region.

C. Film Composition

An e*x situ* cross-sectional XPS depth profile of EE-ALD BN films showed a consistent composition throughout the bulk of the film as shown in Figure 4.8. This film was grown at 27 ˚C with 1600 EE-ALD reaction cycles at an electron energy of 100 eV for 60 s and 100 μA. The borazine exposure was approximately 1 x 10^{-4} Torr s. The film was boron-rich BN with 56 at.% B and 40 at.% N. Contamination levels were low, C at 3 at.% and O at 1 at.%, throughout the bulk of the film. A limited and self-terminating surface oxidation on the BN film is evident.

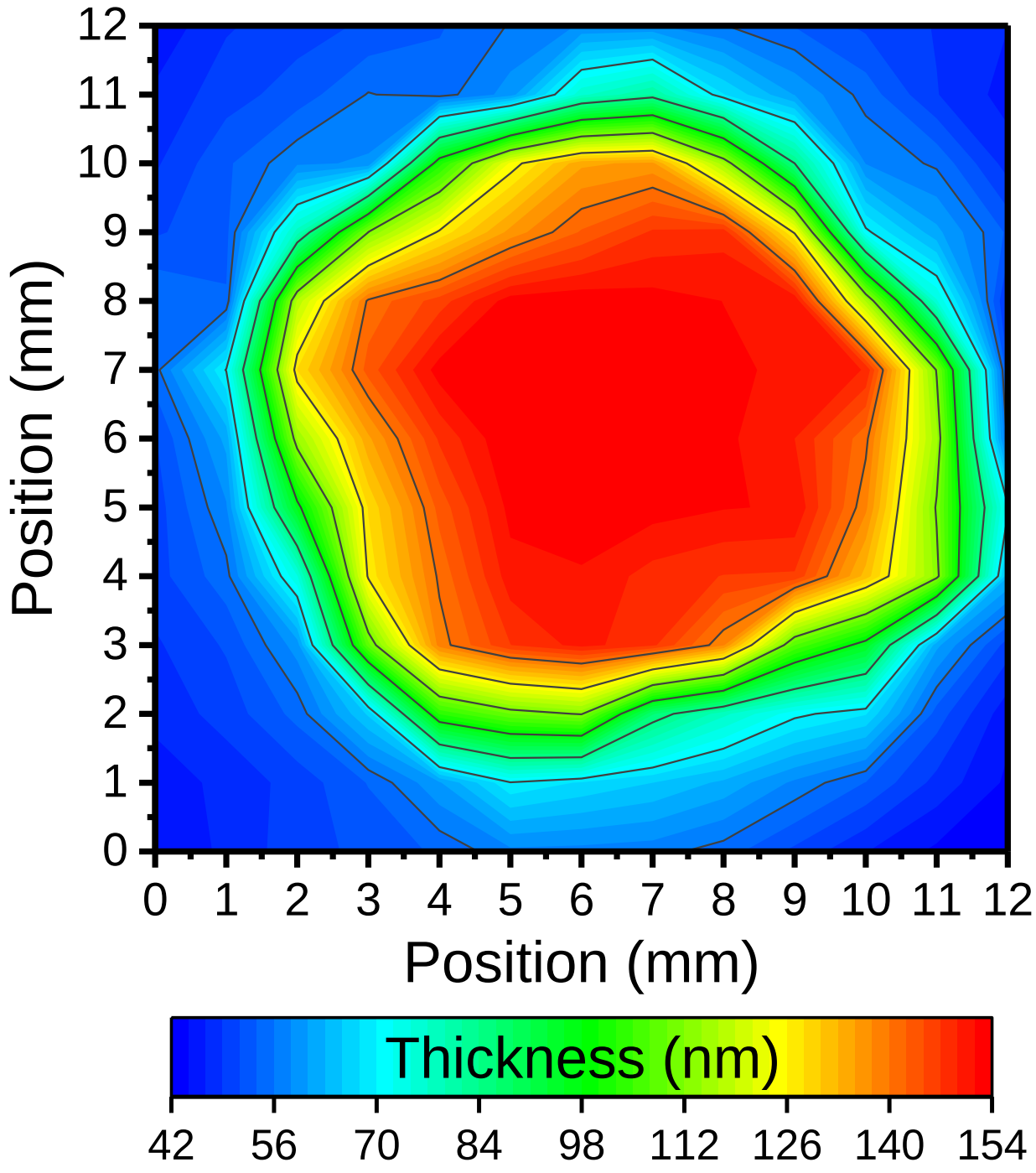

Figure 4.7: Spatial spectroscopic ellipsometry profile of the BN EE-ALD growth spot pictured in Figure 4.6 shows good conformality across the region that was exposed to electron flux.

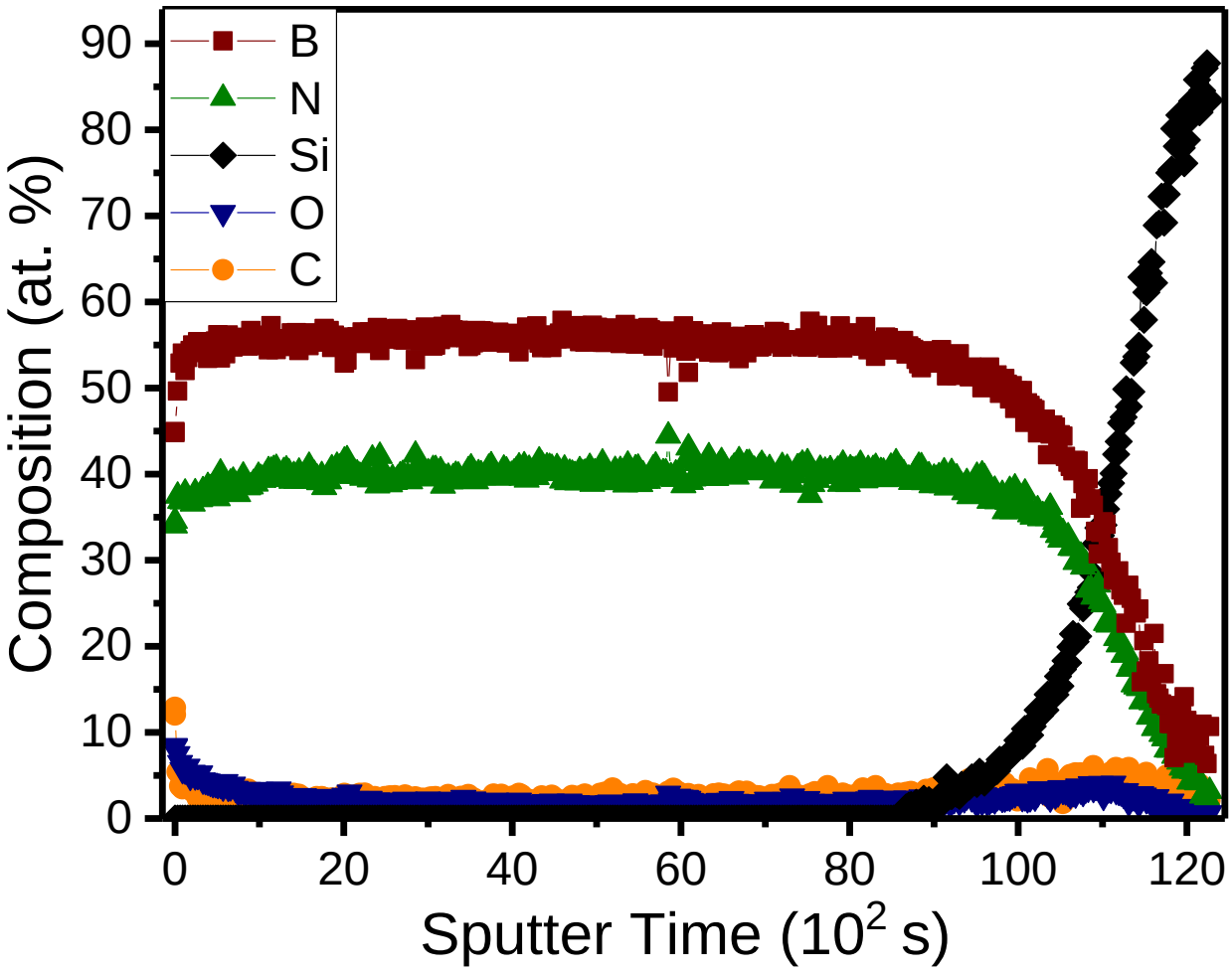

Figure 4.8: XPS depth profile of a BN EE-ALD film grown on Si(111). Film shows consistent composition throughout the bulk with approximately 56 at.% B and 40 at.% N. The film shows approximately 3 at.% C and 1 at.% O contamination throughout bulk.

It is indicative of high levels of film stability as limited degradation occurred even after having been exposed to atmospheric conditions for several hours.

The surface composition of these films was analyzed *in situ* with Auger spectroscopy and the results are in agreement with the XPS results. The film surface was found to be boron-rich with 61 at.% B and 35 at.% N. Surface contamination levels were low with 3 at.% C and 1 at.% O. The slight variation in surface B:N composition from that observed with XPS may be related to molecular orientation of the borazine species as Auger spectroscopy has a penetration depth of 1 nm and is highly surface sensitive. Surface composition was independent of whether the surface had been exposed to borazine or electrons last.

FReS was performed to measure the levels of hydrogen present in these BN EE-ALD films. The hydrogen composition was found to be approximately 7 at.% for a sample that was 4 months old and roughly 11 at.% for a 5 month old sample. Both samples were grown at 27 ˚C with electron energies of 100 eV and under self-limiting reaction conditions.

D. Film Crystallinity and Structure

The crystallinity of EE-ALD BN films was established using grazing incidence x-ray diffraction (GIXRD), micro-Raman spectroscopy, Fourier-transform infrared spectroscopy (FTIR), and high-resolution transmission electron microscopy (HR-TEM). GIXRD of a BN film grown at 100 ˚C with 1000 EE-ALD reaction cycles is show in Figure 4.9a. This film had a thickness of 1170 Å. Growth rates at 100 ˚C were found to be approximately a third the growth rate at 27 ˚C. For reference, Figure 4.9b shows a hexagonal BN XRD powder pattern.[184,185] Only two diffraction peaks are observed in the EE-ALD BN film, which are consistent with BN(002) and BN(004). A slight shift to lower 2θ relative to the hexagonal BN powder pattern is attributed to internal strain in the film. It is possible to calculate the lattice constants to determine the

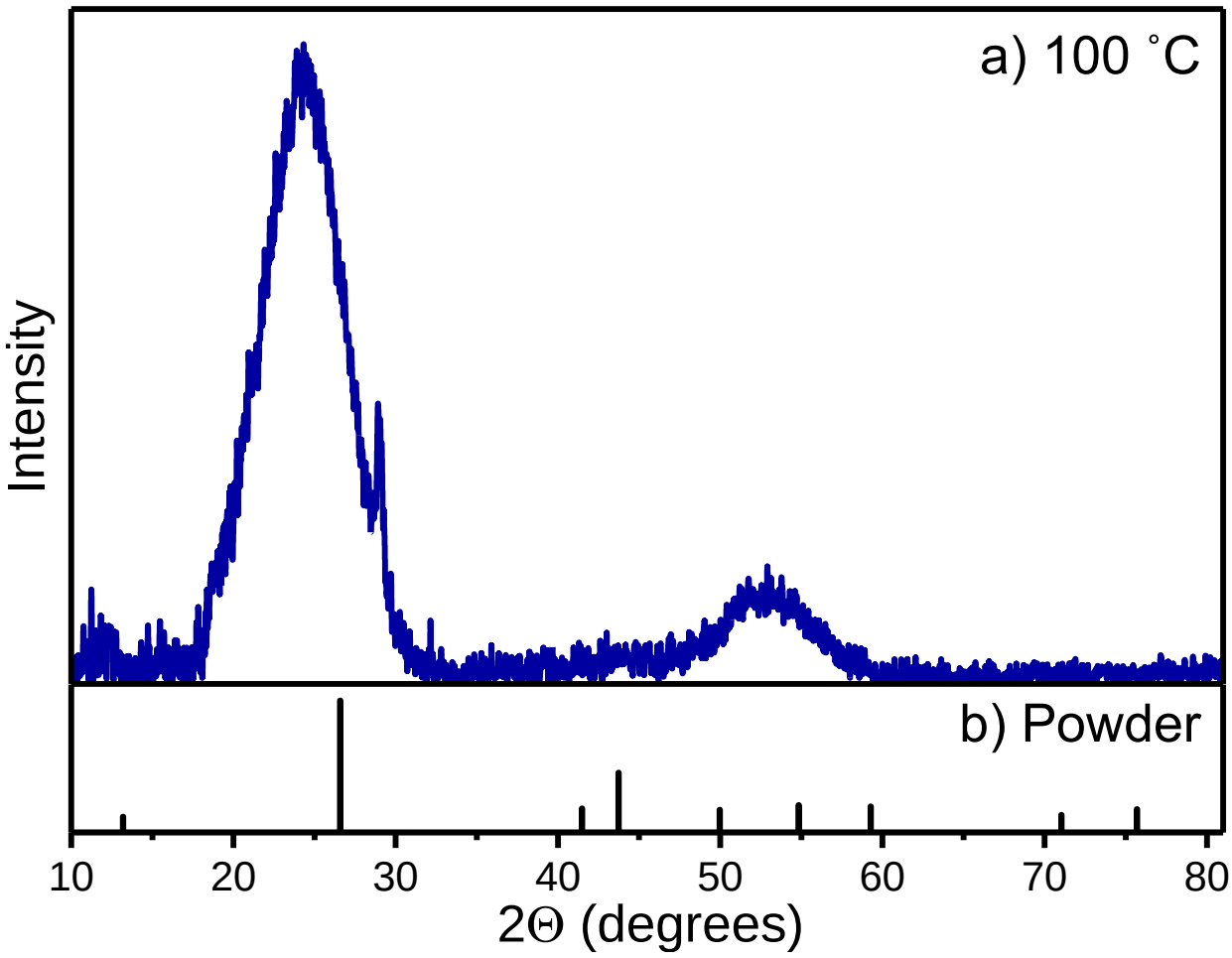

Figure 4.9: a) GIXRD scan of EE-ALD BN film grown at 100 ˚C shows polycrystallinity consistent with hexagonal BN. Crystallite sizes are calculated to be on the order of 1-2 nm. Additionally, due to the presence of only two peaks (002) and (004), it appears that film growth is textured parallel to the substrate surface. b) XRD powder pattern of hexagonal BN for reference.

character of the BN film. Hexagonal BN has an *a* parameter of 2.504 Å and a *c* parameter of 6.658 Å.[186] Turbostratic BN is a variant of hexagonal BN where stacking faults result in a layer displacement by either a random rotation or a shift away from the expected stacking pattern. Based on the percentage of disordered, turbostratic BN present, the *c* lattice parameter can range up to 6.86 Å while no change is observed in the *a* parameter.[186] Ideally, calculation of the lattice constants from GIXRD data would allow for the determination of the purity of hexagonal BN in these EE-ALD films. Unfortunately, due to the shift in peak location attributed to internal strain, calculated lattice constants provide little information about crystallite character. The presence of only the (002) and (004) diffraction peaks is indicative of a textured hexagonal BN film with the c-axis lying perpendicular to the substrate surface. The broadening of diffraction peaks in Figure 4.9a is consistent with fine-grained, polycrystalline BN films. Crystalline size was estimated from the width of the diffraction peaks using the Scherrer formula. Predicted crystallite diameters were 1-2 nm.

Micro-Raman spectroscopy was performed on a BN sample grown at 100 ˚C with 1000 EE-ALD reaction cycles. The film was 1170 Å thick. A small peak was observed at 1372 cm^{-1} that is consistent with the symmetric in-plane stretching of hexagonal BN at 1370 cm^{-1}.[187,188]

Additionally, a BN film grown at 27 ˚C with 2000 EE-ALD cycles was studied with FTIR. The film was 900 Å thick, but was grown under sub-saturating conditions. A broad peak was observed at 1367 cm^{-1}. The IR active peaks for hexagonal BN are found at 1367-1380 cm^{-1} for the in-plane stretch and 780-790 cm^{-1} for out-of-plane bending.[187-190] The FTIR system used only collected down to 1000 cm^{-1}, but the broad 1367 cm^{-1} peak observed was consistent with in-plane stretching for hexagonal BN.

Additionally, the crystallinity of BN EE-ALD films was verified with HR-TEM.[191] Figure 4.10 shows HR-TEM images of a BN film grown at 100 ˚C with 1000 EE-ALD reaction cycles on a Si(111) substrate. HR-TEM visualized the crystallites as small, approximately 1-2 nm in diameter. Though determination is difficult from HR-TEM, the crystallites demonstrated small regions with straight, parallel basal planes consistent with hexagonal BN. However, the crystallite edges and interfacial structures have a wavy basal plane characteristic of turbostratic BN. Despite the presence on a thin ~1 nm amorphous layer between the Si(111) substrate and the bulk of the BN film, the crystallites are textured with the (002) basal plane roughly parallel to the substrate surface in both Figure 4.10a and 4.10b. This observation is consistent with the GIXRD results in Figure 4.9. Previous BN films grown using various ion-bombardment and plasma-enhanced chemical vapor deposition (CVD) techniques as well as physical vapor deposition (PVD) techniques have observed textured, turbostratic BN film growth on Si(001) and Si(111).[188,192-194] However, the turbostratic BN(002) basal plane was observed to be perpendicular to the substrate despite a similar thin amorphous layer.[188,192-194] Conversely, when these same techniques are used in conjunction with a diamond(111) substrate, textured, turbostratic BN with the (002) basal planes parallel to the substrate surface similar to the BN film in Figure 4.10a and 4.10b were observed.[192]

E. Proposed Growth Mechanism

With the EE-ALD BN film growth rates and structure, the growth mechanism for these films can be elucidated. In Figures 4.2-4.5, the maximum growth rates observed are 3.0 - 3.2 Å/cycle. This growth rate is roughly consistent with the 3.3 Å interlayer spacing of hexagonal BN along the c-axis. Further, these films, as deposited, show texturing with the (002) basal plane parallel to the substrate surface in both GIXRD and HR-TEM. It can be concluded that the

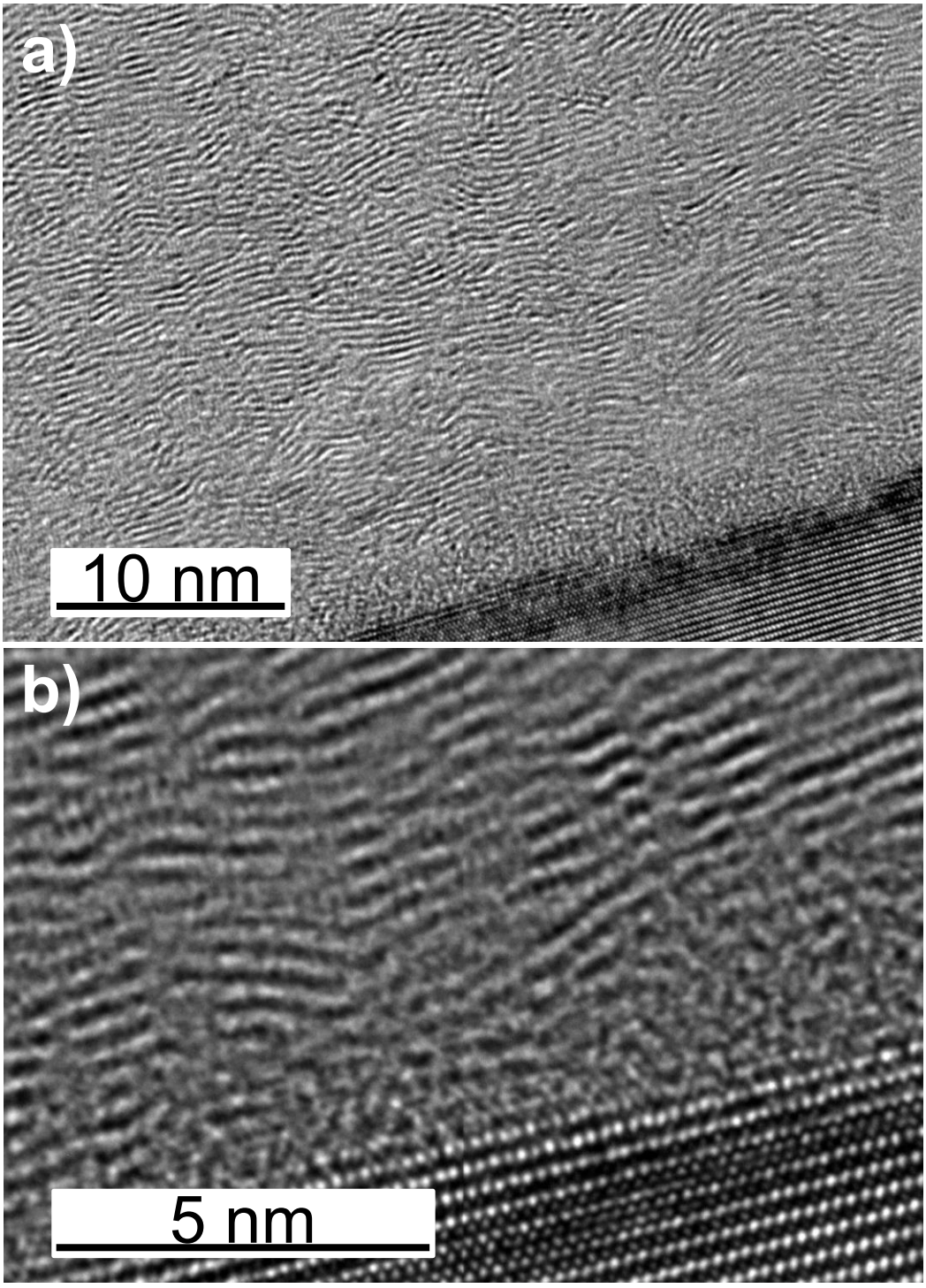

Figure 4.10: HR-TEM images of EE-ALD BN film grown on Si(111) at 100 ˚C. a) Hexagonal and turbostratic BN film shows texturing with the (002) basal plane parallel to the substrate surface. b) Interface of the Si(111) substrate and EE-ALD BN film shows an ~1 nm amorphous BN layer before the formation of the hexagonal and turbostratic BN film.

deposition mechanism for these EE-ALD BN films proceeds through the adsorption of borazine with the ring parallel to the surface as shown in Figure 4.11. Once the surface is irradiated with electrons, the hydrogens attached to borazine are desorbed, leaving highly reactive "dangling" bonds. These "dangling" bonds can then react with neighboring "dangling" bonds to form more sp^2 BN. There is some surface mobility for the adsorbed borazine rings during the electron exposure due to the nature of the van der Waals forces holding them and the energy provided by the incident electrons. After the "dangling" bonds have reacted to form a partial monolayer, more borazine can be introduced and adsorbed. EE-ALD BN is observed to be self-limiting which indicates that the adsorption of a secondary borazine layer on an unreacted, adsorbed borazine layer is unfavorable.

F. Growth on Patterned Substrates

EE-ALD is a line of sight technique that offers selectivity through the directionality of the electron flux on the surface. In the interest of pursuing a bottom-up filling growth technique, EE-ALD of BN was applied to trench structures provided by Applied Materials seen in Figure 4.12. The top of Figure 4.12 is a scanning transmission electron microscopy (STEM) image of BN film growth on the trench structure. It shows a thick layer of BN grown on top of the structure with the indication of a thin BN layer along the sides and at the bottom of the trench. The bottom of Figure 4.12 is an electron energy loss spectroscopy (EELS) image for elemental mapping. The first two panes indicate that a BN film has grown in the trench structure. The film shows a preference for deposition on the surfaces that are closest to normal to the electron source. The thinnest region of the BN film is observed on the trench walls most parallel to the electron source. There are some irregularities in the BN film where preferential growth on the oxide shoulder appears to have shadowed further deposition. The third and fourth panes show the

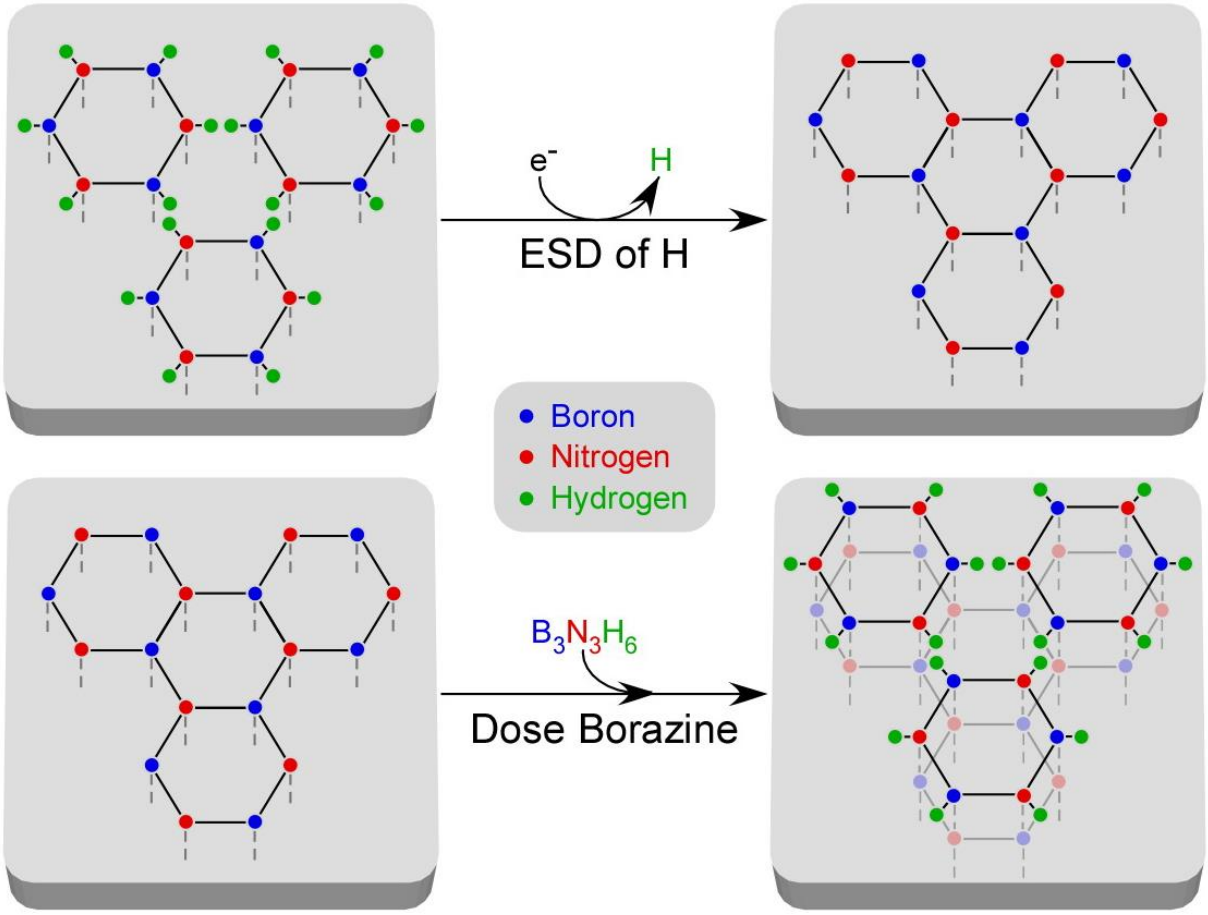

Figure 4.11: Proposed EE-ALD BN growth mechanism.

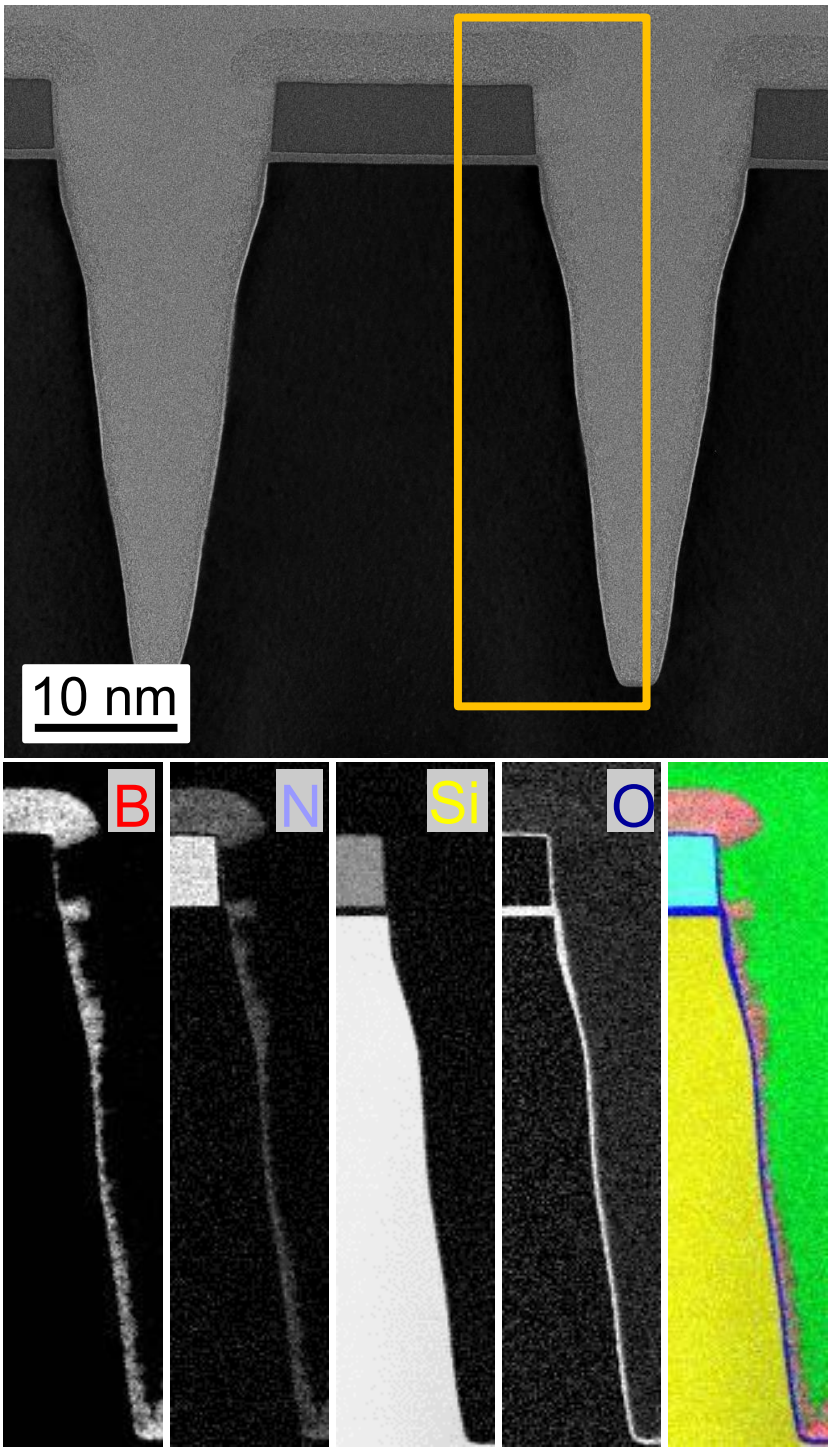

Figure 4.12: EE-ALD BN film growth on trench structure at 27 ˚C. Top pane: STEM image shows thick BN film deposition on top of trench structure with some film deposition on trench sides and bottom. Bottom panes: EELS for B, N, Si, O and a false-colored, combined elemental map. BN films deposited into trench preferentially on the bottom and sloped sides. More vertical regions experienced very little film growth.

trench material and lack of contamination in the BN film. The final pane is a false-colored, composite image of the first four panes. Based on these results, it is expected that with a straight-walled trench structure, preferential bottom-up filling would be observed with this EE-ALD technique. The difficulty with implementing this technique lies in the requirement that electrons penetrate to the bottom of the trench for deposition. This requires that the electron source is aligned with the sample and electrons experience less than a 3˚ deviation in path. In order to deposit the film in Figure 4.12, higher electron energies (400 eV) were used to collimate the electron beam. The film was deposited at 27 ˚C with saturating conditions.

A secondary goal of this research is to probe the ability of the EE-ALD technique with respect to preferential film deposition on the bottom of patterned structures. This "bottom-up" filling technique would add a highly desirable tool for the patterning community.[195] Due to the line of sight growth experienced with the electron flux of EE-ALD, it is expected that EE-ALD films will preferentially deposit on substrate surfaces normal to the electron source.

V. Conclusions

BN films were grown using EE-ALD techniques with sequential exposures of borazine and low energy electrons at 27 ˚C and 100 ˚C. These films are grown through the ESD of hydrogen from the adsorbed borazine surface resulting in "dangling" bond production. The highly reactive "dangling" bonds can then react with each other to form a hexagonal BN layer. Self-limiting growth behavior was observed with respect to borazine exposures, electron exposure time and electron emission current. Additionally, these films grew linearly under a fixed set of conditions. Maximum growth rates of 3.2 Å/cycle were observed at electron energies of 80 – 160 eV. Fitting BN film growth rate versus electron exposure time yielded an ESD hydrogen cross section of $\sigma = 3.9 \times 10^{-14}$ cm^2.

BN films deposited at 100 ˚C were found to be fine-grained and polycrystalline consistent with hexagonal BN by GIXRD, Raman and FTIR. HR-TEM observed textured hexagonal and turbostratic BN with the (002) basal plane parallel to the substrate surface. Estimated crystallite size was 1-2 nm in diameter by GIXRD and HR-TEM. The composition of these films was boron-rich BN (1.3:1) with <3 at.% carbon and oxygen contaminations. Additionally, these films were stable in atmosphere and formed a self-terminating oxide layer.

BN film growth was very conformal across the ~1 cm^2 growth area defined by the electron flux. Additionally, BN film growth on trench structures shows promising results as a bottom-up filling technique. Finally, these EE-ALD BN films can be grown at low temperature and offer a possible avenue for deposition on thermally sensitive substrates.

VI. Acknowledgements

This work was supported by Defense Advanced Research Projects Agency (DARPA). The authors thank Tyler McQuade and Anne Fischer from DARPA for their support and helpful comments. The authors also acknowledge Kenneth Smith and Don David from the University of Colorado Integrated Instrument Development Facility for their help with system design, development and computer interfacing. Additionally, the authors acknowledge Mark Saly from Applied Materials for providing patterned substrates and their analysis, Kathryn Wahl from the Naval Research Laboratory for confirmation GIXRD, Andrew Tomaschke from the University of Colorado Boulder for Raman, Greg Haugstad from the University of Minnesota Characterization Facility for FReS, and Russell Perkins from the University of Colorado Boulder for FTIR.

Chapter 5: Experimental Details

I. Reaction Conditions

Over the course of this work there were significant improvements made to the reactor design allowing for more control and a better understanding of the impacts of reaction parameters. With the initial GaN EE-ALD work, the reactor had very little control over dose pressures and limited *in situ* growth monitoring capabilities. The dosing lines for the trimethylgallium (TMG) and ammonia (NH_3) precursors were attached directly to their respective cylinder regulators resulting in large precursor exposures. These exposures were difficult to quantify as the hot cathode pressure gauge consistently over-pressurized with each precursor dose. Additionally, it was very difficult to optimize reaction parameters with the initial GaN work due to the lack of *in situ* film growth analysis techniques. At this point, the best method for determining optimal reaction conditions was to grow a film under known conditions, analyze it *ex situ*, adjust the reaction parameters and repeat.

System purge times were determined based on the amount of time required for the reaction chamber to return to base pressure after a precursor dose as monitored by the *in situ* residual gas analyzer (RGA) mass spectrometer. It was decided early in the design process that having a current applied across the electron flood gun while a precursor was dosing into the reaction chamber would unnecessarily shorten the lifespan of the filament. Therefore, the electron flood gun was programmed to ramp up its emission current as needed every reaction cycle. A longer system purge was employed to allow for this ramping procedure. Additionally, a small purge was added after the electron flood gun exposure to allow the gun to ramp its current back down during the GaN EE-ALD work. After the discovery of the damaging impacts of disilane on the electron flood gun during the Si EE-ALD work, these post-electron exposure

purge times were extended to allow for filament cooling as well as the reduction in filament current. The impacts of disilane are discussed in detail in section III. While the extended purge times preserved the electron flood gun's lifetime, the increased time allowed for increased levels of "dangling" bond decay and reaction with ambient gases. When precursors were finally introduced, fewer reactive sites were available for film growth. It is expected that this contributed to the low growth rates observed for Si EE-ALD. Purge times were again shortened with the switch to BN EE-ALD as the borazine precursor had fewer adverse interactions with the electron flood gun filament.

GaN EE-ALD precursor dose times needed to be short, ~100 ms, in order to maintain dose pressures in the mTorr range as determined by the hot cathode gauge's programmed over-pressure limits. Prior to beginning the Si EE-ALD work, the reactor's dosing module was redesigned to monitor the fill volume pressure by a capacitance monometer behind the micro-pulse valves. Controlling the fill volume pressures allowed for consistent precursor dosing. The LabVIEW code controlling the dosing system was reprogrammed to account for the new set-up and to automatically maintain the desired fill volume pressure. Dose times were increased for Si and BN EE-ALD in order to obtain precursor dose pressures in the mTorr range.

With the addition of *in situ* film growth monitoring in the form of multi-wavelength ellipsometry, it became more feasible to optimize reaction parameters and study the ALD behavior of EE-ALD film growth. These optimization studies typically consisted of five consecutive reaction cycles under one set of reaction parameters followed by altering a single parameter. The growth rate could be determined by fitting a linear regression to the modeled ellipsometry thickness from the five reaction cycles. Each study varied one parameter until self-

limiting conditions were observed. In this manner, reaction conditions could be fully optimized for a given EE-ALD chemistry.

II. Cleaning Substrate Surfaces

Obtaining a clean substrate surface remained a problem throughout the entirety of this work. Interfacial carbon and oxygen impurities were visible on all x-ray photoelectron spectroscopy (XPS) depth profiles that were collected for these EE-ALD films. The cleaning procedures, both *ex situ* and *in situ,* were designed to remove all material on the substrate surface. Each sample was cleaned *ex situ* in Cyantec Nano-Strip to remove adventitious carbon and other contaminations. After rinsing substrates with deionized water, each sample was cleaned in dilute hydrofluoric acid (HF) (50:1 H_2O:HF) with the intent of removing the oxide layer of the Si(111) and leaving a hydrogen passivated surface.[48,49]

An XPS survey scan of silicon surfaces after this cleaning procedure showed a reduction by approximately half in the surface oxide compared to the untreated samples. The surface carbon appeared relatively unchanged even though the sample was loaded into the XPS directly after treatment. A study of varying exposure times for Nano-Strip and dilute HF cleaning was performed with negligible improvements in reducing contamination levels. Additionally, cleaning with Nano-Strip and piranha acid at 80 ˚C yielded no noticeable change in carbon and oxygen levels.

In situ each substrate was exposed to UV light in both the load lock chamber and the reaction chamber to reduce levels of adsorbed water on the substrate surface. In an attempt to reduce surface contamination levels with another *in situ* process, substrates were exposed to a hydrogen plasma generated on a copper feed-through wire in the reaction chamber backfilled with hydrogen gas to mTorr pressures.[196] Additionally, substrates were exposed to ozone with

UV light and an atomic hydrogen flux from the hydrogen atom beam source (HABS).[196-198] A final cleaning attempt was made by heating the substrate to ~700 °C to thermally desorb any surface species. The interfacial carbon contamination levels showed limited improvement with these treatments when scanned by *in situ* Auger spectroscopy. However, the Auger spectrometer may have been contributing to the carbon contamination as discussed in section IV, D.

It should be noted that these cleaning procedures were attempted for the Si(111) substrate used for the GaN and BN EE-ALD work. Clean Si(111) was desirable for GaN growth as the silicon possessed a decent lattice constant match which might have allowed for the homoepitaxial growth of wurtzite GaN.[199] The Si EE-ALD work was performed on an ALD deposited alumina (Al_2O_3) film on a Si(111) substrate. As the Al_2O_3 film was already amorphous, interfacial contamination had a limited impact on the potential epitaxial growth of the Si EE-ALD films.

III. Electron Source Instability

The electron flood gun failed multiple times during the work focused on Si EE-ALD. Interestingly, no failures occurred during the GaN and the BN EE-ALD work. After the second electron gun filament failure, it was determined that these failures were likely not due to age related degradation. It was thought that a power surge might have overheated the filament resulting in a broken circuit due to melting. However, after the third filament failure occurred, the precursor, disilane, became the main suspect. Upon examination of the filament with scanning electron microscopy (SEM) and energy dispersive spectroscopy (EDS), it became apparent the disilane had adversely affected the electron flood gun filament. The filament was comprised of an iridium disc, employed to increase the surface area for electron generation, attached to a traditional iridium filament structure. The disc was coated with an yttria layer to

reduce the required work function for electron removal from the surface. The impact of the disilane on the electron flood gun was two-fold. First, the disilane acted to reduce the yttria layer to yttrium, thereby increasing the work function for electron removal and increasing the required temperature for the system to function. Second, the disilane proceeded to deposit a CVD silicon film on the hot filament. This silicon layer then diffused into the iridium to form an iridium silicide with a reduced melting point. These two effects compounded to result in quick filament failure through overheating. Figure 5.1 shows a SEM image of the disc after failure of the filament legs. Pitting across the top of the disc surface from the disilane is clearly visible. An EDS elemental map of the surface is provided in Figure 5.2. The oxygen content where the yttria coating should have been is nearly negligible. Additionally, a strong silicon presence can be observed. For the remainder of the Si EE-ALD work, precautions were taken to allow the filament to fully cool before subsequent disilane exposures in order to protect it from further degradation. Finally, the filament material was switched to tungsten with a 5 % rhenium impurity in order to remove the necessity of having an yttria coating layer.

IV. Carbon Contamination

A. Reaction Chamber

During the GaN work, high levels (20 – 30 at.%) of carbon contamination were found throughout the bulk of each EE-ALD film. This contamination was initially attributed to the insufficient removal of the methyl species originating from the trimethylgallium (TMG) precursor used for GaN deposition from the reaction chamber. The system was baked-out and cleaned with hydrogen radicals from the hydrogen atom beam source (HABS) several times in an attempt to clean the reaction chamber.

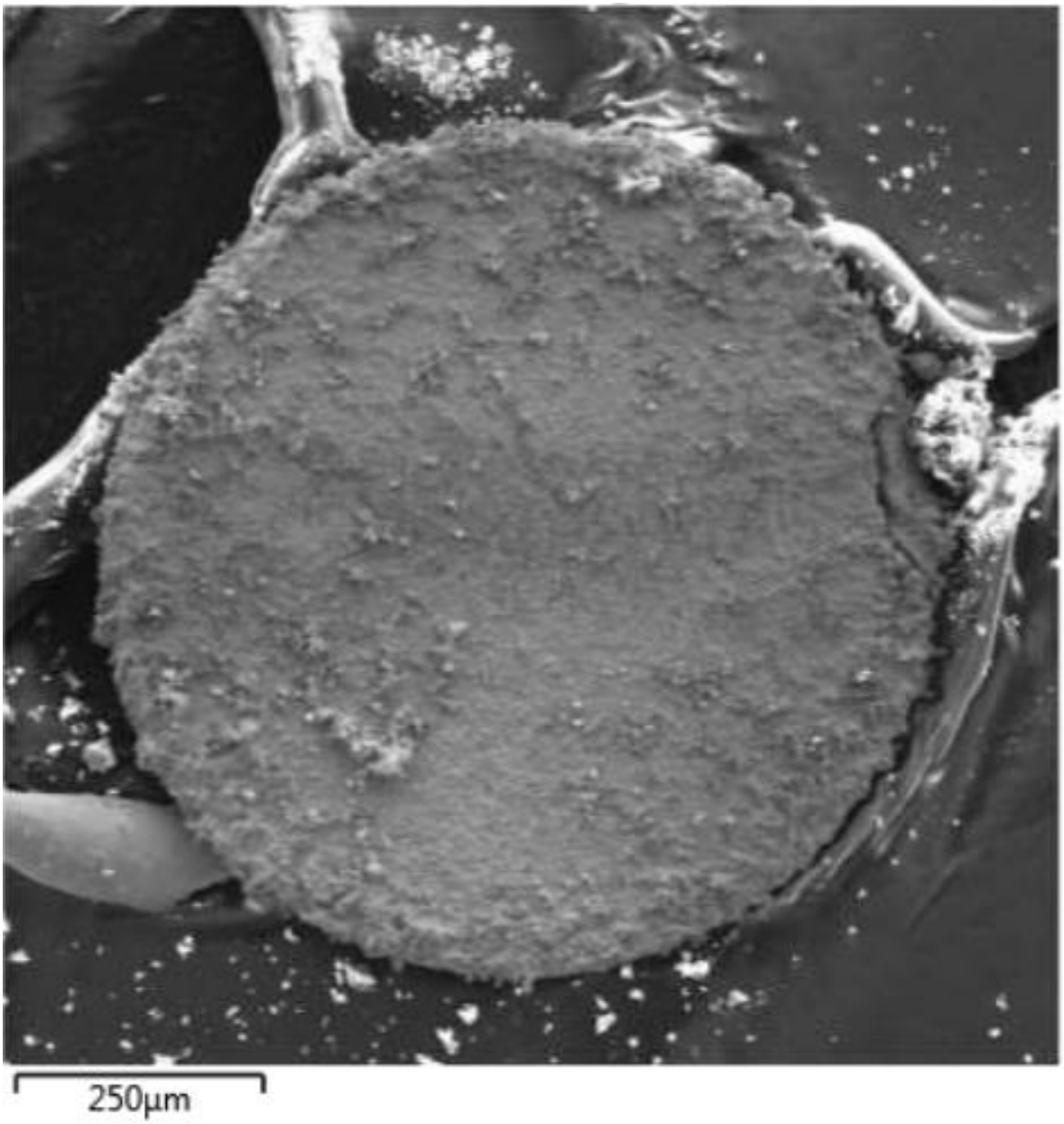

Figure 5.1: SEM image of the electron flood gun disc after filament failure. Pitting and surface morphology changes are evident.

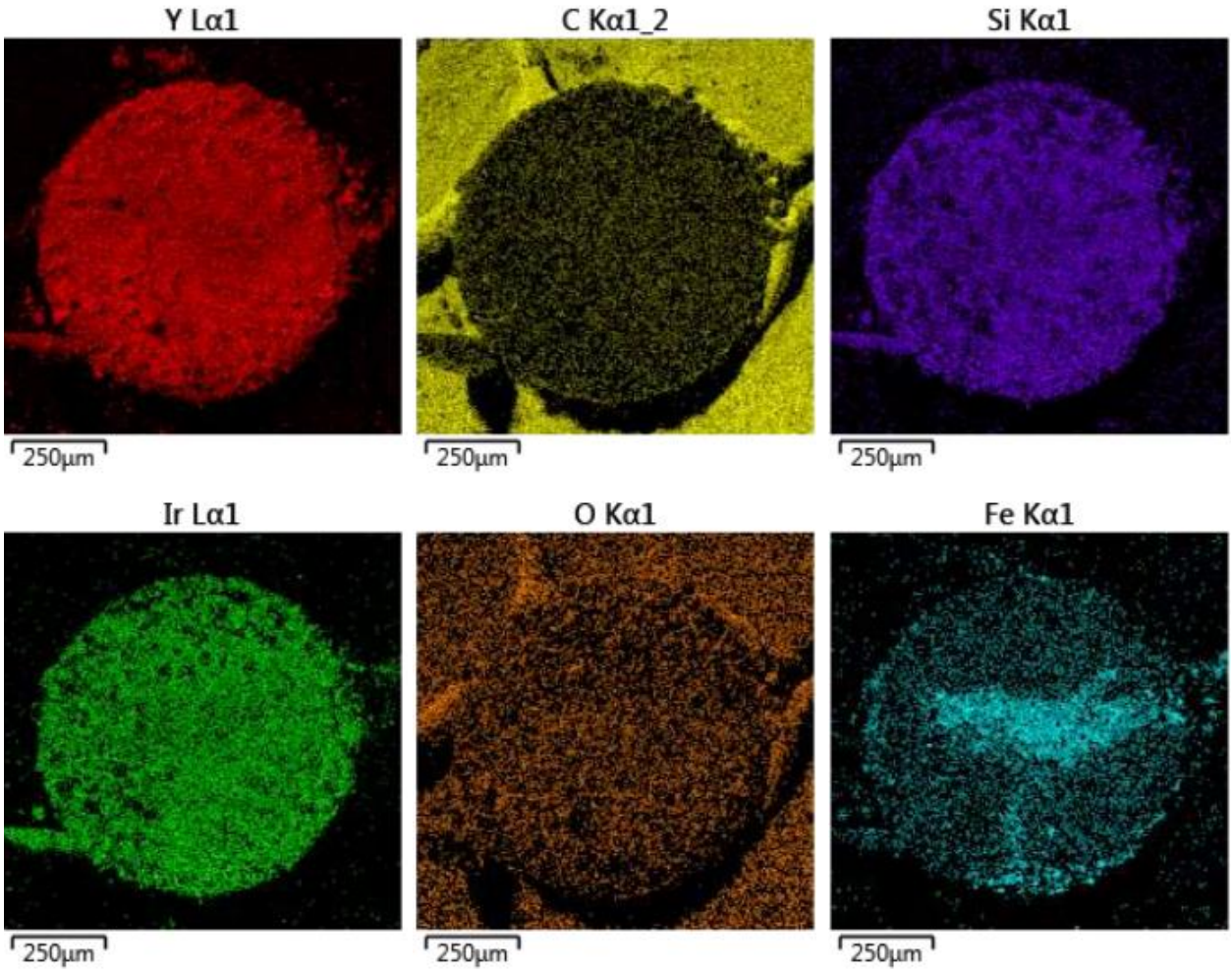

Figure 5.2: EDS elemental mapping of disc shown in Figure 5.1. Images show loss of oxygen from the yttria layer and addition of silicon to the disc face.

In order to reduce the amount of carbon introduced into the reaction chamber, alternative precursors were considered. Theoretical modelling of trimethylgallium (TMG) and triethylgallium (TEG) interactions with an electron flux predicted that the use of the TEG species should result in lower levels of carbon contamination. While counter-intuitive due to the presence of more carbon in the molecule, TEG undergoes a favorable β-hydride elimination reaction resulting in ethylene as a reaction by-product.[200] Meanwhile, TMG dissociatively chemisorbs on the substrate surface with a methane by-product. Ethylene has a much higher vapor pressure and is a less sticky molecule than methane, which should have allowed for more efficient reaction chamber purging. Several experiments were run with the TEG precursor. Unfortunately, the resulting GaN films possessed similar levels of carbon contamination to those found with the TMG species.

After the disappointing results with TEG, further chamber cleaning techniques were employed. An ozone line and generator were installed on the reaction chamber. Ozone has been shown to be highly reactive with carbonaceous species and is frequently used as part of a surface cleaning procedure. A combination of ozone and UV light has been demonstrated to enhance surface cleaning processes.[197,198] This technique was employed for chamber cleaning. Additionally, copper leads were installed on the reaction chamber in order to spark a plasma with the hydrogen gas precursor as hydrogen plasmas have been shown to be efficient for carbon removal.[196] Unfortunately, the carbon levels in the main reaction chamber as monitored by the residual gas analyzer (RGA) remained high.

B. Hydrogen Atom Beam Source

The HABS had been positioned in the reaction chamber at 55 ˚ from surface normal to the reaction substrate and located several inches away from the substrate surface. Due to the carbon contamination problems, these parameters were examined and found to produce a lower

atomic hydrogen flux than anticipated. This lower atomic hydrogen flux resulted in the insufficient removal of methyl species from the film surface and contributed to the films' carbon contamination problems. Additionally, it was determined, through the disassembly and cleaning of the HABS, that the tungsten capillary in which molecular hydrogen was cracked into atomic hydrogen had become contaminated with carbonaceous species. This discovery meant that with every atomic hydrogen exposure, the carbonaceous material on the HABS capillary had the potential to desorb as a radical and react with the film surface. The carbon contamination on the HABS could have been avoided with the use of a curtain gas to prevent the backflow of precursor into the HABS system. During the reactor design stage it was assumed that separation of the HABS from the reaction chamber by a gate valve when not in use would be sufficient. Unfortunately, enough residual precursor remained in the reaction chamber to contaminate the HABS even with the gate valve precaution. Prior to further research, the HABS was cleaned and moved to the analysis chamber to be used only for initial surface cleaning. Additionally, no carbon containing precursors were employed with the system for the Si and BN EE-ALD work.

C. Wire Insulation

Unfortunately, the carbon contamination problems persisted into the Si EE-ALD portion of this work despite continued chamber cleaning, use of non-carbon based precursors and removal of the HABS from the reaction chamber. Eventually, it was found that the electron flood gun and magnetically coupled transfer arm feed-through wires had been insulated with polytetrafluoroethylene (PTFE) sheaths. As the electron flood gun was cycled, the PTFE had the potential to off-gas carbonaceous materials that could contaminate the reaction chamber and film growth. These polymers were removed and replaced with ceramic insulators. With this alteration, and continued chamber baking and cleaning, the background carbon signal was finally reduced to reasonable levels as measured by RGA analysis.

D. Auger Spectrometer

Despite the reaction chamber having low levels of carbon present, Auger spectroscopy analysis of the Si EE-ALD films still showed high levels of carbon present in the films. It was found that samples left overnight in the reaction chamber experienced very little change in surface carbon levels, which was consistent with a clean reaction chamber. When multiple Auger spectroscopy scans were performed consecutively on a film surface, carbon levels were observed to increase dramatically. It was concluded that the Auger spectrometer was actually sputtering carbon onto the film surface along with the high energy electrons used for film analysis. Unfortunately, the ambient carbon contamination in the reaction chamber had resulted in the contamination of the Auger spectrometer. After several degassing cycles were unsuccessful in altering this situation, the spectrometer was returned to RBD Instruments for a rebuild and upgrade.

Upon installation of the updated Auger spectrometer on the analysis chamber, it was discovered that there had been some damage to the alignment of the new system during shipping. While the spectrometer was still functional, the observed elastic peak for the generated electrons was broad and misshaped resulting in a poor signal to noise ratio for all Auger spectroscopy scans. It was still possible to collect spectra and determine relative atomic concentrations; however, none of the data collected by this spectrometer was viable for publication as a figure. Despite the Auger spectrometer system representing an ongoing problem, it was useful for the surface analysis of the BN EE-ALD film work.

Chapter 6: Future Directions

I. Bottom-Up Filling

The continually decreasing dimensions of semiconductor devices has recently driven the need for a large-scale overhaul of existing semiconductor designs. Three-dimensional (3D) integration has emerged as one of the most popular designs to handle the decreasing size of integrated circuits.[201] Vertically stacked, integrated circuits provide greater connectivity and occupy less space than the same number of circuits arrayed in solely two dimensions. However, 3D integration requires increased levels of complexity when it comes to processing these devices. The vertical interconnects of these systems present a new design problem.

Through Silicon Via (TSV) technology represents the shortest vertical interconnects to bridge the vertical integration gaps of these 3D systems.[202,203] A TSV is a high performance interconnect in the form of a manufactured pore that can pass entirely through a silicon wafer. These TSVs serve as a superior alternative to traditional wire-bond and flip-chip circuits.[203] The TSVs are filled, typically with copper, to form a built-in wire interconnect within the integrated circuit. However, filling the TSV presents difficulties in that there cannot be any void space remaining in the TSV from the fill technique and the fill material must be of high quality to avoid electric losses and heating of the circuit.[202,204]

The bottom-up filling method is currently a hot topic in the semiconductor industry as it represents a significant improvement potential for the quality and rate of TSV filling.[205,206] Bottom-up filling is a process through which a film or material is deposited selectively at the bottom of the TSV or pore structure. From there, the film will preferentially grow upward experiencing little to no reaction with the sidewalls of the structure. One common problem with non-bottom-up fill techniques, such as traditional ALD, is that the film on the sidewalls will

grow quickly enough to result in the TSV or pore being pinched off before the entire bottom of the structure is filled. This results in a void space where no material or film is located. Void spaces cause large decreases in conductivity and material defects that degrade the interconnect quality.

This EE-ALD work has shown some initial promising results with regard to application as a bottom-up filling technique. By its nature, EE-ALD is a line-of-sight, directional technique that is dependent on a flux of electrons across the surface for deposition to occur. Initial trench deposition studies have shown a preference for deposition on surfaces normal to the incoming electron flux. Based on these results, it may be possible to optimize this chemistry for bottom-up fill applications. However, there is still much work to be done. The first major hurdle for this transition is the requirement for high levels of collimation within the electron beam to achieve a large enough electron flux across the bottom of trench structures. Additionally, electron charging in these structures during EE-ALD needs to be studied, as a build-up of negative charge on the surface will result in the repulsion of further electrons and the termination of film growth.

II. Deposit-Etch Technique

A recurring difficulty for modern advanced electronic materials lies in obtaining the necessary ultra-thin, conformal films, sometimes only a single monolayer thick, with high material quality. Current ALD techniques are unable to produce single monolayer films of many of the desired materials and for some of these materials atomic level control is not even possible. Typically, this is a result of poor nucleation in the initial stages of film growth.

Three main growth modes observed for ALD techniques: Frank-van der Merwe growth, Volmer-Weber growth and Stranski-Krastanov growth. Traditional ALD processes for low surface energy materials, such as Al_2O_3, deposit films through a Frank-van de Merwe growth

style where adatoms will preferentially adsorb on the surface rather than each other to form a two-dimensional (2D) monolayer.[207,208] Films grown in this fashion will possess standard ALD conformality. However, it is possible to deposit ALD films in a Volmer-Weber growth pattern. The characteristic of this film growth is the initial formation of three-dimensional (3D) islands from individual nucleation sites that will eventually coalesce into a single film if large enough islands are formed.[208-210] Typically, this growth mechanism occurs due to the high surface energy of the deposited material resulting in preferential adatom-adatom interactions such as observed with noble metal film growth.[211] It is also possible to observe a hybrid growth pattern called Stranski-Krastanov growth that is characterized by initial Frank-van der Merwe 2D growth that transitions into the 3D island type growth of Volmer-Weber.[212] This is the least common ALD film growth type. The control desired for advanced electronic materials is most readily obtained when films are grown in a Frank-van der Merwe mode. However, for advanced electronic desired materials, typically transition metal dichalcogenides and metallic multilayer film stacks, the majority of growth occurs through a Volmer-Weber mechanism resulting in poor nucleation and non-continuous films.

The elevated reaction temperatures required for traditional ALD of the desired materials allow for more adatom mobility across surfaces and coalescence into islands. Additionally, many materials of interest for advanced electronic applications have a high surface energy that results in preferential Volmer-Weber growth. In order to combat this Volmer-Weber growth pattern and improve material properties at the monolayer level, it is proposed that a deposit-etch process can be implemented. Initial film growth will be accomplished with EE-ALD. The applicable chemistry will have to be developed, but it should present limited difficulty so long as a hydrogen or halide precursor with a large ESD cross section is employed. The low temperatures

required for this technique will reduce the surface mobility of adatom species resulting from excess thermal energy and result in a more Frank-van der Merwe type growth. Once a continuous film has been achieved via EE-ALD, the film can be etched back by a thermal atomic layer etching (ALE) process until the desired film thickness has been reached. ALE has been shown to have Ångstrom-level control like its growth counterpart, be highly selective and have the ability to smooth a rough film as the etch progresses.[213-215] The combination of EE-ALD and ALE should lead to the deposition of films with high material quality and a tightly controlled thickness that can reach to the monolayer level. Films grown in this manner should find many applications as modern advanced electronic materials.

References

(1) Reprinted with permission from Ramsier, R. D.; Yates, J. T. Electron-stimulated Desorption: Principles and Applications. Surf. Sci. Rep. 1991, 12 (6-8), 133. Copyright 1991 Elsevier.

(2) Reprinted with permission from George, S. M. Atomic Layer Deposition: An Overview. Chem. Rev. 2010, 110, 111. Copyright 2010 American Chemical Society.

(3) Reprinted with permission from Ritala, M.; Leskelä, M.; Dekker, J.-P.; Mutsaers, C.; Soininen, P. J.; Skarp, J. Perfectly Conformal TiN an Al2O3 Films Deposited by Atomic Layer Deposition. Chem. Vap. Deposition 1999, 5 (1), 7. Copyright 1999 John Wiley and Sons.

(4) George, S. M. Atomic Layer Deposition: An Overview. *Chem. Rev.* **2010,** *110*, 111.

(5) Lee, Y. C.; Yersak, A. S.; Spencer, J. A.; Groner, M. D. Atmospheric Pressure Spatial Atomic Layer Deposition Web Coating with in situ Monitoring of Film Thickness. *J. Vac. Sci. Technol., A* **2014,** *32* (1).

(6) Jur, J. S.; Parsons, G. N. Atomic Layer Deposition of Al_2O_{-3} and ZnO at Atmospheric Pressure in a Flow Tube Reactor. *ACS Appl. Mater. Interfaces* **2011,** *3* (2), 299.

(7) Miikkulainen, V.; Leskelä, M.; Ritala, M.; Puurunen, R. L. Crystallinity of Inorganic Films Grown by Atomic Layer Deposition: Overview and General Trends. *J. Appl. Phys.* **2013,** *113*.

(8) Parsons, G. N.; Elam, J. W.; George, S. M.; Haukka, S.; Jeon, H.; Kessels, W. M. M.; Leskelä, M.; Poodt, P.; Ritala, M.; Rossnagel, S. M. History of Atomic Layer Deposition and Its Relationship with the American Vacuum Society. *J. Vac. Sci. Technol., A* **2013,** *31* (5), 050818.

(9) Puurunen, R. L. A Short History of Atomic Layer Deposition: Tuomo Suntola's Atomic Layer Epitaxy. *Chem. Vap. Deposition* **2014,** *20* (10), 332.

(10) Kim, H. Atomic Layer Deposition of Metal and Nitride Thin Films: Current Research Efforts and Applications for Semiconductor Device Processing. *J. Vac. Sci. Technol., B* **2003,** *21* (6), 2231.

(11) George, S. M.; Yoon, B.; Dameron, A. A. Surface Chemistry for Molecular Layer Deposition of Organic and Hybrid Organic-Inorganic Polymers. *Acc. Chem. Res.* **2009,** *42* (4), 498.

(12) Mohseni, H.; Scharf, T. W. Atomic Layer Deposition of $ZnO/Al_2O_3/ZrO_2$ Nanolaminates for Improved Thermal and Wear Resistance in Carbon-Carbon Composites. *J. Vac. Sci. Technol., A* **2011,** *30* (1).

(13) Schwartzberg, A. M.; Olynick, D. Complex Materials by Atomic Layer Deposition. *Adv. Mater.* **2015,** *27* (38), 5778.

(14) Wilson, C. A.; Grubbs, R. K.; George, S. M. Nucleation and Growth during Al_2O_3 Atomic Layer Deposition on Polymers. *Chem. Mater.* **2005,** *17* (23), 5625.

(15) Xiao, X.; Cao, G.; Chen, F.; Tang, Y.; Liu, X.; Xu, W. Durable Superhydrophobic Wool Fabrics Coatings with Nanoscale Al_2O_3 Layer by Atomic Layer Deposition. *Appl. Surf. Sci.* **2015,** *349*, 876.

(16) King, D. M.; Spencer, J. A.; Liang, X.; Hakim, L. F.; Weimer, A. W. Atomic Layer Deposition on Particles using a Fluidized Bed Reactor with In Situ Mass Spectrometry. *Surf. Coat. Technol.* **2007,** *201* (22-23), 9163.

(17) Farmer, D. B.; Gordon, R. G. Atomic Layer Deposition on Suspended Single-Walled Carbon Nanotubes via Gas-Phase Noncovalent Functionalization. *Nano Lett.* **2006,** *6* (4), 699.

(18) Niinisto, J.; Ritala, M. Industrial Applications of Atomic Layer Deposition. *ECS Trans.* **2009,** *25* (8), 641.

(19) Jung, Y. S.; Cavanagh, A. S.; Gedvilas, L.; Widjonarko, N. E.; Scott, I. D.; Lee, S.-H.; Kim, G.-H.; George, S. M.; Dillon, A. C. Improved Functionality of Lithium-Ion Batteries Enabled by Atomic Layer Depositionon the Porous Microstructure of Polymer Separators and Coating Electrodes. *Adv. Energy Mater.* **2012,** *2* (8), 1022.

(20) Hong, K.; Cho, M.; Kim, S. O. Atomic Layer Deposition Encapsulated Activiated Carbon Electrodes for High Voltage Stable Super Capacitors. *ACS Appl. Mater. Interfaces* **2015,** *7* (3), 1899.

(21) Cheng, N.; Shao, Y.; Liu, J.; Sun, X. Electrocatalysts by Atomic Layer Deposition for Fuel Cell Applications. *Nano Energy* **2016,** *29*, 220.

(22) Niu, W.; Li, X.; Karuturi, S. K.; Fam, D. W.; Fan, H.; Shrestha, S.; Wong, L. H.; Tok, A. I. Y. Applications of Atomic Layer Deposition in Solar Cells. *Nanotechnology* **2015,** *26*.

(23) Käärinänen, T. O.; Kemell, M.; Vehkamäki, M.; Käärinänen, M. L.; Correia, A.; Santos, H. A.; Bimbo, L. M.; Hirvanen, J.; Hoppu, P.; George, S. M.et al. Surface Modification of Acetaminophen Particles by Atomic Layer Deposition. *Int. J. Pharm.* **2017,** *525* (1), 160.

(24) Devlin-Mullin, A.; Todd, N. M.; Golrokhi, Z.; Geng, H.; Konerding, M. A.; Ternan, N. G.; Hunt, J. A.; Potter, R. J.; Sutcliffe, C.; Jones, E.et al. Atomic Layer Deposition of a Silver Nanolayer on Advanced Titanium Orthopedic Implants Inhibits Bacterial Colonization and Supports Vascularized de Novo Bone Ingrowth. *Adv. Healthc. Mater.* **2017,** *6* (11).

(25) Neumayer, D. A.; Ekerdt, J. G. Growth of Group III Nitrides. A Review of Precursors and Techniques. *Chem. Mater.* **1996,** *8*, 9.

(26) Ahmed, M.; Ruffing, K.; Potter, D. I. Surface Roughening during Elevated Temperature Implantation of Nickel. *Mater. Sci. Eng.* **1987,** *90*, 37.

(27) Edmonds, M.; Sardashti, K.; Wolf, S.; Chagarov, E.; Clemons, M.; Kent, T.; Park, J. H.; Tang, K.; McIntyre, P. C.; Yoshida, N.et al. Low Temperature Thermal ALD of a SiN_x Interfacial Diffusion Barrier and Interface Passivation Layer on Si_xGe_{1-x}(001) and Si_xGe_{1-x}(110). *J. Chem. Phys.* **2017,** *146*.

(28) Profijit, H. B.; Potts, S. E.; van de Sanden, M. C. M.; Kessels, W. M. M. Plasma-Assisted Atomic Layer Deposition: Basics, Opportunities, and Challenges. *J. Vac. Sci. Technol., A* **2011,** *29* (5).

(29) Chalker, P. R. Photochemical Atomic Layer Deposition and Etching. *Surf. Coat. Technol.* **2016,** *291*, 258.

(30) Lemke, B. P.; Haneman, D. Dangling Bonds on Silicon. *Phys. Rev. B* **1978,** *17* (4).

(31) Redhead, P. A. Interactions of Slow Electrons with Chemisorbed Oxygen. *Can. J. Phys.* **1964,** *42* (5), 886.

(32) Menzel, D.; Gomer, R. Desoption from Metal Surfaces by Low-Energy Electrons. *J. Chem. Phys.* **1964,** *41* (11), 3311.

(33) Feibelman, P. J.; Knotek, M. L. Reinterpretation of Electron-Stimulated Desorption Data from Chemisorption Systems. *Phys. Rev. B* **1978,** *18* (12), 6531.

(34) Halliday, D. *Fundamentals of Physics*; 6th ed.; Wiley: New York, 2001.

(35) Johnson, F. S. Lunar Atmosphere. *Rev. Geophys.* **1971,** *9* (3), 813.

(36) Goeden, C.; Dollinger, G. Electron Stimulated Hydrogen Desorption from Diamond Surfaces and its Influence on the Low Pressure Synthesis of Diamond. *Appl. Phys. Lett.* **2002,** *81* (26), 5027.

(37) Suzuki, S.; Fukui, K.; Onishi, H.; Iwasawa, Y. Hydrogen Adatoms on TiO_2(110)-(1x1) Characterized by Scanning Tunneling Microscopy and Electron Stimulated Desorption. *Phys. Rev. Lett.* **2000,** *84* (10), 2156.

(38) Trenhaile, B. R.; Antonov, V. N.; Xu, G. J.; Agrawal, A.; Signor, A. W.; Butera, R. E.; Nakayama, K. S.; Weaver, J. H. Phonon-Activated Electron Stimulated Desorption of Halogens from Si(100)-(2x1). *Phys. Rev. B* **2006,** *73* (12), 125318.

(39) Adapted with permission from Sprenger, J. K.; Cavanagh, A. S.; Sun, H.; Wahl, K. J.; Roshko, A.; George, S. M. Electron Enhanced Growth of Crystalline Gallium Nitride Thin Films at Room Temperature and 100 °C Using Sequential Surface Reactions. Chem. Mater. 2016, 28 (15), 5282. Copyright (2016) American Chemical Society.

(40) Denbaars, S. P. Gallium Nitride Based Materials for Blue to Ultraviolet Optoelectronics Devices. *Proc. IEEE* **1997,** *85* (11), 1740.

(41) Zhu, D.; Wallis, D. J.; Humphreys, C. J. Prospects of III-Nitride Optoelectronics Grown on Si. *Rep. Prog. Phys.* **2013,** *76* (10), 106501.

(42) Mishra, U. K.; Shen, L.; Kazior, T. E.; Wu, Y.-F. GaN-Based RF Power Devices and Amplifiers. *Proc. IEEE* **2008,** *96* (2), 287.

(43) Pearton, S. J.; Ren, F. GaN Electronics. *Adv. Mater.* **2000,** *12* (21), 1571.

(44) Denis, A.; Goglio, G.; Demazeau, G. Gallium Nitride Bulk Crystal Growth Processes: A Review. *Mat. Sci. Eng. R* **2006,** *50* (6), 167.

(45) Gibart, P. Metal Organic Vapour Phase Epitaxy of GaN and Lateral Overgrowth. *Rep. Prog. Phys.* **2004,** *67* (5), 667.

(46) Khan, M. A.; Kuznia, J. N.; Vanhove, J. M.; Olson, D. T.; Krishnankutty, S.; Kolbas, R. M. Growth of High Optical and Electrical Quality GaN Layers Using Low Pressure Metalorganic Chemical Vapor Deposition. *Appl. Phys. Lett.* **1991,** *58* (5), 526.

(47) Neumayer, D. A.; Ekerdt, J. G. Growth of Group III Nitrides. A Review of Precursors and Techniques. *Chem. Mater.* **1996,** *8* (1), 9.

(48) Molnar, R. J.; Moustakas, T. D. Growth of Gallium Nitride by Electron Cyclotron Resonance Plasma-Assisted Molecular Beam Epitaxy - The Role of Charged Species. *J. Appl. Phys.* **1994,** *76* (8), 4587.

(49) Lei, T.; Moustakas, T. D.; Graham, R. J.; He, Y.; Berkowitz, S. J. Epitaxial Growth and Characterization of Zincblende Gallium Nitride on (001) Silicon. *J. Appl. Phys.* **1992,** *71* (10), 4933.

(50) George, S. M. Atomic Layer Deposition: An Overview. *Chem. Rev.* **2010,** *110* (1), 111.

(51) Huang, S. C.; Wang, H. Y.; Hsu, C. J.; Gong, J. R.; Chiang, C. I.; Tu, S. L.; Chang, H. Growth of Wurtzite GaN on (001)GaAs Substrates at Low Temperature by Atomic Layer Epitaxy. *J. Mater. Sci. Lett.* **1998,** *17* (15), 1281.

(52) Karam, N. H.; Parodos, T.; Colter, P.; McNulty, D.; Rowland, W.; Schetzina, J.; Elmasry, N.; Bedair, S. M. Growth of Device-Quality GaN at 550 Degrees C by Atomic Layer Epitaxy. *Appl. Phys. Lett.* **1995,** *67* (1), 94.

(53) Khan, M. A.; Skogman, R. A.; Vanhove, J. M.; Olson, D. T.; Kuznia, J. N. Atomic Layer Epitaxy of GaN over Sapphire Using Switchedd Metalorganic Chemical Vapor Deposition. *Appl. Phys. Lett.* **1992,** *60* (11), 1366.

(54) Sumakeris, J.; Sitar, Z.; Aileytrent, K. S.; More, K. L.; Davis, R. F. Layer-by-Layer Epitaxial Growth of GaN at Low Temperatures. *Thin Solid Films* **1993,** *225* (1-2), 244.

(55) Koukitu, A.; Kumagai, Y.; Taki, T.; Seki, H. Halogen Transport Atomic Layer Epitaxy of Cubic GaN Monitored by in situ Gravimetric Method. *Jpn. J. Appl. Phys., Part 1* **1999,** *38* (9A), 4980.

(56) Kumagai, Y.; Mayumi, M.; Koukitu, A.; Seki, H. In situ Gravimetric Monitoring of Halogen Transport Atomic Layer Epitaxy of Cubic GaN. *Appl. Surf. Sci.* **2000,** *159*, 427.

(57) Kim, O. H.; Kim, D.; Anderson, T. Atomic Layer Deposition of GaN Using $GaCl_3$ and NH_3. *J. Vac. Sci. Technol. A* **2009,** *27* (4), 923.

(58) Tsuchiya, H.; Akamatsu, M.; Ishida, M.; Hasegawa, F. Layer-by-Layer growth of GaN on GaAs Substrates by Alternate Supply of $GaCl_3$ and NH_3. *Jpn. J. Appl. Phys., Part 2* **1996,** *35* (6B), L748.

(59) Ozgit, C.; Donmez, I.; Alevli, M.; Biyikli, N. Atomic Layer Deposition of GaN at Low Temperatures. *J. Vac. Sci. Technol. A* **2012,** *30* (1), 01a124.

(60) Ozgit-Akgun, C.; Goldenberg, E.; Okyay, A. K.; Biyikli, N. Hollow Cathode Plasma-Assisted Atomic Layer Deposition of Crystalline AlN, GaN and $Al_xGa_{1-x}N$ Thin Films at Low Temperatures. *J. Mater. Chem. C* **2014,** *2* (12), 2123.

(61) Madey, T. E.; Yates, J. T. Electron Stimulated Desorption as a Tool for Studies of Chemisorption - Review. *J. Vac. Sci. Technol.* **1971,** *8* (4), 525.

(62) Ramsier, R. D.; Yates, J. T. Electron Stimulated Desorption - Principles and Applications. *Surf. Sci. Rep.* **1991,** *12* (6-8), 243.

(63) Bellitto, V. J.; Thoms, B. D.; Koleske, D. D.; Wickenden, A. E.; Henry, R. L. Efficient Electron Stimulated Desorption of Hydrogen from GaN(0001). *Phys. Rev. B* **1999,** *60* (7), 4821.

(64) Bermudez, V. M.; Koleske, D. D.; Wickenden, A. E. The Dependence of the Structure and Electronic Properties of Wurtzite GaN Surfaces on the Method of Preparation. *Appl. Surf. Sci.* **1998,** *126* (1-2), 69.

(65) Adams, D. P.; Mayer, T. M.; Swartzentruber, B. S. Nanometer-Scale Lithography on Si(001) Uusing Adsorbed H as an Atomic Layer Resist. *J. Vac. Sci. Technol. B* **1996,** *14* (3), 1642.

(66) Albert, M. M.; Tolk, N. H. Absolute Total Cross Sections for Electron Stimulated Desorption of Hydrogen and Deuterium from Silicon(111) Measured by Second Harmonic Generation. *Phys. Rev. B* **2001,** *63* (3), 035308.

(67) Avouris, P.; Walkup, R. E.; Rossi, A. R.; Akpati, H. C.; Nordlander, P.; Shen, T. C.; Abeln, G. C.; Lyding, J. W. Breaking Individual Chemical Bonds via STM-Induced Excitations. *Surf. Sci.* **1996,** *363* (1-3), 368.

(68) Fuse, T.; Fujino, T.; Ryu, J. T.; Katayama, M.; Oura, K. Electron Stimulated Desorption of Hydrogen from H/Si(001)-1x1 Surface Studied by Time-of-Flight Elastic Recoil Detection Analysis. *Surf. Sci.* **1999,** *420* (1), 81.

(69) Shen, T. C.; Wang, C.; Abeln, G. C.; Tucker, J. R.; Lyding, J. W.; Avouris, P.; Walkup, R. E. Atomic-Scale Desorption Through Electronic and Vibrational Excitation Mechanisms. *Science* **1995,** *268* (5217), 1590.

(70) Menzel, D.; Gomer, R. Desorption from Metal Surfaces by Low Energy Electrons. *J. Chem. Phys.* **1964,** *41* (11), 3311.

(71) Redhead, P. A. Interaction of Slow Electrons with Chemisorbed Oxygen. *Can. J. Phys.* **1964,** *42* (5), 886.

(72) Feibelman, P. J.; Knotek, M. L. Reinterpretation of Electron Stimulated Desorption Data from Chemisorption Systems. *Phys. Rev. B* **1978,** *18* (12), 6531.

(73) Knotek, M. L.; Feibelman, P. J. Ion Desorption by Core-Hole Decay. *Phys. Rev. Lett.* **1978,** *40* (14), 964.

(74) Bellitto, V. J.; Yang, Y.; Thoms, B. D.; Koleske, D. D.; Wickenden, A. E.; Henry, R. L. Desorption of Hydrogen from GaN(0001) Observed by HREELS and ELS. *Surf. Sci.* **1999,** *442* (2), L1019.

(75) Chiang, C. M.; Gates, S. M.; Bensaoula, A.; Schultz, J. A. Hydrogen Desorption and Ammonia Adsorption on Polycrystalline GaN Surfaces. *Chem. Phys. Lett.* **1995,** *246* (3), 275.

(76) Shekhar, R.; Jensen, K. F. Temperature Programmed Desorption Investigations of Hydrogen and Ammonia Reactions on GaN. *Surf. Sci.* **1997,** *381* (1), L581.

(77) Lyding, J. W.; Shen, T. C.; Hubacek, J. S.; Tucker, J. R.; Abeln, G. C. Nanoscale Patterning and Oxidation of H-Passivated Si(100)2x1 Surfaces with an Ultrahigh Vacuum Scanning Tunneling Microscope. *Appl. Phys. Lett.* **1994,** *64* (15), 2010.

(78) Becker, R. S.; Higashi, G. S.; Chabal, Y. J.; Becker, A. J. Atomic Scale Conversion of Clean Si(111)-H-1x1 to Si(111)-2x1 by Electron Stimulated Desorption. *Phys. Rev. Lett.* **1990,** *65* (15), 1917.

(79) Hitosugi, T.; Hashizume, T.; Heike, S.; Watanabe, S.; Wada, Y.; Hasegawa, T.; Kitazawa, K. Scanning Tunneling Spectroscopy of Dangling-Bond Wires Fabricated on the Si(100)-2x1-H Surface. *Jpn. J. Appl. Phys., Part 2* **1997,** *36* (3B), L361.

(80) Shen, T. C.; Wang, C.; Lyding, J. W.; Tucker, J. R. Nanoscale Oxide Patterns on Si(100) Surfaces. *Appl. Phys. Lett.* **1995,** *66* (8), 976.

(81) Shen, T. C.; Wang, C.; Tucker, J. R. Al Nucleation on Monohydride and Bare Si(001) Surfaces: Atomic Scale Patterning. *Phys. Rev. Lett.* **1997,** *78* (7), 1271.

(82) Randall, J. N.; Lyding, J. W.; Schmucker, S.; Von Ehr, J. R.; Ballard, J.; Saini, R.; Xu, H.; Ding, Y. Atomic Precision Lithography on Si. *J. Vac. Sci. Technol. B* **2009,** *27* (6), 2764.

(83) Koebley, S. R.; Outlaw, R. A.; Dellwo, R. R. Degassing a Vacuum System with in situ UV Radiation. *J. Vac. Sci. Technol. A* **2012,** *30* (6), 060601.

(84) Bermudez, V. M. Theoretical Study of Hydrogen Adsorption on the GaN(0001) Surface. *Surf. Sci.* **2004,** *565* (1), 89.

(85) Nepal, N.; Qadri, S. B.; Hite, J. K.; Mahadik, N. A.; Mastro, M. A.; Eddy, C. R., Jr. Epitaxial Growth of AlN Films via Plasma-Assisted Atomic Layer Epitaxy. *Appl. Phys. Lett.* **2013,** *103* (8), 082110.

(86) Langford, J. I.; Wilson, A. J. C. Scherrer After 60 Years - Survey and Some New Results in Determination of Crystallite Size. *J. Appl. Crystallogr.* **1978,** *11* (APR), 102.

(87) Li, J.-S.; Zhang, C.-R.; Li, B.; Cao, F.; Wang, S.-Q. An Improved Synthesis of Borazine with Aluminum Chloride as Catalyst. *Eur. J. Inorg. Chem.* **2010,** *2010* (12), 1763.

(88) Cobine, J. D. *Gaseous Conductors: Theory and Engineering Applications*; McGraw-Hill Book Company, Inc.: New York, 1941.

(89) Ejder, E. Refractive Index of GaN. *Phys. Status Solidi A* **1971,** *6* (2), 445.

(90) Tanabe, N.; Hayashi, T.; Iwaki, M. Substrate Temperature Influence of c-BN Thin Film Formation by IBED. *Diamond Relat. Mater.* **1992,** *1*, 151.

(91) Balkas, C. M.; Davis, R. F. Synthesis Routes and Characterization of High-Purity, Single-Phase Gallium Nitride Powders. *J. Am. Ceram. Soc.* **1996,** *79* (9), 2309.

(92) Kumar, M. S.; Kumar, J. XRD, XPS, SEM, PL and Raman Scattering Analysis of Synthesised GaN Powder. *Mater. Chem. Phys.* **2003,** *77* (2), 341.

(93) Ishibashi, A.; Takeishi, H.; Mannoh, M.; Yabuuchi, Y.; Ban, Y. Residual Impurities in GaN/Al_2O_3 Grown by Metalorganic Vapor Phase Epitaxy. *J. Electron. Mater.* **1996,** *25* (5), 799.

(94) Chen, Q.; Dapkus, P. D. On the Thermal Decomposition of Trimethylgallium - A Molecular Beam Sampling Mass Spectroscopy Study. *J. Electrochem. Soc.* **1991,** *138* (9), 2821.

(95) Francis, J. T.; Benson, S. W.; Tsotsis, T. T. Observation of the Methyl Radical During the Surface Decomposition Reaction of Trimethylgallium. *J. Phys. Chem.* **1991,** *95* (12), 4583.

(96) Lam, H. T.; Vohs, J. M. Surface Reactions of Trimethylgallium on MOVPE-Grown GaN(0001). *Surf. Sci.* **1999,** *426* (2), 199.

(97) Armitage, R.; Hong, W.; Yang, Q.; Feick, H.; Gebauer, J.; Weber, E. R.; Hautakangas, S.; Saarinen, K. Contributions from Gallium Vacancies and Carbon-Related Defects to the "Yellow Luminescence" in GaN. *Appl. Phys. Lett.* **2003,** *82* (20), 3457.

(98) DeMierry, P.; Ambacher, O.; Kratzer, H.; Stutzmann, M. Yellow Luminescence and Hydrocarbon Contamination in MOVPE-Grown GaN. *Phys. Status Solidi A* **1996,** *158* (2), 587.

(99) Wright, A. F. Substitutional and Interstitial Carbon in Wurtzite GaN. *J. Appl. Phys.* **2002,** *92* (5), 2575.

(100) Gillis, H. P.; Choutov, D. A.; Martin, K. P.; Pearton, S. J.; Abernathy, C. R. Low Energy Electron-Enhanced Etching of GaN/Si in Hydrogen Direct Current Plasma. *J. Electrochem. Soc.* **1996,** *143* (11), L251.

(101) Madden, H. H.; Jennison, D. R.; Traum, M. M.; Margaritondo, G.; Stoffel, N. G. Correlation of Stimulated H^+ Desorption Threshold with Localized State Observed in Auger Line Shape - Si(100)-H. *Phys. Rev. B* **1982,** *26* (2), 896.

(102) Pian, T. R.; Tolk, N. H.; Traum, M. M.; Kraus, J.; Collins, W. E. Energy Dependence of Electron Stimulated Desorption of Excited Neutral Alkalis from Alkali Halides. *Surf. Sci.* **1983,** *129* (2-3), 573.

(103) Nakatsuji, K.; Matsuda, K.; Yonezawa, T.; Daimon, H.; Suga, S. Adsorption and Desorption Processes of Cl on a Si(100) Surface. *Surf. Sci.* **1996,** *363* (1-3), 321.

(104) Stawinski, U.; Bauer, E. Alkali Halide Layers on W(110) - Electron Stimulated Desorption of Ions, Structure, and Composition. *Phys. Rev. B* **1993,** *47* (19), 12820.

(105) Pearton, S. J.; Abernathy, C. R.; Vartuli, C. B.; Lee, J. W.; MacKenzie, J. D.; Wilson, R. G.; Shul, R. J.; Ren, F.; Zavada, J. M. Unintentional Hydrogenation of GaN and Related Alloys During Processing. *J. Vac. Sci. Technol. A* **1996,** *14* (3), 831.

(106) Zavada, J. M.; Wilson, R. G.; Abernathy, C. R.; Pearton, S. J. Hydrogenation of GaN, AlN and InN. *Appl. Phys. Lett.* **1994,** *64* (20), 2724.

(107) George, S. M.; Desantolo, A. M.; Hall, R. B. Surface Diffusion of Hydrogen on Ni(100) Studied Using Laser Induced Thermal Desorption. *Surf. Sci.* **1985,** *159* (1), L425.

(108) Mak, C. H.; Brand, J. L.; Deckert, A. A.; George, S. M. Surface Diffusion of Hydrogen on Ru(001) Studied Using Laser Induced Thermal Desorption. *J. Chem. Phys.* **1986,** *85* (3), 1676.

(109) Schafer, J.; Simons, A.; Wolfrum, J.; Fischer, R. A. Detection of Gas-Phase Species in MOCVD of GaN Using Molecular Beam Quadrupole Mass Spectrometry. *Chem. Phys. Lett.* **2000,** *319* (5-6), 477.

(110) Battaile, C. C.; Srolovitz, D. J.; Oleinik, II; Pettifor, D. G.; Sutton, A. P.; Harris, S. J.; Butler, J. E. Etching Effects During the Chemical Vapor Deposition of (100) Diamond. *J. Chem. Phys.* **1999,** *111* (9), 4291.

(111) Ivanov, O. A.; Muchnikov, A. B.; Chernov, V. V.; Bogdanov, S. A.; Vikharev, A. L.; Butler, J. E. Experimental Study of Hydrogen Plasma Etching of (100) Single Crystal Diamond in a MPACVD Reactor. *Mater. Lett.* **2015,** *151*, 115.

(112) Adapted from Sprenger, J. K.; Sun, H.; Cavanagh, A. S.; George, S. M. Electron Enhanced Atomic Layer Deposition of Silicon Thin Films at Room Temperature. Submitted to the Journal of Vacuum Science and Technology A. Currently under review.

(113) Coon, P. A.; Wise, M. L.; George, S. M. Modeling Silicon Epitaxial Growth with SiH_2Cl_2. *J. Cryst. Growth* **1993,** *130* (1-2), 162.

(114) Gates, S. M.; Kulkarni, S. K. Kinetics of Surface-Reactions in Very Low-Pressure Chemical Vapor-Deposition of Si from SiH_4. *Appl. Phys. Lett.* **1991,** *58* (25), 2963.

(115) Jasinski, J. M.; Gates, S. M. Silicon Chemical Vapor-Deposition One-Step at a Time - Fundamental-Studies of Silicon Hydride Chemistry. *Acc. Chem. Res.* **1991,** *24* (1), 9.

(116) Regolini, J. L.; Bensahel, D.; Scheid, E.; Mercier, J. Selective Epitaxial Silicon Growth in the 650–1100 °C Range in a Reduced Pressure Chemical Vapor Deposition Reactor using Dichlorosilane. *Appl. Phys. Lett.* **1989,** *54* (7), 658.

(117) Eversteyn, F. C. Chemical-Reaction Engineering in Semiconductor Industry. *Philips Res. Rep.* **1974,** *29* (1), 45.

(118) Gupta, P.; Colvin, V. L.; George, S. M. Hydrogen Desorption Kinetics from Monohydride and Dihydride Species on Silicon Surfaces. *Phys. Rev. B* **1988,** *37* (14), 8234.

(119) Koehler, B. G.; Mak, C. H.; Arthur, D. A.; Coon, P. A.; George, S. M. Desorption-Kinetics of Hydrogen and Deuterium from Si(111)7x7 Studied using Laser-Induced Thermal-Desorption. *J. Chem. Phys.* **1988,** *89* (3), 1709.

(120) Walsh, R. Bond-Dissociation Energy Values in Silicon-Containing Compounds and Some of Their Implications. *Acc. Chem. Res.* **1981,** *14* (8), 246.

(121) Schulze, G.; Henzler, M. Adsorption of Atomic-Hydrogen on Clean Cleaved Silicon(111). *Surf. Sci.* **1983,** *124* (2-3), 336.

(122) Wise, M. L.; Koehler, B. G.; Gupta, P.; Coon, P. A.; George, S. M. Comparison of Hydrogen Desorption-Kinetics from Si(111)7x7 and Si(100)2x1. *Surf. Sci.* **1991,** *258* (1-3), 166.

(123) Sinniah, K.; Sherman, M. G.; Lewis, L. B.; Weinberg, W. H.; Yates, J. T.; Janda, K. C. Hydrogen Desorption from the Monohydride Phase on Si(100). *J. Chem. Phys.* **1990,** *92* (9), 5700.

(124) Fuse, T.; Fujino, T.; Ryu, J.-T.; Katayama, M.; Oura, K. Electron-Stimulated Desorption of Hydrogen from H/Si(001)1x1 Surface Studied by Time-of-Flight Elastic Recoil Detection Analysis. *Surf. Sci.* **1999,** *420* (1), 81.

(125) Matsunami, N.; Hasebe, Y.; Itoh, N. Determination of the Absolute Cross Scetion of Electron-Stimulated-Desorption of Deuterium from Si(111). *Surf. Sci.* **1987,** *192*, 27.

(126) Antoniewicz, P. R. Model for Electron-Stimulated and Photon-Stimulated Desorption. *Phys. Rev. B* **1980,** *21* (9), 3811.

(127) Madey, T. E. History of Desorption Induced by Electronic-Transitions. *Surf. Sci.* **1994,** *299* (1-3), 824.

(128) Yates, J. T. Electron Stimulated Desorption, DIET, and Photochemistry at Surfaces: A Personal Recollection. *J. Chem. Phys.* **2012,** *137* (9), 091701.

(129) Czyzewski, J. J.; Madey, T. E.; Yates, J. T. Angular Distributions of Electron-Stimulated-Desorption Ions: Oxygen on W(100). *Phys. Rev. Lett.* **1974,** *32* (14), 777.

(130) Yasue, T.; Ichimiya, A.; Ohtani, S. Electron Stimulated Desorption Ion Angular Distribution (ESDIAD) from LiF Surface. *Appl. Surf. Sci.* **1988,** *33/34*, 167.

(131) Wallace, R. M.; Taylor, P. A.; Dresser, M. J.; Choyke, W. J.; Yates, J. T. Background Effects in Electron Stimulated Desorption Ion Angular Distribution (ESDIAD) Measurements on Si(111)(7x7). *Rev. Sci. Instrum.* **1991,** *62* (3), 720.

(132) Johnson, A. L.; Walczak, M. M.; Madey, T. E. ESDIAD of First-Row Protic Hydrides Adsorbed on Si(100): Structure and Reactivity. *Langmuir* **1988,** *4*, 277.

(133) Randolph, S. J.; Fowlkes, J. D.; Rack, P. D. Focused, Nanoscale Electron-beam-induced Deposition and Etching. *Crit. Rev. Solid State Mater. Sci.* **2006,** *31* (3), 55.

(134) Adams, D. P.; Mayer, T. M.; Swartzentruber, B. S. Nanometer-scale Lithiography on Si(001) using Adsorbed H as an Atomic Layer Resist. *J. Vac. Sci. Technol. B* **1996,** *14* (3), 1642.

(135) Avouris, P.; Walkup, R. E.; Rossi, A. R.; Akpati, H. C.; Nordlander, P.; Shen, T. C.; Abeln, G. C.; Lyding, J. W. Breaking Individual Chemical Bonds via STM-Induced Excitations. *Surf. Sci.* **1996,** *363*, 368.

(136) Shen, T. C.; Wang, C.; Abeln, G. C.; Tucker, J. R.; Lyding, J. W.; Avouris, P.; Walkup, R. E. Atomic-Scale Deposition through Electronic and Vibration-Excited Mechanisms. *Science* **1995,** *268*, 1590.

(137) Ballard, J. B.; Owen, J. H. G.; Owen, W.; Alexander, J. R.; Fuchs, E.; Randall, J. N.; Von Ehr, J. R.; McDonnell, S.; Dick, D. D.; Wallace, R. M.et al. Pattern Transfer of Hydrogen Depassivation Lithography Patterns into Silicon with Atomically Traceable Placement and Size Control. *J. Vac. Sci. Technol. B* **2014,** *32* (4), 041804.

(138) Goh, K. E. J.; Chen, S.; Xu, H.; Ballard, J.; Randall, J. N.; Von Ehr, J. R. Using Patterned H-resist for Controlled Three-dimensional Growth of Nanostructures. *Appl. Phys. Lett.* **2011,** *98* (16), 163102.

(139) Owen, J. H. G.; Ballard, J.; Randall, J. N.; Alexander, J.; Von Ehr, J. R. Patterned Atomic Layer Epitaxy of Si/Si(001):H. *J. Vac. Sci. Technol. B* **2011,** *29* (6), 06f201.

(140) Sprenger, J. K.; Cavanagh, A. S.; Sun, H.; Wahl, K. J.; Roshko, A.; George, S. M. Electron Enhanced Growth of Crystalline Gallium Nitride Thin Films at Room Temperature and 100 °C Using Sequential Surface Reactions. *Chem. Mater.* **2016,** *28* (15), 5282.

(141) Asif Khan, M.; Kuznia, J. N.; Van Hove, J. M.; Olson, D. T.; Krishnankutty, S.; Kolbas, R. M. Growth of High Optical and Electrical Quality GaN Layers using Low-Pressure Metalorganic Chemical Vapor Deposition. *Appl. Phys. Lett.* **1991,** *58* (5), 526.

(142) Gibart, P. Metal Organic Vapour Phase Epitaxy of GaN and Lateral Overgrowth. *Rep. Prog. Phys.* **2004,** *67* (5), 667.

(143) Ahn, B.-C.; Shimizu, K.; Satoh, T.; Kanoh, H.; Sugiura, O.; Matsumara, M. Hot-Wall Chemical-Vapor-Deposition of Amorphous-Silicon and Its Application to Thin-Film Transitors. *Jpn. J. Appl. Phys.* **1991,** *30* (12B), 3695.

(144) Madden, H. H.; Jennison, D. R.; Traum, M. M.; Margaritondo, G.; Stoffel, N. G. Correlation of Stimulated H^+-Desorption Threshold with Localized State Observed in Auger Line Shape - Si(100):H. *Phys. Rev. B* **1982,** *26* (2), 896.

(145) Shepperd, K. R.; Lane, C. D.; Orlando, T. M. Low-Energy Electron-Stimulated Desorption of Cations and Neutrals from Si(111)(7x7):C_2D_2. *J. Chem. Phys.* **2010,** *132* (21), 214704.

(146) Ueda, K.; Kodama, S.; Takano, A. Desorption Study of a Proton from H/Si(100) by Electron Stimulated Desorption Spectroscopy. *Surf. Sci.* **1992,** *283*, 195.

(147) Dillon, A. C.; Robinson, M. B.; George, S. M. Decomposition of Silicon Hydrides Following Disilane Adsorption pn Porous Silicon Surfaces. *Surf. Sci.* **1993,** *295* (1-2), L998.

(148) Uram, K. J.; Jansson, U. The Adsorption of Disilane on Si(111)7x7 as Studied by Multiple Internal-Reflection Spectroscopy. *Surf. Sci.* **1991,** *249* (1-3), 105.

(149) Gates, S. M. Adsorption-Kinetics of SiH_4, Si_2H_6 and Si_3H_8 on the Si(111)(7x7) Surface. *Surf. Sci.* **1988,** *195* (1-2), 307.

(150) Wu, Y. M.; Nix, R. M. Adsorption of Hydrogen and Disilane on Si(100) and Si-Ge Surfaces. *Surf. Sci.* **1994,** *306* (1-2), 59.

(151) Ong, S. W.; Tok, E. S.; Kang, H. C. Revisiting the Vibrational Spectra of Silicon Hydrides on Si(100)(2x1) Surface: What is on the Surface When Disilane Dissociates? *J. Chem. Phys.* **2010,** *133* (7), 074708.

(152) Shinohara, M.; Niwano, M.; Neo, Y.; Yokoo, K. Infrared Study of Adsorption and Thermal Decomposition of Si_2H_6 on Si(100). *Thin Solid Films* **2000,** *369* (1-2), 16.

(153) Goeden, C.; Dollinger, G. Electron Stimulated Desorption of Diamond(100) as a Negative Hydrogen Source. *Appl. Surf. Sci.* **1999,** *147*, 107.

(154) Madey, T. E.; Yates, J. T. Electron-Stimulated Desorption as a Tool for Studies of Chemisorption: A Review. *J. Vac. Sci. Technol.* **1971,** *8* (4), 525.

(155) Chung, Y. B.; Park, H. K.; Lee, D. K.; Jo, W.; Song, J. H.; Lee, S. H.; Hwang, N. M. Low Temperature Deposition of Crystalline Silicon on Glass by Hot Wire Chemical Vapor Deposition. *J. Cryst. Growth* **2011,** *327* (1), 57.

(156) Koch, C.; Ito, M.; Schubert, M. Low-temperature Deposition of Amorphous Silicon Solar Cells. *Sol. Energy Mater. Sol. Cells* **2001,** *68* (2), 227.

(157) Lee, S. H.; Jung, J. S.; Lee, S. S.; Lee, S. B.; Hwang, N. M. Low Temperature Deposition of Polycrystalline Silicon Thin Films on a Flexible Polymer Substrate by Hot Wire Chemical Vapor Deposition. *J. Cryst. Growth* **2016,** *453*, 151.

(158) Schubert, M. B. Low Temperature Silicon Deposition for Large Area Sensors and Solar Cells. *Thin Solid Films* **1999,** *337* (1-2), 240.

(159) Barbee, T. W.; Mrowka, S.; Hettrick, M. C. Molybdenum-Silicon Multilayer Mirrors for the Extreme Ultraviolet. *Appl. Opt.* **1985,** *24* (6), 883.

(160) Yulin, S.; Benoit, N.; Feigl, T.; Kaiser, N. Interface-engineered EUV Multilayer Mirrors. *Microelectron. Eng.* **2006,** *83* (4-9), 692.

(161) Voorma, H.-J.; Louis, E.; Koster, N. B.; Bijkerk, F. Temperature Induced Diffusion in Mo/Si Multilayer Mirrors. *J. Appl. Phys.* **1998,** *83* (9), 4700.

(162) Moffat, T. P.; Josell, D. Extreme Bottom-Up Superfilling of Through-Silicon-Vias by Damascene Processing: Suppressor Disruption, Positive Feedback and Turing Patterns. *J. Electrochem. Soc.* **2012,** *159* (4), D208.

(163) Adapted from Sprenger, J. K.; Sun, H.; Cavanagh, A. S.; Roshko, A.; Blanchard, P.; George, S. M. Electron Enhanced Atomic Layer Deposition of Boron Nitride Thin Films at Room Temperature. In preparation for submission to Chemistry of Materials.

(164) Sprenger, J. K.; Sun, H.; Cavanagh, A. S.; George, S. M. Electron-Enhanced Atomic Layer Deposition of Silicon Thin Films at Room Temperature. *Submitted to J. Vac. Sci. Technology* **2017**.

(165) Dean, C. R.; Young, A. F.; Meric, I.; Lee, C.; Wang, L.; Sorgenfrei, S.; Watanabe, K.; Taniguchi, T.; Kim, P.; Shepard, K. L.et al. Boron Nitride Substrates for High-Quality Graphene Electronics. *Nat. Nanotechnol.* **2010,** *5*, 722.

(166) Zhang, M.; Zhu, Y.; Wang, X.; Feng, Q.; Qiao, S.; Wen, W.; Chen, Y.; Cui, M.; Zhang, J.; Cai, C. Controlled Synthesis of ZrS_2 Monlayer and Few Layers on Hexagonal Boron Nitride. *J. Am. Chem. Soc.* **2015,** *137* (22), 7051.

(167) Kumar, N. A.; Dar, M. A.; Gul, R.; Baek, J.-B. Graphene and Molybdenum Disulfide Hybrids: Synthesis and Applications. *Mater. Today* **2015,** *18* (5), 286.

(168) Roy, T.; Tosun, M.; Kang, J. S.; Sachid, A. B.; Desai, S. B.; Hettick, M.; Hu, C. C.; Javey, A. Field-Efect Transistors Built from All Two-Dimensional Material Components *ACS Nano* **2014,** *8* (6), 6259.

(169) Britnell, L.; Gorbachev, R. V.; Jalil, R.; Belle, B. D.; Schedin, F.; Mishchenko, A.; Georgiou, T.; Katsnelson, M. I.; Eaves, L.; Morozov, S. V.et al. Field-Effect Tunneling Transistor Based on Vertical Graphene Heterostructures. *Science* **2012,** *335* (6071), 947.

(170) Khan, M. H.; Casillas, G.; Mitchell, D. R.; Liu, H. K.; Jiang, L.; Huang, Z. Carbon- and Crack-Free Growth of Hexagonal Boron Nitride Nanosheets and Their Uncommon Stacking Order. *Nanoscale* **2016,** *8* (35), 15926.

(171) Li, J.-S.; Zhang, C.-R.; Li, B.; Cao, F.; Wang, S.-Q. Boron Nitride Coatings by Chemical Vapor Deposition from Borazine. *Surf. Coat. Technol.* **2011,** *205* (12), 3736.

(172) Shi, Y.; Hamsen, C.; Jia, X.; Kim, K. K.; Reina, A.; Hofmann, M.; Hsu, A. L.; Zhang, K.; Li, H.; Juang, Z. Y.et al. Synthesis of Few-Layer Hexagonal Boron Nitride Thin Film by Chemical Vapor Deposition. *Nano Lett.* **2010,** *10* (10), 4134.

(173) Driver, M. S.; Beatty, J. D.; Olanipekun, O.; Reid, K.; Rath, A.; Voyles, P. M.; Kelber, J. A. Atomic Layer Epitaxy of h-BN(0001) Multilayers on Co(0001) and Molecular Beam Epitaxy Growth of Graphene on h-BN(0001)/Co(0001). *Langmuir* **2016,** *32* (11), 2601.

(174) Jones, J.; Beauclair, B.; Olanipekun, O.; Lightbourne, S.; Zhang, M.; Pollok, B.; Pilli, A.; Kelber, J. A. Atomic Layer Deposition of h-BN(0001) on RuO2(110)/Ru(0001). *J. Vac. Sci. Technol. A* **2017,** *35* (1), 01B139.

(175) Mårlid, B.; Ottosson, M.; Pettersson, U.; Larsson, K.; Carlsson, J.-O. Atomic Layer Deposition of BN Thin Films. *Thin Solid Films* **2002,** *402* (1-2), 167.

(176) Hemmi, A.; Bernard, C.; Cun, H.; Roth, S.; Klockner, M.; Kalin, T.; Weinl, M.; Gsell, S.; Schreck, M.; Osterwalder, J.et al. High Quality Single Atomic Layer Deposition of Hexagonal Boron Nitride on Single Crystalline Rh(111) Four-Inch Wafers. *Rev. Sci. Instrum.* **2014,** *85* (3), 035101.

(177) Ferguson, J. D.; Weimer, A. W.; George, S. M. Atomic Layer Deposition of Boron Nitride using Sequential Exposures of BCl3 and NH3. *Thin Solid Films* **2002,** *413*, 16.

(178) Fuse, T.; Fujino, T.; Ryu, J.-T.; Katayama, M.; Oura, K. Electron-Stimulated Desorption of Hydrogen from H/Si(001)-1×1 Surface Studied by Time-of-Flight Elastic Recoil Detection Analysis. *Surf. Sci.* **1999,** *420* (1), 81.

(179) Matsunami, N.; Hasebe, Y.; Itoh, N. Determination of the Absolute Cross Scetion of Electron-Stimulated-Desorption of Deuterium from Si (111). *Surf. Sci.* **1987,** *192*, 27.

(180) Paffett, M. T.; Simonson, R. J.; Papin, P.; Paine, R. T. Borazine Adsorption and Decomposition at Pt(111) and Ru(001) Surfaces. *Surf. Sci.* **1990,** *232*, 286.

(181) Commercial equipment, instruments, or materials are identified only in order to adequately specify certain procedures. In no case does such identification imply recommendation or endorsement by the National Institute of Standards and Technology, nor does it imply that the products identified are necessarily the best available for the purpose.

(182) Goeden, C.; Dollinger, G. Electron Stimulated Desorption of Diamond (100) as a Negative Hydrogen Source. *Appl. Surf. Sci.* **1999,** *147*, 107.

(183) Madey, T. E.; Yates, J. T. Electron-Stimulated Desorption as a Tool for Studies of Chemisorption: A Review. *J. Vac. Sci. Technol.* **1971,** *8* (4), 525.

(184) Joint Committee on Powder Diffraction Standards (JCPDS). JCPDS File 85-1068.

(185) Brager, A. An X-ray Examination of the Structure of Boron Nitride. *Acta Physicochimica USSR* **1937,** *7*, 699.

(186) Kurdyumov, A. V.; Solozhenko, V. L.; Zelyavski, W. B. Lattice Parameters of Boron Nitride Polymorphous Modifications as a Function of Their Crystal-Structure Perfection. *J. Appl. Crystallogr.* **1995,** *28*, 540.

(187) Saitoh, H.; Yarbrough, W. A. Preparation and Characterization of Nanocrystalline Cubic Boron Nitride by Microwave Plasma-Enhanced Chemical Vapor Deposition. *Appl. Phys. Lett.* **1991,** *58* (20), 2228.

(188) Zhang, W. J.; Chong, Y. M.; Bello, I.; Lee, S. T. Nucleation, Growth and Characterization of Cubic Boron Nitride (cBN) Films. *J. Phys. D: Appl. Phys.* **2007,** *40* (20), 6159.

(189) Gielisse, P. J.; Mitra, S. S.; Plendl, J. N.; Griffis, R. D.; Mansur, L. C.; Marshall, R.; Pascoe, E. A. Lattice Infrared Spectra of Boron Nitride and Boron Monophosphide. *Phys. Rev.* **1967,** *155* (3), 1039.

(190) Nocua, J. E.; Piazza, F.; Weiner, B. R.; Morell, G. High-Yield Synthesis of Stoichiometric Boron Nitride Nanostructures. *J. Nanomater.* **2009,** *2009*, 1.

(191) The contribution of an agency of the U.S. government is not subject to copyright.

(192) Zhang, W. J.; Meng, X. M.; Chan, C. Y.; Chan, K. M.; Wu, Y.; Bello, I.; Lee, S. T. Interfacial Study of Cubic Boron Nitride Films Deposited on Diamond. *J. Phys. Chem. B* **2005,** *109*, 16005.

(193) Hofsäss, H.; Eyhusen, S.; Ronning, C. On the Mechanisms of Cubic Boron Nitride Film Growth. *Diamond Relat. Mater.* **2004,** *13* (4-8), 1103.

(194) Yang, H. S.; Iwamoto, C.; Yoshida, T. Nanostructures of the turbostratic BN transition layer in cubic BN thin films deposited by low-pressure inductively coupled plasma-enhanced chemical vapor deposition. *J. Appl. Phys.* **2002,** *91* (10).

(195) Moffat, T. P.; Josell, D. Extreme Bottom-Up Superfilling of Through-Silicon-Vias by Damascene Processing: Suppressor Distribution, Positive Feedback and Turing Patterns. *Journal of the Electrochemiscal Society* **2012,** *159* (4), D208.

(196) Dolgov, A.; Lopaev, D.; Rachimova, T.; Kovalev, A.; Vasil'eva, A.; Lee, C. J.; Krivtsun, V. M.; Yakushev, O.; Bijkerk, F. Comparison of H_2 and He Carbon Cleaning Mechanisms in Extreme Ultraviolet Induced and Surface Wave Discharge Plasmas. *J. Phys. D: Appl. Phys.* **2014,** *47* (6).

(197) Lancaster, C. A.; Shumaker-Parry, J. S. Surface Preparation of Gold Nanostructureson Glass by Ultraviolet Ozone and Oxygen Plasma for Thermal Atomic Layer Deposition of Al_2O_3. *Thin Solid Films* **2016,** *612*, 141.

(198) Vig, J. R. UV/Ozone Cleaning of Surfaces. *J. Vac. Sci. Technol., A* **1985,** *3* (3), 1027.

(199) Kukushkin, S. A.; Osipov, A. V.; Bessolov, V. N.; Medvedev, B. K.; Nevolin, V. K.; Tcarik, K. A. Substrates for Epitaxy of Gallium Nitride: New Materials and Techniques. *Rev. Adv. Mater. Sci.* **2008,** *17*, 1.

(200) An, Q.; Jaramillo-Botero, A.; Liu, W.-G.; Goddard, W. A. Reaction Pathways of GaN (0001) from Trimethylgallium and Ammonia versus Triethylgallium and Hydrazine Using First Principle Calculations. *J. Phys. Chem. C* **2015,** *119* (8), 4095.

(201) Savastiouk, S. Moore's Law - The Z Dimension. *Solid State Technol.* **2000,** *43* (1).

(202) Zhang, Y.; Ding, G.; Wang, H.; Cheng, P.; Liu, R. Optimization of Innovative Approaches to the Shortening of Filling Times in 3D Integrated Through-Silicon Vias (TSVs). *J. Micromech. Microeng.* **2015,** *25* (4), 045009.

(203) Lim, S. K. *Design of High Performance, Low Power, and Reliable 3D Integrated Circuits*; Springer: New York, 2013.

(204) Motoyoshi, M. Through-Silicon Via (TSV). *Proc. IEEE* **2009,** *97* (1), 43.

(205) Du, L.; Shi, T.; Su, L.; Xue, D.; Liao, G. A Novel Bottom-Up Copper Filling of Blind Silicon Vias in 3D Electronic Packaging. *J. Micromech. Microeng.* **2015,** *25* (4).

(206) Heng, W.; Zhen'an, T.; Zhu, W.; Wan, C.; Daquan, Y. Simulation of Through Via Bottom-Up Copper Plating with Accelerator for the Filling of TSVs. *J. Semicond.* **2013,** *34* (9).

(207) Heo, H.; Sung, J. H.; Ahn, J.-H.; Ghahari, F.; Taniguchi, T.; Watanabe, K.; Kim, P.; Jo, M.-H. Frank-van der Merwe Growth versus Volmer-Weber Growth in Successive Stacking of a Few-Layer Bi_2Te_3/Sb_2Te_3 by van der Waals Heteroepitaxy: The Critical Roles of Finite Lattice-Mismatch with Seed Substrates. *Adv. Electron. Mater.* **2017,** *3* (2), 1600375.

(208) Krupski, A. Growth Morphology of Thin Films on Metallic and Oxide Surfaces. *J. Phys.: Condens. Matter* **2014,** *26* (5).

(209) Evans, M. M. R.; Glueckstein, J. C.; Nogami, J. Epitaxial Growth of Manganese of Silicon: Volmer-Weber Growth on the Si(111) Surface. *Phys. Rev. B* **1996,** *53* (7).

(210) Floro, J. A.; Chason, E.; Cammarata, R. C.; Srolovitz, D. J. Physical Origins of Intrinsic Stresses in Volmer-Weber Thin Films. *MRS Bull.* **2002,** *27* (1), 19.

(211) Weber, M. J.; Mackus, A. J. M.; Verheijen, M. A.; van der Marel, C.; Kessels, W. M. M. Supported Core/Shell Bimetallic Nanoparticles Synthesis by Atomic Layer Deposition. *Chem. Mater.* **2012,** *24* (15), 2973.

(212) Van Bui, H.; Kovalgin, A. K.; Wolters, R. A. M. Growth of Sub-Nanometer Thin Continuous TiN Films by Atomic Layer Deposition. *ECS J. Solid State Sci. Tech.* **2012,** *1* (6), 285.

(213) Lee, Y.; George, S. M. Atomic Layer Etching of Al_2O_3 using Sequential, Self-Limiting Thermal Reactions with $Sn(acac)_2$ and Hydrogen Flouride. *ACS Nano* **2015,** *9* (2), 2061.

(214) Lee, Y.; Huffman, C.; George, S. M. Selectivity in Thermal Atomic Layer Etching using Sequential, Self-Limiting Fluorination and Ligand-Exchange Reactions. *Chem. Mater.* **2016,** *28* (21).

(215) George, S. M.; Lee, Y. Prospects for Thermal Atomic Layer Etching using Sequential, Self-Limiting Fluorination and Ligand-Exchange Reactions. *ACS Nano* **2016,** *10* (5), 4889.